Earthquake triggered submarine slides in Norway

Marthe Fenne Vestly

MASTER OF SCIENCE, GEODYNAMICS
DEPARTMENT OF EARTH SCIENCE
UNIVERSITY OF BERGEN

December 2017

Abstract

Towards the end of the last glacial period, several episodes of submarine mass failures has taken place both in Norwegian fjords and on the continental shelf. Submarine mass failures have the potential of generating tsunamis which can cause great harm to coastal communities and offshore infrastructure. Because slides on the continental shelf can be initiated on slopes with low inclination, it has been assumed that an external trigger mechanism is required to initiate failure. Earthquakes is one of the suggested trigger mechanism for slides on gentle slopes. The Storegga slide, which occurred offshore Norway approximately 8200 years ago, may have been triggered by an earthquake. The slide generated a tsunami that had a run up height of 10-12 meters. There exists several large faults in the area of the Storegga slide, which have the potential of generating earthquakes of relatively high magnitudes. In the area, two earthquakes with a magnitude above 5 was recorded in 1988 and 1989. It is assumed that the area can also experience earthquakes with this magnitude also in the future. This study has performed modeling of 14 faults located in the Storegga area. The critical acceleration, or the ground motion required to initiate slide has been calculated. Two different ground motion prediction equations depending on magnitude and distance have been evaluated together with the critical acceleration to calculate the maximum distance from fault to initiation area for an earthquake to be the responsible triggering mechanism for slides. The program EXSIM12 was used to model the resulting ground motion from earthquakes with a magnitude of 5 to 7. The sediment response to earthquakes has been evaluated with the program DEEPSOIL. The pseudo-static limit equilibrium method has been used to obtain an index of stability, and a seismic-induced permanent displacement equation has been used to calculate the permanent displacement that could occur in a slope as a response to an earthquake. The results indicate that the stability of the slope considered is very stable on low slope angles, and a higher slope inclination would be required for an earthquake to initiate failure.

Acknowledgments

This thesis has been written as part of a master's degree in geodynamics at the Department of Earth Science at the University of Bergen.

First, I would like to thank my supervisor Mathilde Bøttger Sørensen for her help and useful feedbacks. Especially with the modeling in EXSIM12 and for helpful discussions and inputs whilst writing this thesis. I also want thank my co-supervisor Prof. Berit Oline Hjelstuen for her geological inputs and feedbacks.

Brian Carlton from the Norwegian Geotechincal Institute is thanked for his valuable inputs and help with DEEPSOIL and seismic slope stability analyses. Prof. Kuvvet Atakan and Prof. Haflidi Haflidason for their expertise and advice regarding selection of faults for modeling purposes.

The conference "Geofaredagen" held in October 2017 in Oslo provided me great inspiration for further work with geohazards. The Norwegian National Seismic Network (operated by the University of Bergen) is thanked for sponsoring my trip to Oslo.

My friends at the University of Bergen and roommates deserve a big thank you for their support and all the good memories during my student time in Bergen. A special thanks goes to Anette and Mari for their help proofreading and encouragement during writing this thesis.

Finally, I want to give a huge thanks to my family. My mom, dad and little brothers for always supporting and believing in me.

Contents

Appendix:

Chapter 1

Introduction

1.1 Motivation

Submarine mass failures (SMF) and their associating hazard to the society are well established though several recent events which included fatalities and loss of infrastructure. The 1998 Papua New Guinea, 1979 Nice Airport and 1929 Grand Banks are examples of events that caused tsunamis not generated by large tectonic earthquakes. These events caused awareness that tsunamis also can be generated by SMF. Tsunamis generated by submarine landslides triggered by moderate earthquakes, does not often allow for early warning as for large tectonic earthquakes, thus pose a great hazard to coastal communities (Lamarche et al., 2016).

SMF may not only cause tsunamis, but can also pose a threat to offshore infrastructure, such as platforms, communication cables and pipelines from the petroleum industry. Exploration for hydrocarbons offshore are moving towards other environments, such as deeper water, where SMF can pose a significant threat to installations (Lamarche et al., 2016).

Lamarche et al. (2016) describes the progress and challenges concerning submarine mass failures. They states that the link between earthquakes and continental slides are well established, but the link of submarine slides and earthquakes are not that well established. Many factors concerning the triggering process of submarine mass failures on gentle slopes still remains to be answered. It has therefore been performed extensively studies to obtain knowledge on how these submarine mass failures develops, how they might be triggered and their frequency of occurrence (Lamarche et al., 2016).

SMF often occur on open continental slopes with very gentle slopes ($<2°$) that are almost always considered stable on land. The low gradients of these slopes indicate that one or several external triggering mechanisms must be involved (Talling et al., 2014). The literature describes several potential triggering mechanisms, among them natural triggers; earthquakes, tectonic faulting, excess pore pressure due to rapid sedimentation during glacial periods, gas hydrate melting due increased sea water temperature after glacial periods. Man-made triggers such as anchor forces from ships or floating platforms, rock-filling for pipeline supports, temperature change around wells in the field development area, underground blow-outs, reservoir depletion and subsidence (including induced seismicity) (Nadim et al., 2005). In this study I will evaluate earthquakes as a separate trigger mechanisms. However it is important to keep in mind that combinations of several mechanisms can lead to the finial failure. Section 1.4 will give a short introduction to submarine mass failures and some important aspects concerning these.

The Storegga Slide have been claimed to be earthquake triggered by many previously published studied (e.g. Bryn et al., 2005). Due to the discovery and development of the gas field Ormen Lange the area has been extensively studied, and there are good access to information and data from the area. The access to data and because the Storegga slide are claimed to be earthquake triggered, this slide has been studied. If the investigation give indication that the Storegga Slide was earthquake triggered, this can be used as an analog to the seismic slope stability for other location of the same depositional history and bathymetry as the Storegga region. The Storegga area and the Mid-Norwegian continental shelf are described more detailed in Section 1.3 and 2.1.

There has been a significant progress since the first discoveries of submarine mass failures (e.g Heezen and Ewing, 1952), but still many mechanisms and processes are only partly understood (Huvenne et al., 2016). Because SMF often occur on remote locations and are located under water, several challenges are associated with the study of submarine slides. Direct observations and in-situ measurements are challenging (Talling et al., 2014; Huvenne et al., 2016), and the deep waters requires special equipments for field investigations and measurements (Strout and Tjelta, 2005). Hence, the main source of information are from the failed sequence and slide deposits (Huvenne et al., 2016). Various modeling performed in slope stability analyses requires input parameters ideally obtained from field investigation at the particular site. Because of the challenges in field investigation, the uncertainties and quality of inputs data can cause large uncertainties in the modeling results (Bellwald, Benjamin, and University of Bergen, 2016).

1.2 Objectives

The initiation and location of submarine mass failures are controlled by a wide variety of physical and mechanical processes, which have lead research to the development of a range of approaches and methodologies in order to improve knowledge on the potential impacts of SMF. The various methods, approaches and investigations can be summed up in the following main categories (Huvenne et al., 2016; Lamarche et al., 2016):

- Geophysical surveys (reflection, multibeam bathymetry)
- Geological sampling (coring)
- Geotechnical investigations (soil parameters, shear strength etc.)
- Analogue and numerical modeling techniques

One of the modeling techniques for slope stability are developed based on the pseudo-static limit equilibrium method, more commonly known as the Factor of Safety (FoS) concept, first attributed to Terzaghi (1950) (Kramer, 1996). The FoS concept are based on the ratio between resisting forces and driving forces, and will give an index of stability. The pseudo-static method include the horizontal and vertical static seismic forces to simulate the potential inertial forces due to ground acceleration in an earthquake (Abramson et al., 1996). The seismic-induced permanent displacement method (e.g. Bray, 2007) are another method for evaluation of seismic slope stability. Several equations have been proposed by different scientist, however, they are all based on the sliding block model, first proposed by Newmark (1965) in the fifth Rankine lecture. These two methods are linked to one-dimensional problems, but there also exist two- and three-dimensional modeling techniques for slope stability analysis. An example of 2D analysis is the method of slices, which divides the potential failure mass into slices and considers each slice as an individual block allowing complex slope geometries, variable soil conditions and the influence of external boundary loads to be considered (Abramson et al., 1996). Due to their complexity, 3D stability analyses are rarely used in practice. However, they are important where the slope geometry and slip surface have large variations in the lateral direction and the properties of the materials in place are highly non-homogeneous (Chakraborty and Goswami, 2016).

The characterizing of submarine slope failures on the continental slope are their large size and depths in the range of a few meters to hundreds of meters (Biscontin and Pestana, 2006). Continental slopes are often long and continuous (Talling et al., 2014) and have a stratigraphy of parallel layers of normally consolidated to lightly over consolidated clayey soils (Biscontin and Pestana, 2006). The ratio between the failure depth and other dimensions are often small (Carlton et al., 2016), and the lateral sedimentary layers in continental slopes are often homogeneous, so the boundary effects can safely be ignored and the slope can be considered as an infinite slope. When the slope can be considered as an infinite slope, 1D site response analyses can be used to model the seismic response of a slope (Biscontin and Pestana, 2006). Because modeling of 3D wave propagation and slope stability is extremely challenging and the problem usually simplifies to a 1D case (Biscontin and Pestana, 2006; Chakraborty and Goswami, 2016).

To investigate earthquakes effect on slope stability, I have performed ground motion modeling of selected faults with various distance to the assumed initiation area. The site response, i.e. the response of sediments to seismic loading, was then evaluated through an equivalent linear and a non-linear approach. The resulting ground motion at the assumed initiation location of the slide was then analyzed in terms of pseudo-static limit equilibrium analysis and seismic-induced permanent displacement analysis. This analyses was evaluated with respect to the slope angle to obtain an indication of the slope inclination an earthquake can be responsible for triggering submarine slides. The methodology and approaches are described detailed in Chapter 3.

Aware that the methods presented in this thesis probably not will give a well-defined conclusion of earthquakes as a triggering mechanism, this thesis will try to link theoretical ground motion and soil response to the question of earthquake as a triggering mechanism for submarine landslides on gentle slopes. Chapter 4 will discuss the input parameters used in the analyses, and Chapter 6 will discuss and compare the input parameters with the modeling result, and suggest improvements and further work.

1.3 Study Area - The Storegga region

The Storegga area (Figure 1.1) is located offshore the coast of Mid-Norway, roughly bounded by 0-6°E and 62-67°N (Solheim et al., 2005). Along the Mid-Norwegian margin, several slides have been identified on reflection seismic data with an interval of approximately 100ky during the past 2.5 million years (e.g. Bryn et al., 2005, 2003; Solheim et al., 2005; Evans et al., 1996). The Storegga slide was the last major slide to occur in the area 8200 years ago (Haflidason et al., 2005, 2004). Mapped deposits suggest that a tsunami, with a run up of 10-12 meters on the west coast of Norway, 4-6 meters on Scotland, 20-30 meters on Shetland and above 10 meters on the Faroes, was generated by the slide(Bondevik et al., 2003). The slide removed between 2400 and 3200km^3 from the slide scar, affected an area of approximately 95.000km^2, and is considered to be among the largest submarine slide identified in the world (Haflidason et al., 2005).

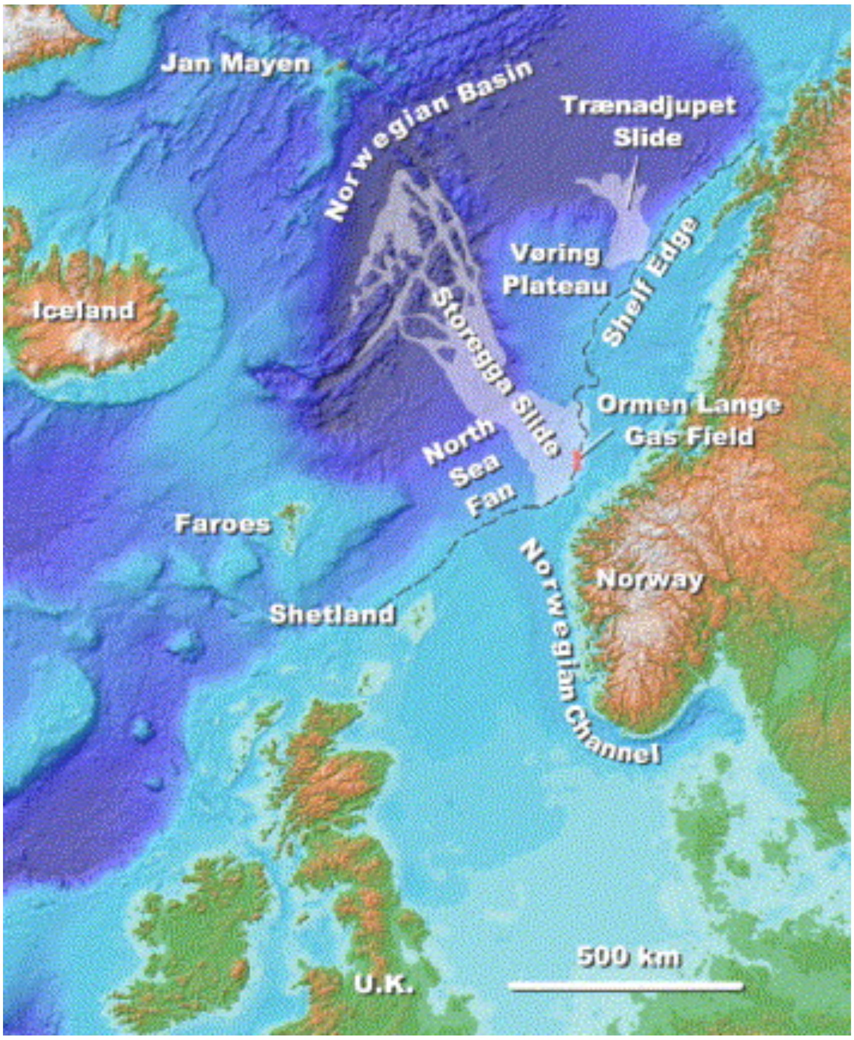

Figure 1.1: Map displaying the location of the Storegga slide, the North Sea Fan and the Ormen Lange Gas Field. From Bryn et al. (2005).

The preslide inclination of the slope was 1-2° in the upper slope, 0.6-0.7° in the middle and 10-15° in the lower slope areas (Bryn et al., 2005). Because the average inclination of the preslide slope is low and there is good access to data, the Storegga slide has been evaluated to be a good candidate for the investigation of earthquake triggered submarine slide.

Several mechanisms have earlier been evaluated for the potential of triggering the slide. Among them are rapid sediment loading during peak glaciations, gas hydrates and earthquakes the mechanisms that have been given most attention when evaluating the Storegga slide. One common feature for all mechanism are that they may increase the pore pressure in the sediment (Bryn et al., 2005). Other mechanisms should also be considered when evaluating slope stability, weak layers have been given more attention (Talling et al., 2014) and man-made impacts such as anchors, increase in temperature around wells, extra loads on the sea floor for different purposes (Nadim et al., 2005). The man-made triggering factors are not the case for the Storegga, but for future slope stability evaluations they should be considered.

During peak glaciations, enormous amounts of sediments can be deposited on the continental shelf. Excess pore pressure can be generated as a response to rapid loading. When sediments with low permeability are deposited faster than the time for consolidation, the drainage path increases and excess pore pressure can be generated (Kvalstad et al., 2005b). Another possibility shown by numerical modeling by Kvalstad et al. (2005b), that excess pore pressure may have been generated in the North Sea Fan, where the deposition rate was higher (Solheim et al., 2005), and then spread laterally towards the Storegga area.

Gas hydrates can melt as temperature in the water increases, thus destabilizing slopes by increasing the pore pressure. However, they are believed to affect slope stability locally and not large areas as the Storegga slide (Talling et al., 2014; Bryn et al., 2005; Kvalstad, 2014).

Following the deglaciation of Scandinavia, earthquakes was generated as a response to the glacio-isostatic rebound (Bungum et al., 2005; Bungum and Lindholm, 1997; Fjeldskaar et al., 2000). Sediment loading on the North Sea Fan causing isostatic deformation and reactivation of Late Jurassic – Early Cretaceous faults probably resulted in an increase in earthquake events during the time of the Storegga slide (Byrkjeland et al., 2000). Because of the increase in seismic events, earthquake as a triggering mechanism are believed to be the cause of the initiation of the Storegga area (Lindholm et al., 2005). Modeling performed by Lindholm et al. (2005) also showed that the Møre Basin effectively traps seismic energy, causing the duration of ground motion to last longer. Present there is still large earthquake activity in the study area, and the area is considered to be more seismic active than other parts of the Norwegian continental margin (Byrkjeland et al., 2000). Earthquake with magnitude above five have been recorded in Norway in more recent times, the last with a magnitude of 5.3 in 1988 (NNSN[1]). The mechanism behind earthquakes in Mid-Norway are described in detail in Section 2.2.

1.3.1 Previous studies

The Ormen Lange gas field, discovered in 1997, is located at large water depth beneath the scar of the Storegga slide (Figure 1.1) and to ensure safe development of the field, extensively studies on slope stability of especially the headwalls of the slide have been carried out. Before, during and after the development of the Ormen Lange gas field, several studies has been performed concerning the slope stability and possible triggering mechanism. Kvalstad et al. (2005b) developed mechanical models for assessing the slide mechanism concerning strain-softening behavior and performed numerical models and

---

[1] Norwegian National Seismic Network operated by the University of Bergen

field measurement for evaluation of pore pressure generation. Strout and Tjelta (2005) described field measurement of pore pressure and evaluated their significance on slide initiation. Bungum et al. (2005), Lindholm et al. (2005) and Atakan and Ojeda (2005) performed seismicity studies of the Storegga area, but non can conclude if earthquake was the responsible triggering mechanism. Leynaud et al. (2004) performed a finite element analyses for seismic loading, which indicated that a shallow failure (depth of 30m) on gentle slopes could potential be triggered by an earthquake. The Storegga slide had a deeper failure (150-300 meter), and Leynaud et al. (2004) therefore suggest that other preconditioning processes are required for deep failure. They also suggest that excess pore pressure generated by cyclic loading could affect the shear strength in a marine layer (weak layer) leading to failure. Even though several studies have concluded that the Storegga slide most likely was earthquake triggered, the question if the slide really was earthquake triggered and release on very low slope angles, still remains. The slopes in the area today is considered to be stable, and a very strong earthquake are believed to be the only possible mechanism to reactivate new slides (Nadim et al., 2005; Kvalstad et al., 2005a).

1.4 Submarine mass failures

Landslides regularly occur on slopes that have become unstable as a part of the evolution of topography (Kramer, 1996). Submarine mass failures are defined by Kvalstad (2014) as unconsolidated material moving downslope under water. They occur in different environments such as deltas, on the flanks of volcanic islands, in fjords and lakes, and on continental slopes (e.g. Locat et al., 2014). Landslides are commonly characterized by their type of movement and the material in place. Failure of a slope usually starts at a point or in an area, and then moves progressively from that point/area. Typical characteristics of submarine landslides are translational movement. The movement of translational slides often follows discontinuities or planes where the material has a weaker strength than the surroundings (Abramson et al., 1996). Many of the concepts concerning slope stability and factors affecting this will be described throughout the study, but two important factors are described briefly in this section.

Causes for submarine mass failures

Mass failures will in general occur when the resisting forces are smaller than the driving forces as described by many (e.g. Kramer, 1996; Kvalstad, 2014; Abramson et al., 1996; Locat et al., 2014). As already mentioned, several factors can to contribute this, such as erosion, earthquakes and gas hydrates. Generation of excess pore pressure decreases the shear strength of the sediments and is considered the most important factor for mass failure (e.g. Leynaud et al., 2004). Erosion at the toe and deposition on the top of the slope can also cause instability in the slope because it increases the shear stresses.

Earthquake shaking will, in addition to the overlying weight cause compaction and overpressure in unconsolidated sediments, and add additional dynamic stress to the slope on top of the static stress (Kvalstad, 2014). Earthquake shaking can also cause permanent displacement of the slope material, ten Brink et al. (2009) and Newmark (1965) states that if the earthquake shaking causes the slope to be displaced a given distance, this will lead to catastrophic failure.

Pore pressure

Many previous studies (e.g Bryn et al., 2005) describes that generation of excess pore pressure is a common factor for most processes that may affect slope stability. This feature is important because excess pore pressure tends to reduce the strength of a material (Solheim et al., 2007). In between pores in a soil, the pressure that acts on the walls of the grains, are known as the pore pressure. Pore pressure is present in both saturated and unsaturated soils, but for sub sea soil, the saturated soil is most relevant (Strout and Tjelta, 2005) and will be the focus here.

The effective stress controls the behavior of soil, and is therefore shown to be an important concept of slope stability evaluations (Abramson et al., 1996). The effective stress is a function of the total stress and the pore pressure, which makes the determination of pore pressure important (Strout and Tjelta, 2005). The effective stress (σ') can be expressed by

$$\sigma' = \sigma - u \tag{1.1}$$

where u is the pore pressure and σ is the total stresses (Strout and Tjelta, 2005). The pore pressure in a saturated soil can at any point be divided into two components; the hydrostatic pressure u_0 and excess pore pressure Δu (Figure 1.2). The hydrostatic pressure may be calculated by the total unit weight of the fluids above the depth of interest (Strout and Tjelta, 2005).

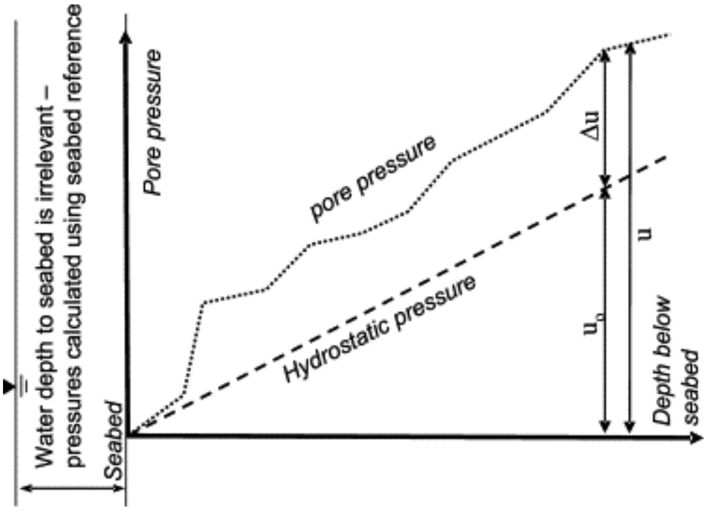

Figure 1.2: Illustration of the pore pressure in a fully saturated soil. The hydrostatic pressure u_0 and the excess pore pressure Δu makes up the total pore pressure u. From: Strout and Tjelta (2005)

Shear strength of soils

A very important term when considering slope stability and slope failures is the shear strength. A change in the effective stress is related to shearing stresses and thus to slope stability through the shear strength of the slope material. Most measurements of shear soil strength are conducted through laboratory measurements. However, it is possible to do some in-situ measurements. The values of shear strength achieved from laboratory measurements, depends upon several factors; method applied, size of sample etc., and especially on the type of soil. The laboratory test will typically reveal stress-strain curves for the soil conditions expected (Abramson et al., 1996).

The shear strength (S) can be expressed as:

$$S = (\sigma - u)\tan\theta \tag{1.2}$$

where θ is the coefficient of friction, u is the pore pressure and σ is the overburden total stress (Talling et al., 2014). Figure 1.3 illustrates the shear strength of soils. The resisting force and the total stress is a function of the effective stress. This means that an increase in the pore pressure (Eq. 1.2), will result in an decrease of the shear strength (Talling et al., 2014; Strout and Tjelta, 2005).

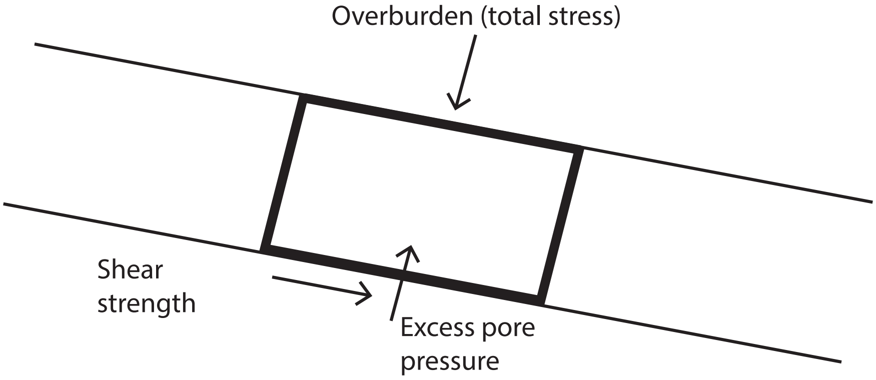

Figure 1.3: Relation between total stress(σ), excess pore pressure (Δu) and shear strength (S) . Modified from: Talling et al. (2014)

Chapter 2

Geological and Tectonical Background

In this chapter I will describe the main events that have contributed to the development of the Norwegian continental shelf. The main focus will be on the events that were crucial for the development of the mid-Norwegian continental shelf, that today are located approximately from 61 to 69°N. The stratigraphy of the study area is briefly described. Last, I will describe the seismicity and the driving forces for earthquakes in Norway.

2.1 Geological evolution of the Norwegian Continental Shelf

Several tectonic episodes have occurred during the geological evolution of Norway, where the main episodes occurred in Silurian to Early Devonian time (Roberts, 2003), Late Paleozoic, late Mid-Jurassic to Early-Cretaceous and Late-Cretaceous to Early-Tertiary time. These episodes involved continental collision, continental rifting and sea floor spreading (Brekke et al., 2000). The main events contributing to the tectonic evolution of the area will only briefly be described here, a more detailed description can be found in e.g. Brekke et al. (2000), Faleide et al. (2010) and Roberts (2003).

2.1.1 The Caledonian Orogeny

One event which had a large impact on the geology in Norway is the Caledonian Orogeny. The Iapetus sea was formed when Laurentia and Baltica moved apart in Precambrian time, but at some point the movement was reversed. This change from divergent to convergent movement later resulted in the major continent collision that is today known as the Caledonian Orogeny (Fossen et al., 2007b).

Four major orogenic events can be identified within the Caledonian Orogeny, in addition to a late event of extensional collapse. The first main event occurred in Late Cambrian to earliest Ordovician time and is named the Finnmarkian event (Figure 2.1.a). This event is assumed to be a result of the collision between the Baltoscandian margin with a magmatic arc, i.e. a continent-ocean collision. 25 million years later, in Lower Ordovician, the Trondheim event occurred (Figure 2.1.b). This event represents a phase of deformation and metamorphism, and involve ocean-ward subduction (Roberts, 2003). Micro-fossils from Ordovicium age suggest that the Baltican plate was subducted (Fossen et al., 2007b). After the Trondheim event, in Mid to Late Ordovician, there was an accumulation of island-arcs named the Taconian event (Figure 2.1.c). The last event was the Scandian event in Late Silurian to Early Devonian time (Figure 2.1.d). This orogenic event is assumed to be a result of the oblique continent-continent collision between the Laurentia and the Baltica plates. Evidence from the presence of the mineral coesite in Norway indicate that this event was of short duration with rapid subduction and exhumation (Fossen et al., 2007b; Roberts, 2003).

In Early-Devonian time the colliding forces disappeared and the continents started drifting apart again. The orogeny lost its side support and collapsed (Fossen et al., 2007a). This gravitational collapse of the orogeny led to several large extensional shear zones (Fossen et al., 2007a; Roberts, 2003).

2.1.2 Rifting events

After the Devonian collapse of the Caledonian Orogeny, the NW Atlantic has experienced several rifting events (Lundin and Doré, 1997). In Carboniferous time, rifting and strike-slip movement started between Norway and Greenland (Nøttvedt and Worsley, 2007). In the Mid-Norwegian Sea this can be seen as a system of horsts and half-grabens of Carboniferous to Late Permian age (Brekke et al., 2000). The super continent Pangea started rifting in Triassic, but in Early Jurassic the area had a period were it was tectonically stable. Reactivations of older rift structures occurred in Late Jurassic (Figure 2.2) , and the rifting propagated northwards (Nøttvedt and Johannessen, 2007). This rifting was probably linked to the rifting in central Europe and the rift system have an North-South orientation implying an East-West-extension (Lundin and Doré, 1997).

The rifting that started in Late Jurassic continued into Early Cretaceous, and resulted in the development of major basins such as the Vøring and Møre Basins (Faleide et al., 2010). The Vøring and Møre Basins have an NE orientation which imply an EW-extension (Lundin and Doré, 1997). This rifting in the Vøring Basin involve the formation of the Fles Fault Complex (FFC in Figure 2.2), and depocenters and synclines that formed

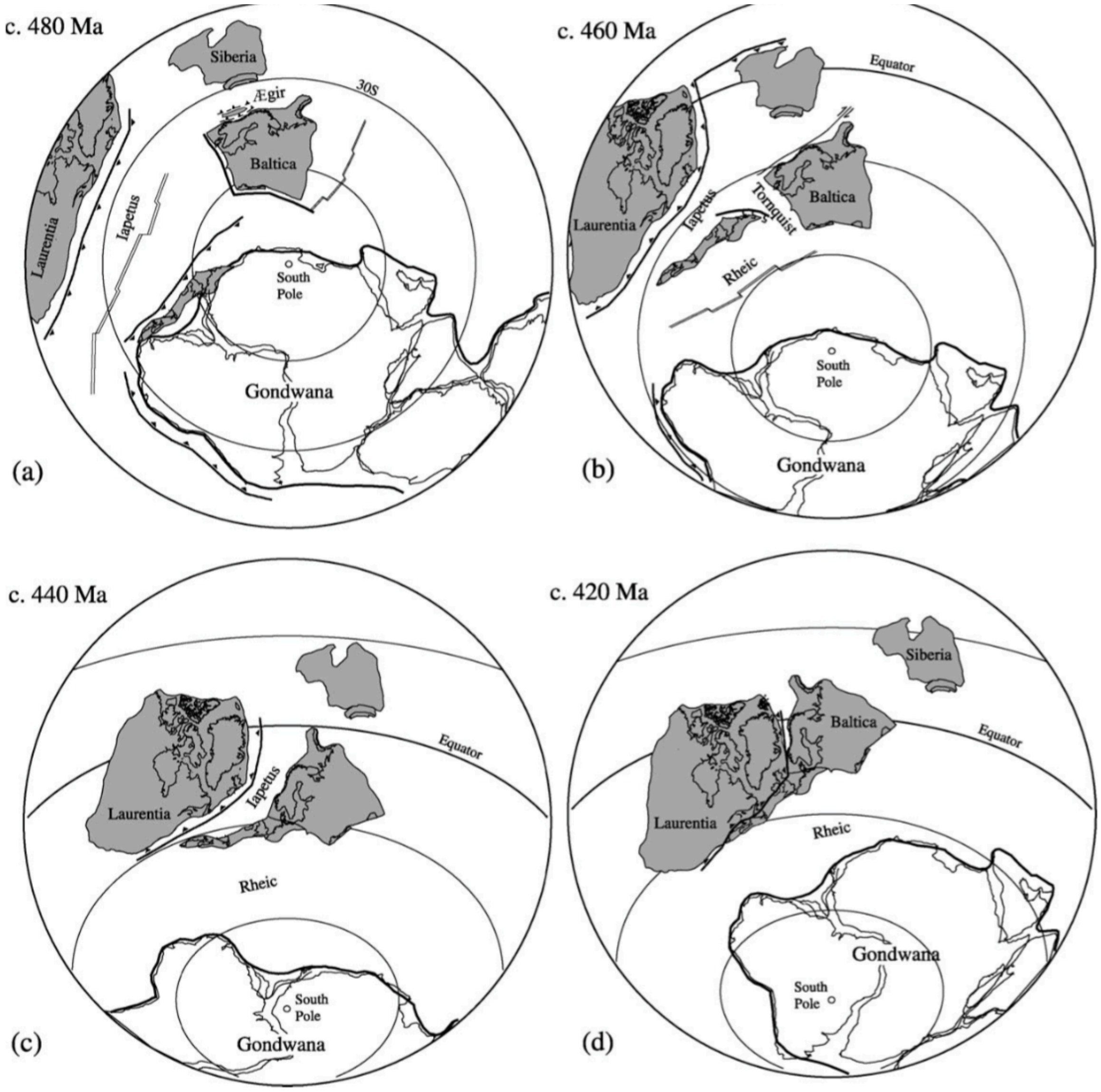

Figure 2.1: The geological evolution of the Caleonian Orogeny. a) The Finnmarkian event - collision between the Baltoscandian margin with a magmatic arc (continent-ocean plate collision) b) The Trondheim event - deformation and metamorphism that involve ocean-ward subduction c) The Taconian event - accumulation of island arcs d) The Scandian event - continent-continent collision between the Laurentia and Baltica plate. From: Roberts (2003)

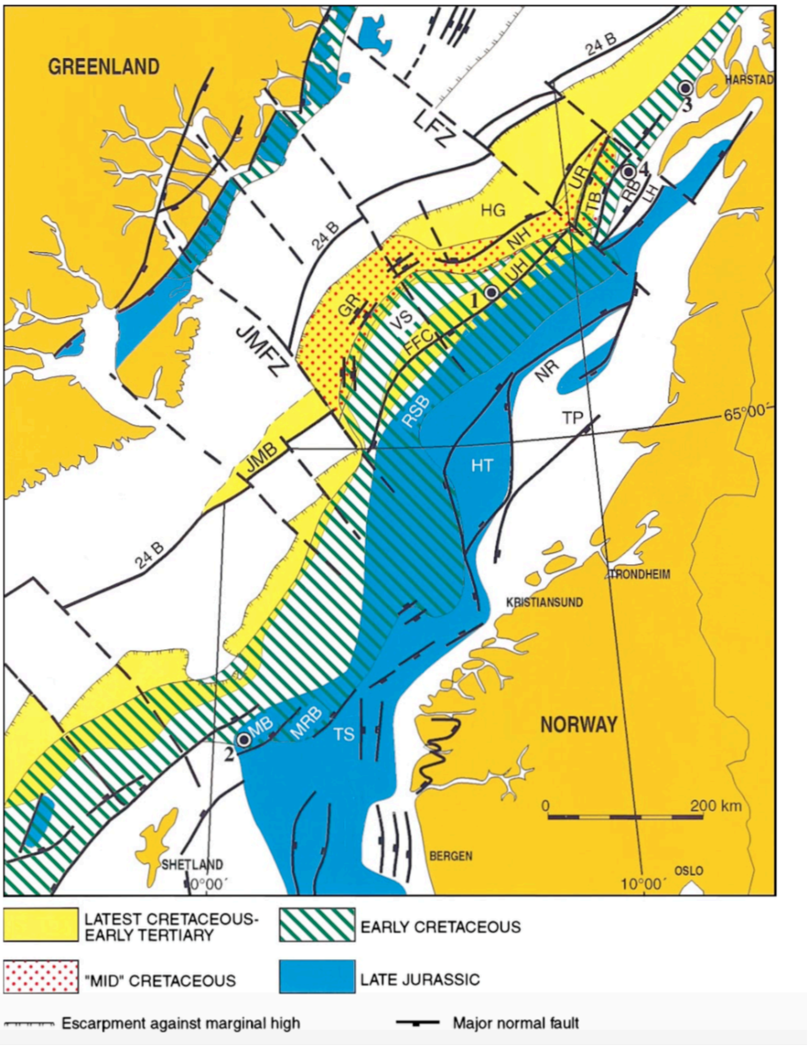

Figure 2.2: Tectonically active areas during different events. FFC -Fles Fault Complex, JMFZ - Jan Mayen Fracture Zone, TP - Trøndelag Platform. From: Lundin and Doré (1997)

several subbasins and highs (Brekke et al., 2000; Faleide et al., 2010). The Fles Fault Complex have experienced several reactivations, and have had a large impact on the tectonic development of the Vøring area. The Møre area also experienced the main tectonic episode during this period, but was probably not as active as the Vøring Basin. The Møre-Trøndelag Fault Complex (Figure 2.3) may have been developed as early as Triassic, but was most active during this period. The Møre-Trøndelag Fault Complex is shown as a set of horsts and half-grabens (Figure 2.3) (Brekke et al., 2000).

The rifting from Late-Jurassic to Early Cretaceous continued to Early Paleogene, and finally led to the continental separation between Norway and Greenland (Brekke et al., 2000; Martinsen and Nøttvedt, 2007). The area has from Early Paleogene to present experienced reactivation of the major lineaments and fault complexes such as the Jan Mayen Lineament in Figure 2.3 (Brekke et al., 2000). Since Middle Eocene time the mid-Norwegian Margin experienced subsidence and moderate sedimentation, and developed into a passive rifted continental margin (Faleide et al., 2010). During Late Miocene the area experienced regional onshore uplift, which resulted in a coastal progradation (Faleide et al., 2010; Ottesen et al., 2009).

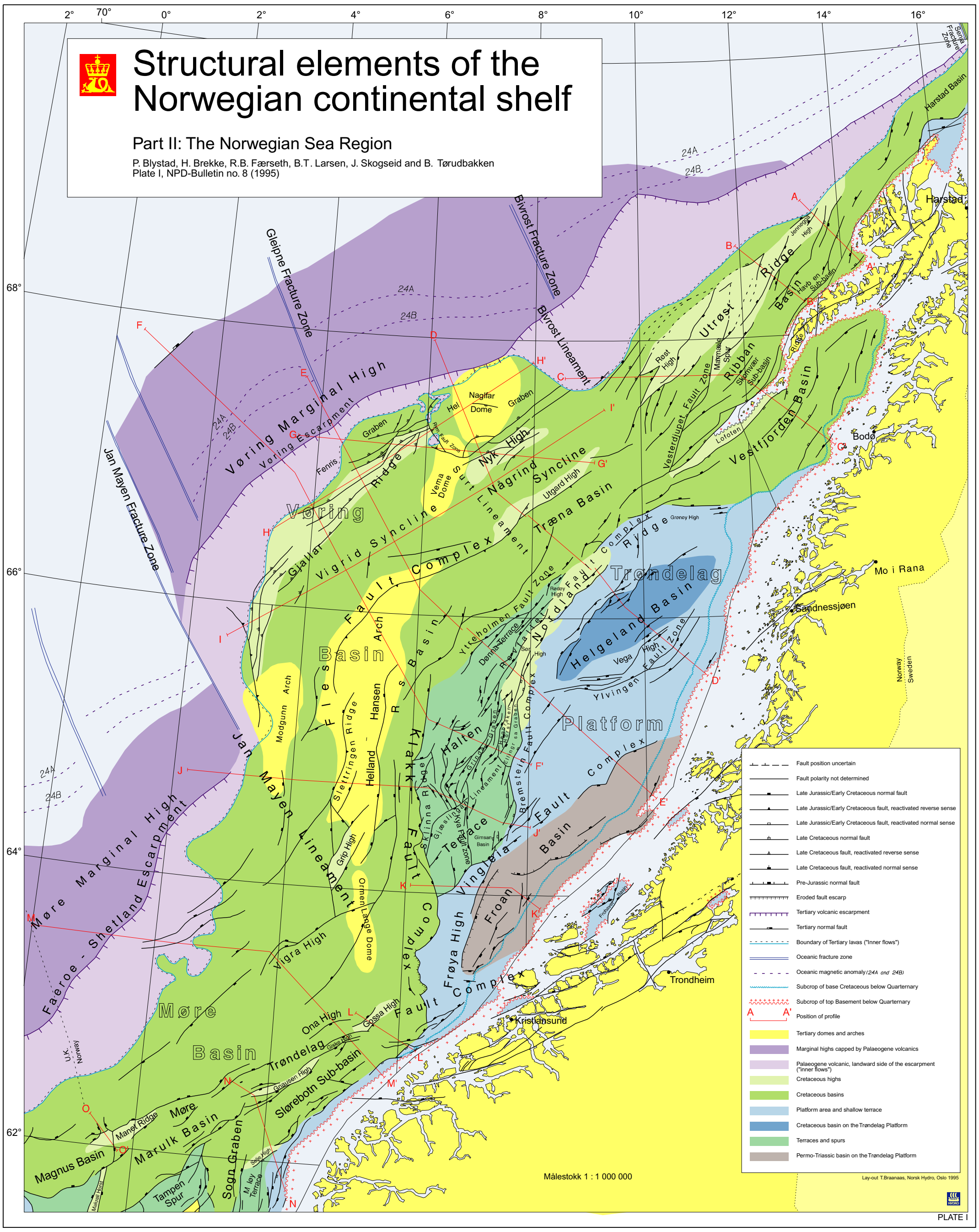

Figure 2.3: Structural map of the Norwegian Continental Shelf. From: Blystad et al. (1995)

2.1.3 Stratigraphy

The morphology of the mid-Norwegian continental shelf seen today is mostly a product of rapid progradation of the shelf during the last 3 Ma (Pliocene to Pleistocene). The progradation is a result of several glaciations (Rise et al., 2005). Shallow banks separated by troughs characterize the Mid Norwegian Continental Shelf. These troughs acted as paths for fast-flowing ice streams during the glaciations. Among these troughs is the Norwegian Channel, which is a major geomorphological feature in the North Sea/ southernmost part of the Norwegian sea (Ottesen et al., 2009).

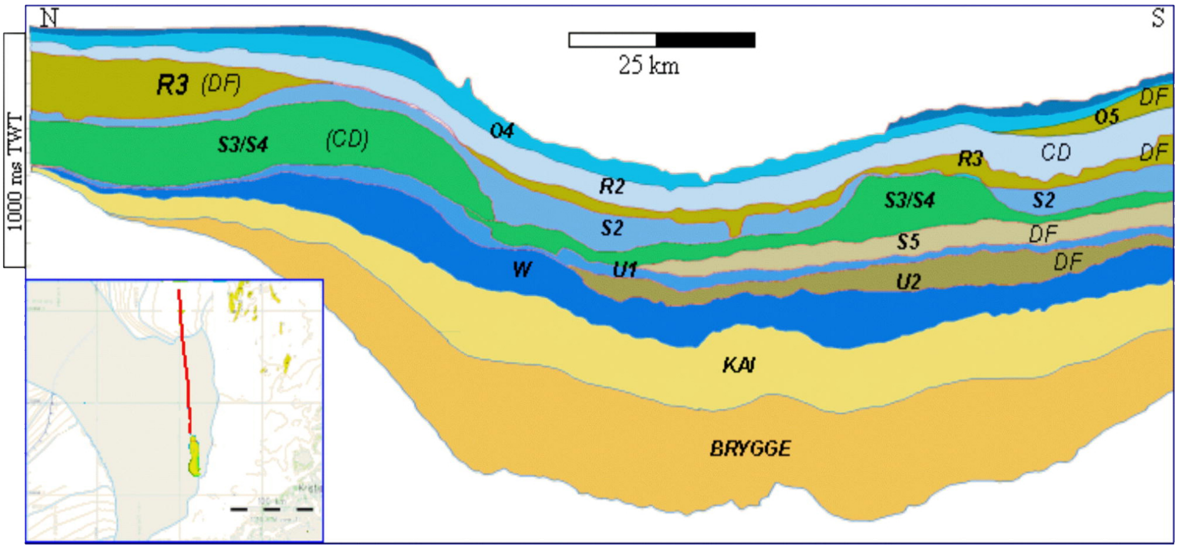

Figure 2.4: Stratification of the Naust Formation with subunits W, U, S, R, O overlying the Kai and Brygge Fm. The Nasut Fm. have been given new names in later times, and are now named respectively N, A, U, S, T (Carl Fredrik Forsberg, pers. comm.). Modified from Berg et al. (2005)

The mid-Norwegian shelf and margin is divided into four regions according to Bryn et al. (2005); the steep Lofoten margin (where the Trænadjup slide occurred), the Vøring plateau, the Storegga region and the North Sea Fan region (Figure 1.1).

The Naust Formation (Fm.) (Figure 2.4) defines the overall seismic stratigraphy of the mid-Norwegian margin. The formation is divided into five main sequences, where each are related to the main glaciations. The stratigraphy of Naust Fm. consist mainly of marine clay and glacial diamictons (Berg et al., 2005). Peak glaciations represent the shortest time period of the glacial-interglacial cycle, but during this time the ice could reach out on the shelf break (Berg et al., 2005). Glacial sediments in the study area have mainly been deposited during this period by fast flowing ice streams (e.g. Rise et al., 2005; Hjelstuen et al., 2005), and was moved further out on the continental slope by debris flows (Berg et al., 2005). The North Sea Fan is the most significant of these deposits with a thickness up to 1700meters (Nygård et al., 2005). The glacial sediments were also deposited by debris flows during the longer interglacial periods, marine or hemipelagic fine-grained sediments were deposited (Berg et al., 2005).

The Naust Fm. is overlying the fine-grained oozes of the Brygge and Kai Fm. The Brygge Fm. are a sequence of siliceous ooze, having a thickness of 1500meters in the main depocentre, 600-1000meters in the North Sea Fan and less than 400meters on the Vøring Plateau. Contouritic deposits define most of the Kai Fm. and have a thickness of 1000meters in the main depocentre located in the Northern flank of the Storegga slide area. Towards the central parts of the Storegga area the contouritic sediments are absent or very thin (Bryn et al., 2005).

2.2 Seismicity of Norway

In this section I will describe the seismicity of Norway. ten Brink et al. (2009) suggested that if earthquakes should be responsible triggering a submarine landslide, the earthquake should occur relatively close to the release area of the slide. This is the case even for large magnitude earthquake, and I will therefore focus my description on the seismicity close to the study area. Last, I will discuss the mechanisms that contribute to stress build-up in Norway.

The seismicity rates in Norway are the highest in northern Europe, but on a global scale, the seismicity rate is seen as low to intermediate (Bungum et al., 2005; Olesen et al., 2013). The most seismically active areas in Norway include the coastal part of western Norway, Nordland and the Oslo rift zone. In these areas, earthquakes with magnitude 6 and above is possible due to the dimensions of faults located in the area. Earthquake with a magnitude of this size can pose a significant hazard to the society in Norway due to the potential triggering of rock avalanches and landslide, that in turn could generate tsunamis in fjords and on the continental slope (Olesen et al., 2013).

Figure 2.5 shows earthquakes that occurred in Norway and surrounding areas from 1900 to November 2017. This representation of earthquakes makes it clear that the highest occurrence of earthquakes is located in the Oslo area and along the coast of Norway, with a highest occurrence in Western Norway (NNSN). Presently there is a relatively high seismicity in the Norwegian and Barents Sea, believed to be caused by present tectonic processes (Olesen et al., 2013; Bungum et al., 2005). Mainland Norway have experienced several earthquakes with magnitudes above 5, where the largest registered in the earthquake catalog is the Oslo magnitude 5.4 in 1904 (NNSN). Offshore western Norway, two earthquakes with a magnitude greater than 5 occurred in 1988 (M5.3) and 1989 (M5.1) (Bungum et al., 2005). The Stuoragurra fault in Finnmark is believed to be created right after a deglaciation by an earthquake with magnitude greater than 7. The seismicity rates in Fennoscandia indicates that there is expected one M5 every 10 years and one M7 every 1100 years (Bungum et al., 2005), however this assumption is uncertain due to the long return period.

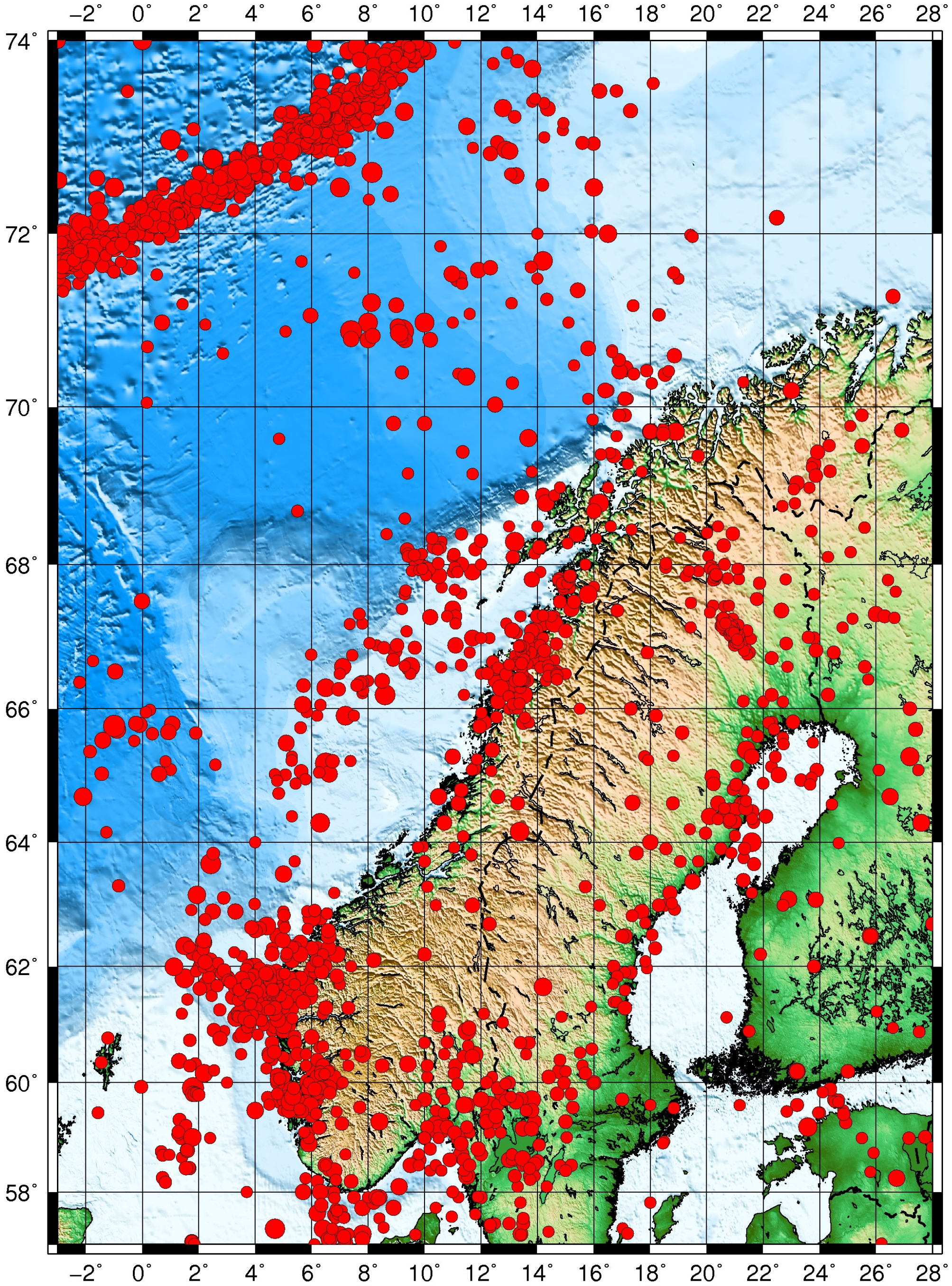

Figure 2.5: Earthquakes in Norway and surroundings from 1900 to November 2017. Sizes of red dots indicate magnitude of event (Earthquake catalog retrieved from NNSN).

Table 2.1: Stress generating mechanisms divided in groups based in the extent of their stress field. From: Fejerskov and Lindholm (2000)

Stress Field	Continental	Regional	Local
Lateral extend	>1000km	100-1000km	<100km
Stress-generating mechanisms	Plate tectonic forces: Ridge push Slab pull Basal drag	Large-scale density inhomogeneities: Continental margin Flexural stresses: Deglaciation Sediment loading Topographic loads	Topography: Fjords and Mountain ranges Geological features: Faults Hard and soft inclusions

Norway is a passive continental margin, and have several (failed) rift zones, as described in section 2.1.2. In stable continental regions; rifted passive margins and failed rifts are the main types of structures that can host large earthquakes. Earthquakes that occur in intra-plate environments usually follow preexisting zones of weakness and result from a build-up of stress and a reduced shear strength along faults in the same direction (Bungum et al., 2005; Olesen et al., 2013).

Several major structures have recently been mapped and shown to have capabilities to accommodate M6.5-7 earthquakes without breaking the surface. As the largest historically known earthquake in Fennoscandia only being a magnitude 5.8 earthquake, there is a possibility that the maximum magnitude in this area may exceed this (Bungum et al., 2005).

Stress generating mechanisms

Several mechanisms can contribute to stress build-up in Norway. The mechanisms that generates stress can be identified by their origin and lateral extent, and is divided into continental, regional and local stress field (Table 2.1). In the Norwegian region the major stress field is caused by the ridge push force on continental scale and regional density inhomogeneities, topographic loads, plate flexure and sediment loading on regional scale (Fejerskov and Lindholm, 2000).

Mid ocean ridges, or spreading zones, are areas that are approximately in isostatic equilibrium. The crust is elevated due to heating from underneath, but is compensated at depth by hot and low density material. The oceanic lithosphere cools down and subsides when it moves away (and ages) from the mid ocean ridge. Because of the elevation of the ridge, there is induced an outward compressional force that is perpendicular to the crest of the ridge. This force is generated by gravity and is an apparent horizontal force (Engelder and Price, 1993), and is zero at the ridge crest (Fejerskov and Lindholm, 2000). The magnitude of this force will increase with age, but decrease with depth. For 60 Ma old crust the magnitude of this force is 20-30MPa. The ridge push force is the main stress generating mechanism in Fennoscandia (Fejerskov and Lindholm, 2000). The study area is located close to an area with thinned crust and can therefore locally experience higher magnitude of deviatoric stress (Figure 2.6.a).

The continental and the oceanic crust have different densities, due to this stress can be generated from the continental margin. Extensional stresses in the continental crust and compressional stresses in the oceanic crust can be generated due to the continental crusts tendency to spread out over the oceanic lithosphere. When only the effect of the continent is considered the stress will act normal to the margin. The stress orientation can change when other forces contribute. It has been shown that the stress orientation is dependent on the angle between the continental crust and the ridge push force. The force has a higher magnitude where the continental margin is oriented parallel, as in the Norwegian sea, to the far-field stress, i.e. parallel to the stress direction of the ridge push force. This can explain the change in stress direction from WNW-ESE in western Norway to NW-SE direction in mid-Norway (Fejerskov and Lindholm, 2000). The maximum deviatoric stress have been computed by Stein et al. (1989) to 40-50MPa close to the slope of the margin. The forces will decrease with depth and distance from the margin.

Stresses can be introduced by the load or unloading of glaciers or ice sheets in the upper crust. This is referred to as glacial rebound and/or flexural stresses related to deglaciations. Two models have been proposed for the calculation of the horizontal stresses related to flexural stresses (Fejerskov and Lindholm, 2000). The first model of Stephansson (1988) assume that if the crust is at isostatic equilibrium before the load of ice, the ice sheet will push the lithosphere down. This will cause compressional stresses under the ice and extensional stresses on the side of the ice. When the ice is removed, there will be a following uplift to reach isostatic equilibrium, where the stresses will decrease until equilibrium is reached. The second model (Figure 2.6.c) by Stein et al. (1989) assume the plate is in equilibrium with ice load. This will cause the stress direction related to uplift from deglaciation to be the opposite of the first model. The first model will calculate stresses with magnitudes of 3-4MPa for a 2km thick ice sheet, while the second model calculated a magnitude of 30MPa. The model that should be applied depends thus on the glacial history for the region of interest (Fejerskov and Lindholm, 2000).

The same principle as for ice loading applies for flexural stresses from sediment loading. There will be compressional stresses at the top and extensional stresses to the side

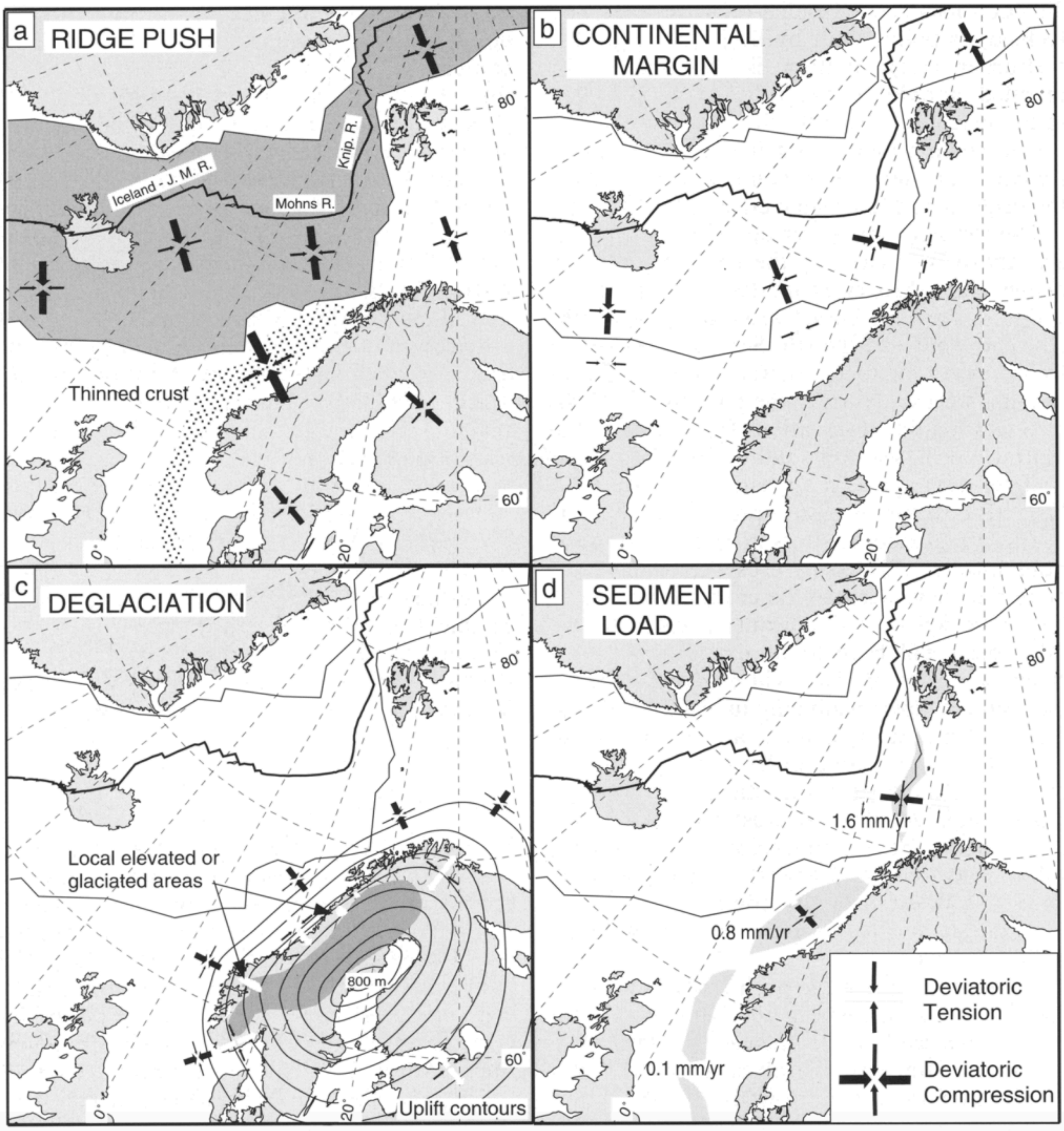

Figure 2.6: Overview over the main driving mechanism for stress build-up in the Norwegian region. a) Ridge push from the mid-Atlantic spreading ridge. The stress field induces has a NW-SE direction and have a magnitude of 20-30MPa in the oldest oceanic crust. b) The continental margin induce a stress field acting normal to the margin. Tensional stress field are induced in the continental crust and compression stress field in the oceanic crust. c) Post-glacial uplift according to the model of Stein et al. (1989). Areas former glaciated show tension, while areas beyond the ice edge show compression. d) Bending stresses developed as a response to sediment loading, the magnitude of these stresses are dependent on sedimentation rate. Beneath the load compression is present, while tension is present on the flanks of the load. From Fejerskov and Lindholm (2000).

of the basin according to the model of Stein et al. (1989). This models predict stress with magnitudes of several 100MPa for an elastic place, but reduces to tens of MPa if considering a brittle-ductile behavior. Stein et al. (1989) also concluded that basins with a high sedimentation rate over a thin lithosphere will have the highest stresses. In late Neogene time there is indications of strong erosion due to uplift of onshore areas in mid-Norway. This is seen as a thick prograding sequence, as pointed out in section 2.1. In Pliocene time there was a sedimentation rate of up to 0.8mm/yr in the area (Figure 2.6). This high sedimentation rate could have been sufficient to cause flexural stresses and thus seismic activity on the mid-Norwegian shelf (Fejerskov and Lindholm, 2000).

Topography, i.e. high altitude mountains, will represent a similar load on the plate as both the ice- and sedimentation load. In mid-Norway, the effect from topography can therefore influence the near-surface stresses onshore (Fejerskov and Lindholm, 2000).

Focal mechanisms and Focal depth

The focal depth and focal mechanisms in the study area are hard to determine due to the sparse coverage of seismic stations. While the stations should be within twice the focal depth, the distance from station to epicenter is often between 200-400km. However, the focal depths show a tendency of increasing depth from onshore to offshore. To obtain a good resolution on the focal mechanism, the stations should ideally be distributed around the epicenters. Stations in Norway are distributed on the mainland, which give a low resolution on focal mechanisms of earthquakes offshore. Therefore, all focal mechanism and focal depth will only be an indication of the stress-regimes (Lindholm et al., 2000).

Figure 2.7 present an overview over the focal mechanisms determined for different areas in Norway. The northern North Sea shown the principal horizontal stress direction (σ_H) as WNW-ESE. Mid-Norway have a slightly clockwise rotation of the σ_H compared to the northern North Sea and have a direction of NW-SE. These directions of σ_H is consistent with the overall stress regime when assuming that the ridge push force is the principal stress-generation mechanism (Lindholm et al., 2000; Fejerskov and Lindholm, 2000).

In the northern North Sea, the dominant faulting style is reverse and oblique strike-slip, which indicates a compressive stress regime. Both normal and reverse faulting is observed with NW-SE σ_H in Mid-Norway area (Lindholm et al., 2000).

There is a general high correlation between the main faults and seismic activity. The deeper offshore faults have a reverse trend, while the shallower onshore faults have a normal trend (Lindholm et al., 2000; Fejerskov and Lindholm, 2000).

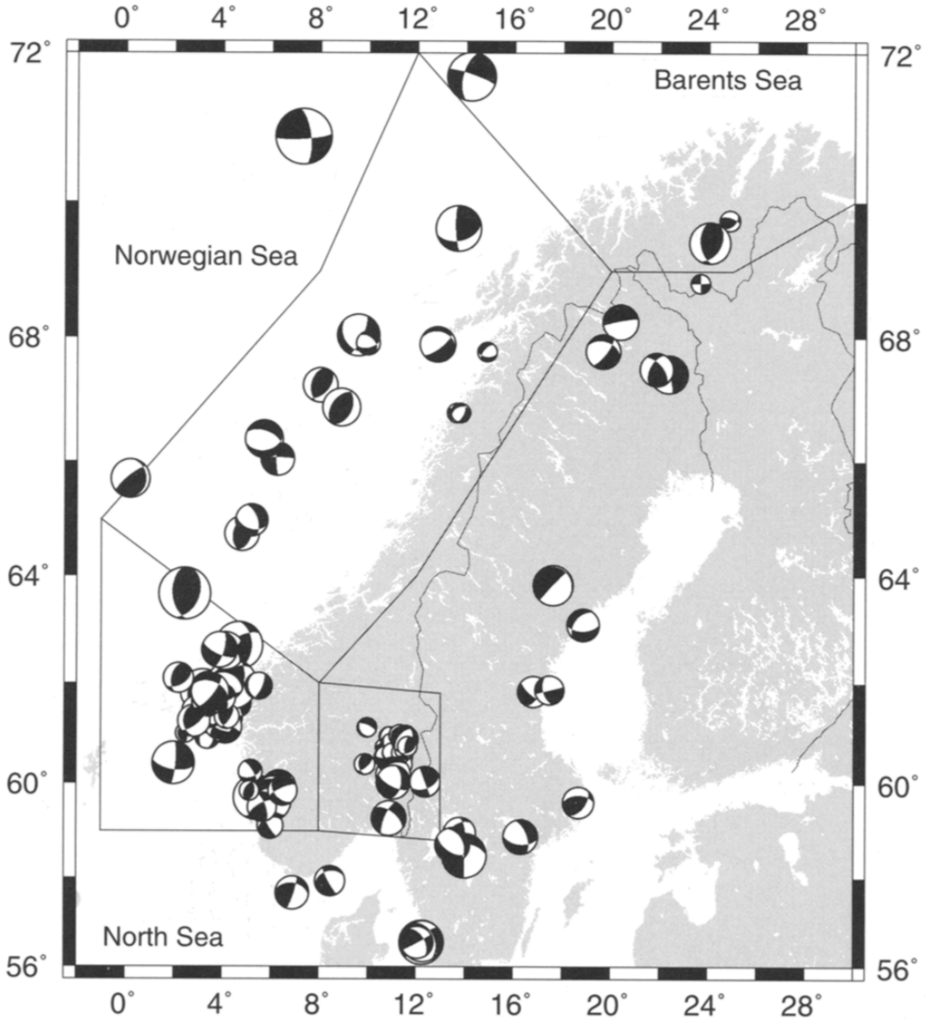

Figure 2.7: Overview of the focal mechanism in the Norwegian region. The map is divided into main stress regimes, where the stress field located to SW are close to the study area. In the study area the focal mechanism show a trend towards reverse and oblique strike-slip. From Lindholm et al. (2000).

Chapter 3

Methods

In this chapter I will describe methods used for modeling ground motion and site response, and the evaluation of slope stability. First, the calculation of maximum distance from source to site will be explained. The program EXSIM12 and DEEPSOIL have been applied for ground motion modeling and site response evaluation, and the theory behind these programs will be described. Last, the analysis for seismic slope stability are explained.

3.1 Maximum distance from fault to site

To obtain a general overview over the possible sources for earthquakes in the study, the maximum distance from expected failure to fault has been computed. The method applied for the computation is derived from the pseudo-static analysis of seismic slope stability, described in section 3.4.2, and are based on the computation of the critical acceleration (ten Brink et al., 2009). The critical acceleration is the level of acceleration assumed to be required in order to affect the stability of a slope (Kramer, 1996).

The study area has a huge number of structural elements and faults that may have been reactivated in the past, and possibly can be reactivated in the future. A method presented by e.g. ten Brink et al. (2009) have been used to calculate the maximum distance from source to site. This method relates the magnitude of earthquakes to the distance from the fault to failure location. Slope stability is sensitive to horizontal acceleration induced by earthquake (Kramer, 1996), therefore we want to find an acceleration value that is critical for the stability of the slope.

The method assumes that mass failures in soft sediments triggered by earthquakes, may occur when the undrained shear strength S_u of the sediments is exceeded by the shear stress τ on a slip surface (e.g. Locat et al., 2014). This condition can be expressed by the Factor of Safety (FoS) as described in section 3.4.1.

$$FoS = \frac{S_u}{\tau} \leq 1 \tag{3.1}$$

The following description for calculating the critical acceleration is a summary from ten Brink et al. (2009). A pseudo-static representation of the downslope shear stress can be expressed as:

$$\tau = \gamma^{'} z \sin\beta \cos\beta + k\gamma z \cos^2\beta \tag{3.2}$$

where β is the slope inclination (or slope angle), z is the thickness of the potential failure mass, k is the horizontal earthquake acceleration and γ' is the submerged unit weight of the potential failure mass in the slope and γ is the unit total weight of the potential slide.

This representation is a sum of two terms:

- The downslope component of gravitational stress
- Pseudo-static horizontal stress related to earthquake loading

A slope can be defined on the brink of failure when $FoS \leq 1$, therefore the failure conditions can be set as $FoS = 1$ which yields

$$S_u/(\gamma^{'} z) = \cos\beta \sin\beta + k(\gamma/\gamma^{'}) \cos^2\beta \tag{3.3}$$

where $S_u/(\gamma^{'} z)$ is defined as the c/p-ratio.

Rearranging Eq. 3.3 will express the earthquake acceleration at which the pseudo-static stress equals the shear strength,

$$k_y = \frac{(\frac{c}{p})(\frac{\gamma^{'}}{\gamma})}{\cos^2\beta - (\gamma'/\gamma)\tan\beta} \tag{3.4}$$

where β is the slope angle. k_y is the yield coefficient or the critical acceleration. This critical acceleration corresponds to the acceleration required to affect the stability of slopes in a way that failure may occur. This means that the earthquake acceleration has to be equal to or exceed the k_y to overcome the shear strength of the sediment. Also, the slope has to be displaced a finite distance by the earthquake shaking to cause a catastrophic failure (Newmark, 1965).

A slope failure will not only be affected by the pseudo-static condition described above, the the earthquake acceleration and the duration will also affect slope stability. Maximum acceleration from an earthquake rarely occur in the direction of a slope failure, the response of the ground may therefore be a non-linear result. This non-linear response can be dependent on temporary build up of pore pressure (Newmark, 1965), the magnitude of shaking (Makdisi and Seed, 1978) and variations of shaking with depth.

Faults are rarely located at the same location as the area or point of failure. Therefore, the earthquakes hypocenters may be located at a distance from the area of failure. Because ground motion will be attenuated with distance, the acceleration from earthquakes may be above or below the critical acceleration at various distances from the failure area. Ground motion prediction equations, or attenuation relationships, have therefore been used to calculate the peak ground acceleration as a function of magnitude and distance. Ground motion prediction equations (GMPE) are equations that relates parameters describing the earthquake source, the path waves are traveling and site effects to ground motion intensity measures (Douglas, 2003). Because no GMPE have been derived for Norway, GMPEs from a similar tectonic area has been applied. Norway is, as described in section 2.2, a stable continental region, and similar to the Eastern North America (ENA) region. Two GMPEs derived for ENA has therefore been applied here. The Hybrid Empirical method is used for developing GMPEs where few strong-motion recordings are available. The first GMPE applied was derived by Campbell (2003) given as:

$$\ln Y = c + f_1(M) + f_2(M,r) + f_3(r) \tag{3.5}$$

where f_1, f_2 and f_3 are functions that relates magnitude and closest distance to fault rupture. The c-values are regressions coefficients chosen based on the fundamental period.

Several GMPEs have been developed for ENA after the one from Campbell (2003). The second GMPE that was applied, are a more recent developed GMPE, derived by Shahjouei and Pezeshk (2015) given as:

$$\begin{aligned}\log \overline{Y} =& c_1 + c_2\boldsymbol{M} + c_3\boldsymbol{M}^2 + (c_4 + c_5\boldsymbol{M}) \times min[\log(R), \log(60)] + \\ & (c_6 + c_7\boldsymbol{M}) \times max[min\left\{\log(R/60), \log(120/60)\right\}, 0] \\ & + (c_8 + c_9\boldsymbol{M}) \times min[\log(R/120), 0] + c_{10}R\end{aligned} \tag{3.6}$$

where $R = \sqrt{R_{RUP}^2 + c_{11}^2}$, R is the Joyner-Boore distance (Figure 3.1), M is the moment magnitude, and c are the regression coefficients. This equation is valid for magnitudes between 5 and 8, and a Joyner-Boore distance for 2 to 1000km (Shahjouei and Pezeshk, 2015).

Sediments may cause an amplification of the peak spectral acceleration (PSA). Boore and Joyner (1997) derived an amplification factor of 3.5 for average rock sites, that have been used for the calculations in this thesis. T_s in Eq. 3.7 is the fundamental period. The maximum distance to failure with respect to the slope angle can now be estimated with

$$0.15 \times 3.5 \times K_{PSA(T_s=0.75)} \leq K_y \tag{3.7}$$

The MATLAB -script for these computations can be found in Appendix A.

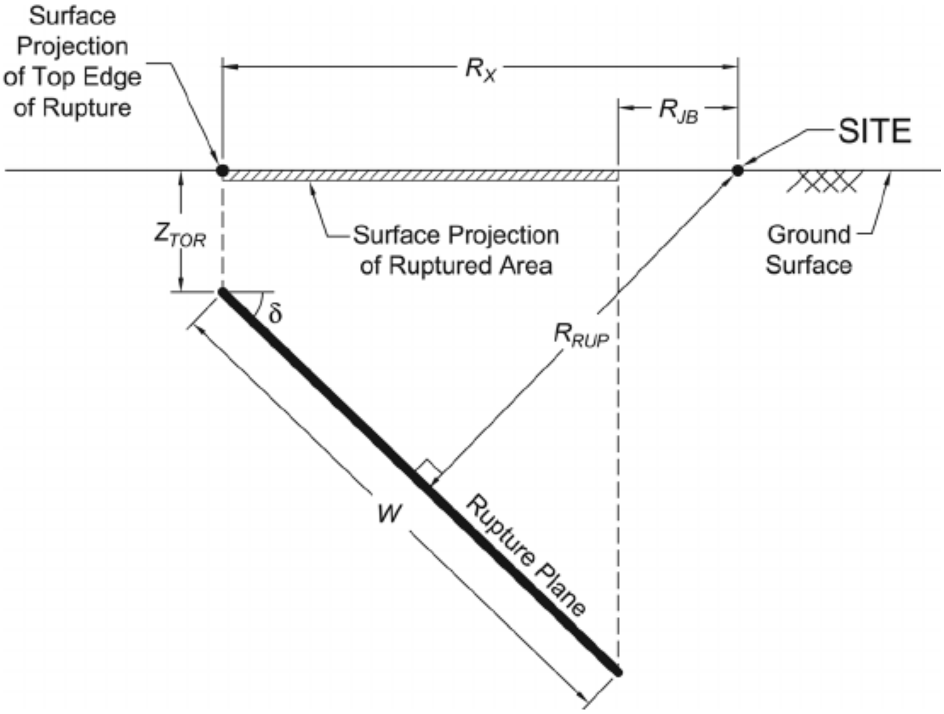

Figure 3.1: Figure illustrating the distances used in the GMPEs. Campbell (2003) uses a distance dependent on R_{RUP}, while Shahjouei and Pezeshk (2015) uses the Joyner-Boore distance (R_{JB}). From: Kaklamanos et al. (2011).

3.2 The stochastic method - EXSIM12

In this section I will describe the stochastic finite-fault model used to model ground motion at bedrock level. In the modeling done in this thesis the bedrock is defined as the depth in the sediments where there is a large contrast in seismic velocity. I have used the FORTAN-based program EXSIM12. EXSIM12 is an stochastic finite-fault modeling algorithm that can be used to generate times series of ground motion for earthquakes (Motazedian and Atkinson, 2005).

EXSIM12 is a further development of FINSIM and SMSIM. SMSIM is a point-source model, and consider the contribution from the entire fault as being radiated from a point. FINSIM and EXSIM12 extend the model to consider a finite fault rupture by dividing the fault into a number of subfaults (N) which each is considered a point-source. The ground motion is the sum of the contributions from each subfault (Figure 3.2) (Motazedian and

Atkinson, 2005).

The point-source method provides appropriate results at large distances compared to the fault dimensions. However, at sites closer to the source, the finite-fault effect become significant. When the fault dimension is large compared to the distances, the effect of directivity, must be considered (Beresnev and Atkinson, 1998). The need for considering these effects led to the development of the finite fault methods, FINSIM and EXSIM.

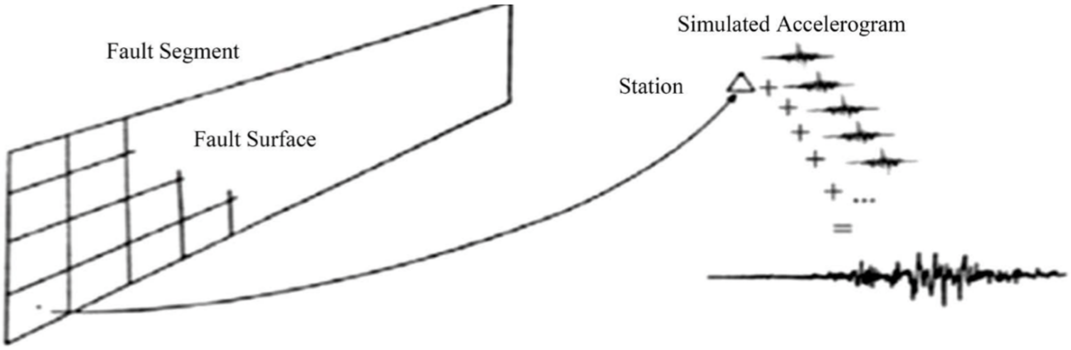

Figure 3.2: Illustration of the finite-fault method. The squares represent subfaults, which each contribute to acceleration. The acceleration from each subfault is then summed to represent the accelerogram from the finite fault. From: Amiranlou et al. (2016)

The point-source method of Boore (2003), which is the basis for all three algorithms, will create a random-phase time series at an observation point for a specified point source at a specified distance (Atkinson and Assatourians, 2015). The process (illustrated in Figure 3.3) has been divided into steps by e.g Atkinson et al. (2009) and Atkinson and Assatourians (2015) and listed as the following:

1. A normally distributed random signal with zero mean and unit variance is generated (Figure 3.3.a).

2. A window function of a specified duration gets multiplied by the noise (Figure 3.3.b).

3. The windowed signal is Fourier transformed from the time-domain to the frequency-domain (Figure 3.3.c).

4. The results are normalized so that the root mean square (RMS) amplitude spectrum of the noise signal equals unity (Figure 3.3.d).

5. The theoretical point-source spectrum as a function of frequency is calculated by Equation 3.8.

6. The normalized noise spectrum is multiplied by Equation 3.8 to obtain the Fourier spectrum of the motion at site (Figure 3.3.e).

7. The last step is the inverse Fourier transform of the site spectrum. This will provide the simulated accelerogram (Figure 3.3.f).

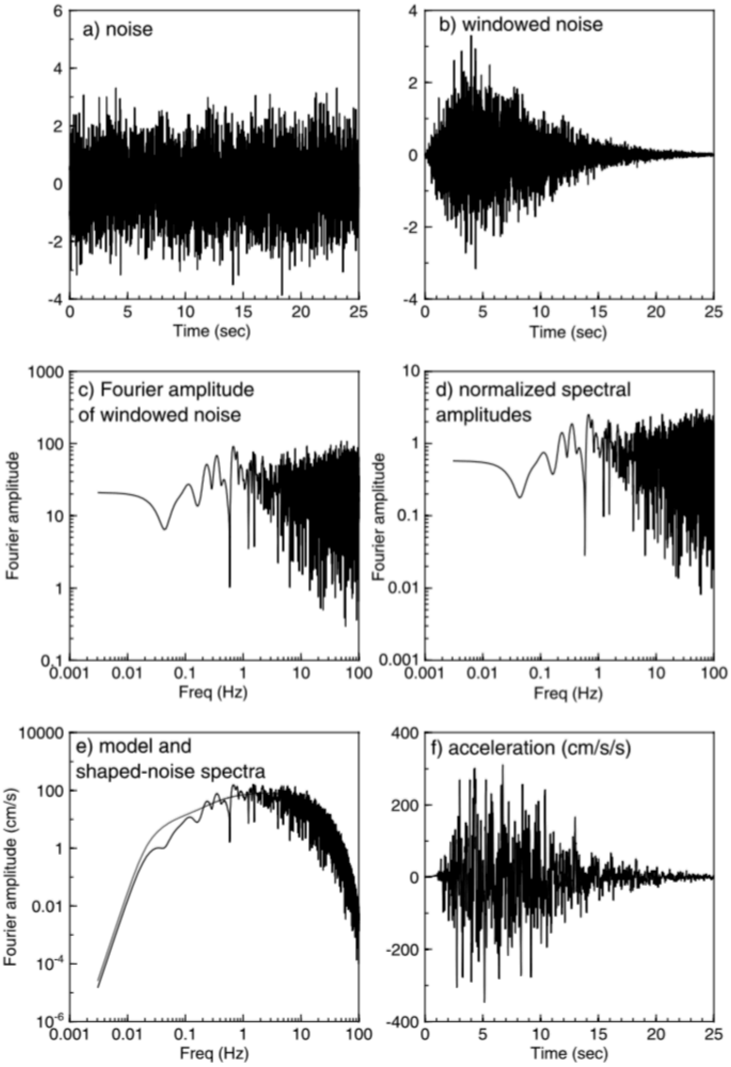

Figure 3.3: Illustration of the steps in the stochastic point-source method. From: Boore (2003).

The Fourier spectrum at the observation point, is given by Eq. 3.8:

$$Acc(M_0, R, f) = Source(M_0, f) \times Path(R, f) \times Site(f) \tag{3.8}$$

where M_0 is the moment magnitude, f is the frequency and R is the distance from the point-source to the observation point (Figure 3.4) (Atkinson and Assatourians, 2015). The main difference between the point-source method to the finite fault-method is how the three terms and their parameters in Equation 3.8, is defined.

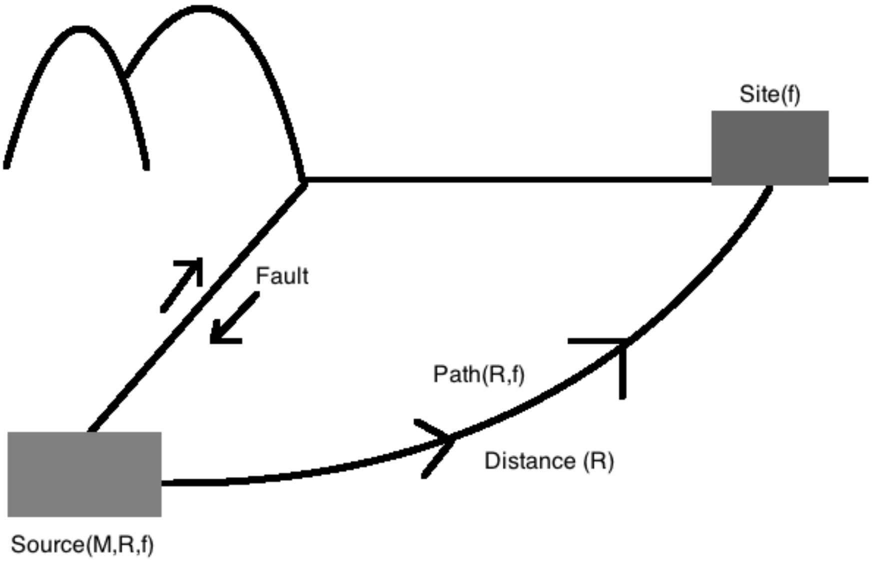

Figure 3.4: Illustration of Equation 3.8. The acceleration recorded at a site are dependent on the source (fault), the path (and distance) the waves are traveling and the local site conditions. Modified from: Kramer (1996)

The first term of Equation 3.8, when considering the finite fault method, concerns the source spectrum and is given by Equation 3.9, M_0 is the source moment, f is the frequency and f_0 is the corner frequency, defined in Equation 3.10 (Atkinson and Assatourians, 2015). C is a constant that involves parameters which account for effects such as the radiation pattern, free-surface effect, and the partitioning of energy into two horizontal components (Kramer, 1996).

$$S(f) = \frac{CM_0 4\pi^2 f^2}{1 + \frac{f^2}{f_0^2}} \tag{3.9}$$

The definition in the point-source method is given by $f_0 = (4.9 \times 10^6) + 6V_s(\Delta\sigma/M_0)^{1/3}$, where $\Delta\sigma$ is the stress drop, M_0 is the seismic moment and V_s is the shear-wave velocity (Boore, 2003). However, the subfault size was a problem in earlier algorithms due to the energy not being conserved when changing the size of subfaults in the above definition (Motazedian and Atkinson, 2005). The concept of dynamic corner frequency was therefore introduced by Motazedian and Atkinson (2005), and make the simulations insensitive to subfault size.

The dynamic corner frequency for the ij^{th} subsource is a function of the cumulative number of ruptured subfaults at time t, $N_R(t)$, defined in Equation 3.10 as:

$$f_{0ij}(t) = N_R(t)^{-1/3}(4.9 \times 10^6) + 6V_s(\Delta\sigma/M_{0ave})^{1/3} \tag{3.10}$$

where $\Delta\sigma$ is the stress drop, V_s is the shear wave velocity and $M_{0ave} = M_0/N$ is the average seismic moment of ruptured subfaults (Motazedian and Atkinson, 2005).

In a real earthquake rupture, the entire fault will not rupture all at once, and the rupture will develop over the fault plane with time. This can be taken into account by assuming that only some of the subfaults are rupturing at any time. When rupture is initiated the subfaults that are active at a time will follow the direction of the overall rupture direction, this is referred to as pulsing. Only the subfault that are actively pulsing will then contribute to the ground motion, and the passive subfaults will not affect the dynamic corner frequency. The active/passive pulsing is taken account for by the parameter N_R in Equation 3.10. At the beginning, N_R will increase with time and then be constant at a fixed percentage after some time (Motazedian and Atkinson, 2005). This fixed percentage is later referred to as the pulsing percentage.

The second term of Equation 3.8 concerns the path ($Path(R, F)$) the seismic waves are traveling from the source to the site of observation. This term describes the attenuation of ground motion from the subsource to the observation site. Several attenuation models can be applied, where the simplest is a linear model defined in Equation 3.11.

$$P(f) = \frac{e^{-\gamma(f)R}}{R} \tag{3.11}$$

where R is the hypocentral distance and $\gamma(f)$ is inelastic attenuation which is inversely related to the quality factor Q (Atkinson and Assatourians, 2015) as:

$$\gamma(f) = \frac{\pi f}{QV_s} \tag{3.12}$$

The third, and last, term of Equation 3.8 concerns the site amplification $Site(f)$. Typically, this term includes two components where the first describe how the seismic waves are affected when propagating through the regional crust, and the second describes any high-frequency deamplification effects from near-surface materials (Atkinson and Assatourians, 2015). For this part of the modeling, DEEPSOIL, described in the next section, will be applied.

Based on Equation 3.8 and the following equations, we can compute the contribution from each subsource separately (Equation 3.13). The acceleration spectrum of the ij^{th} subsource can be defined as:

$$A_{ij}(f) = CM_{0ij}H_{ij}(2\pi f)^2/[1 + (f/f_{0ij})^2] \tag{3.13}$$

where M_{0ij} is the moment magnitude of the ij^{th} subsource, and H_{ij} is a scaling factor introduced to conserve the high-frequency spectral level of subfaults as mentioned for the dynamic corner frequency.

The ground-motion acceleration from the entire fault can now be calculated in the time domain by Equation 3.14::

$$a(t) = \sum_{i=1}^{nl}\sum_{j=1}^{nw} A_{ij}(t + \Delta t_{ij}) \tag{3.14}$$

Δt_{ij} is the relative time delay for the radiated wave from the ij^{th} subfault to the observation point, while nl and nw are the number of subfaults along the length and width of main fault (Motazedian and Atkinson, 2005).

3.3 1D Site response analysis - DEEPSOIL

Local site conditions may have a significant effect on the ground motion propagation from an earthquake. In this thesis, the site response will be analyzed with the one-dimensional analysis program DEEPSOIL. DEEPSOIL has been developed under the direction of Prof. Youssef M.A. Hashash at the University of Illinois at Urbana-Champaign. The program allows to perform 1D site response analyses in the frequency domain by Equivalent linear approach (EQL) and in the time domain by a non-linear approach (NL) (Hashash et al., 2015).

1D site response analyses approximate ground motion by assuming that horizontal shear waves (SH-waves) propagate vertically from the bedrock through sediments to the ground surface. The sediments or soil profile is considered to be a linear viscoelastic (Kelvin-Voigt solid) system because the amplitude will attenuate with distance. The site stratigraphy is defined by horizontal layers that extend infinitely in the horizontal direction and must be perpendicular to the direction of wave propagation (Park and Hashash, 2004; Ordonez, 2012).

The EQL approach provides reasonable results for many cases, but the results are still an approximation of the actual non-linear response. Therefore, the NL approach can be used to analyze the actual non-linear response using direct numerical integration in the time domain. Both analyses can produce reasonable results for cases where strain levels are low, while for cases with high strain levels the NL-approach usually provide more accurate results (Kramer, 1996).

3.3.1 Soil behavior under cyclic loading and Soil properties

For geotechnical purposes, properties of sedimentary layers are usually specified by parameters such as density, viscosity, confining pressure, consolidation ratio, stiffness, shear strength, shear wave velocity, damping, Poisson's ratio, Young's modulus, and bulk modulus. For behavior of soils in soil response analysis, it can be assumed that these parameters can be reduced to stiffness and damping. Stiffness and damping can be used directly to describe the behavior of soils, these parameters are also known as the equivalent linear material parameters (Kramer, 1996; Ordonez, 2012).

Shear modulus

The shear modulus G, is defined as the stiffness of a material, and is continuously changing during cyclic loading. The relation between shear stress and shear strain can be expressed as a hysteresis curve/loop as shown in Figure 3.5, where the stiffness of the soil controls the inclination of the loop. The average value of the shear modulus under cyclic loading, G_{sec} can be approximated by Equation 3.15 (Kramer, 1996),

$$G_{sec} = \frac{\tau_c}{\gamma_c} \tag{3.15}$$

where τ_c is the shear stress amplitude and γ_c is the shear strain amplitude. G_{sec} varies as strain amplitude varies, and are influenced by e.g. void ratio according to Kramer (1996). By combining slopes of several hysteresis loops with various cyclic strain amplitudes, a *backbone curve* is obtained (Figure 3.5). G_{max} is the largest possible values of shear modulus, and is defined as the slope in the origin of the backbone curve. When the amplitudes of the cyclic strain increase, the modulus ratio G_{sec}/G_{max} drops to levels below 1, since G_{sec} reaches values lower than G_{max} for increasing strains. Because of this, we need to consider both G_{max} and how the modulus ratio G_{sec}/G_{max} changes when cyclic stains change, in order to correctly characterize a materials stiffness. G_{max} is related to the shear wave velocity and the density by the Equation 3.16 (Kramer, 1996).

$$G_{max} = \rho V_s^2 \tag{3.16}$$

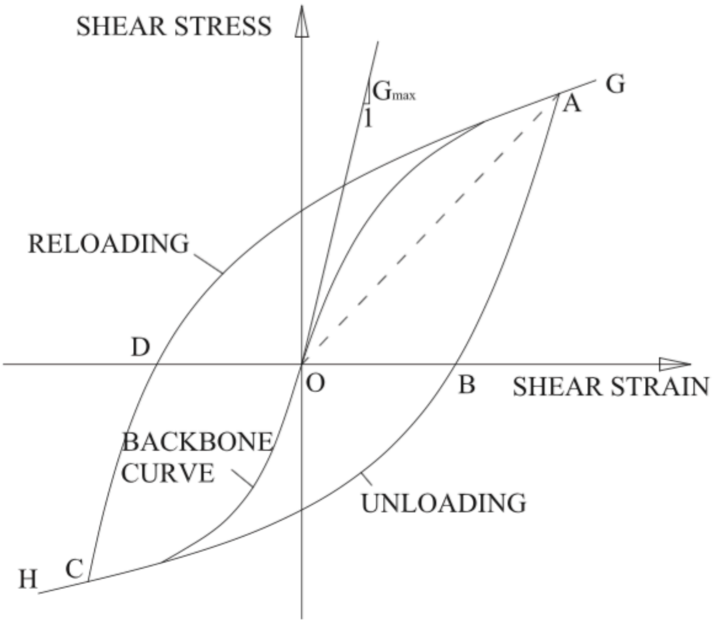

Figure 3.5: Illustration of stress-strain backbone curve and hysteresis loop. The slope at the origin are G_{max}, and the dashed line are G_{sec}. From: Yu et al. (2013)

Damping

The amplitude of real material will attenuate with distance, affected by the properties of materials the waves travel through and on the geometry of the wave propagation (geometry not considered in the 1D-analysis). As mention in the introduction of this section, the analysis assumes that the waves are traveling through a Kelvin-Voigt solid. In this section damping in general are described and the reader are refereed to e.g. Kramer (1996) for a detailed description of viscous damping.

Considering the hysteresis loop in Figure 3.5, the width, which is dependent on the area of this loop, is a measure of energy dissipation and can be described by the damping ratio:

$$\xi = \frac{1}{2\pi}\frac{A_{loop}}{G_{sec}\gamma_c^2} \tag{3.17}$$

The nonlinear behavior in soils due to cyclic loading can be approximated with the damping ratio and the shear modulus and are important in the equivalent linear approach. The width of the hysteresis loop increases as strain amplitude increase due to cyclic loading, which implies that the damping ratio also increase. The system dissipate energy even at very low strains. For the damping ratio described above, it is assumed that strain always will return to zero after cyclic loading, thus failure can never occur. When high strains are represented, this damping ratio will not capture the full nonlinearity of the soil (Kramer, 1996). For high strains, e.g. the GQ/H-model, described in section 3.3.3, can be implemented (Hashash et al., 2015).

3.3.2 Equivalent linear analysis

The equivalent linear approach was initiated by the work of Schnabel et al. (1972), and is a modification of the linear approach to predict non-linear behavior using an iterative procedure with EQL soil properties. The program SHAKE was developed for such analysis, and the EQL analysis in DEEPSOIL follows the procedure of SHAKE and Schnabel et al. (1972). The EQL approach principally uses a transfer function to evaluate if the frequency of the input motion is amplified or deamplified due to propagation through a material (Kramer, 1996).

The transfer function

The transfer function relates the displacement of the oscillator to the external load, and can also be seen as an output signal (displacement) produced by filtering an input signal (time history of loading). Properties such as thickness, stiffness, damping and input motion influence the characteristics of the transfer function (Kramer, 1996). The following explanation of the propagation of shear waves through the one-dimensional system is a summary from Kramer (1996), Ordonez (2012) and Lutro, Torunn (2011).

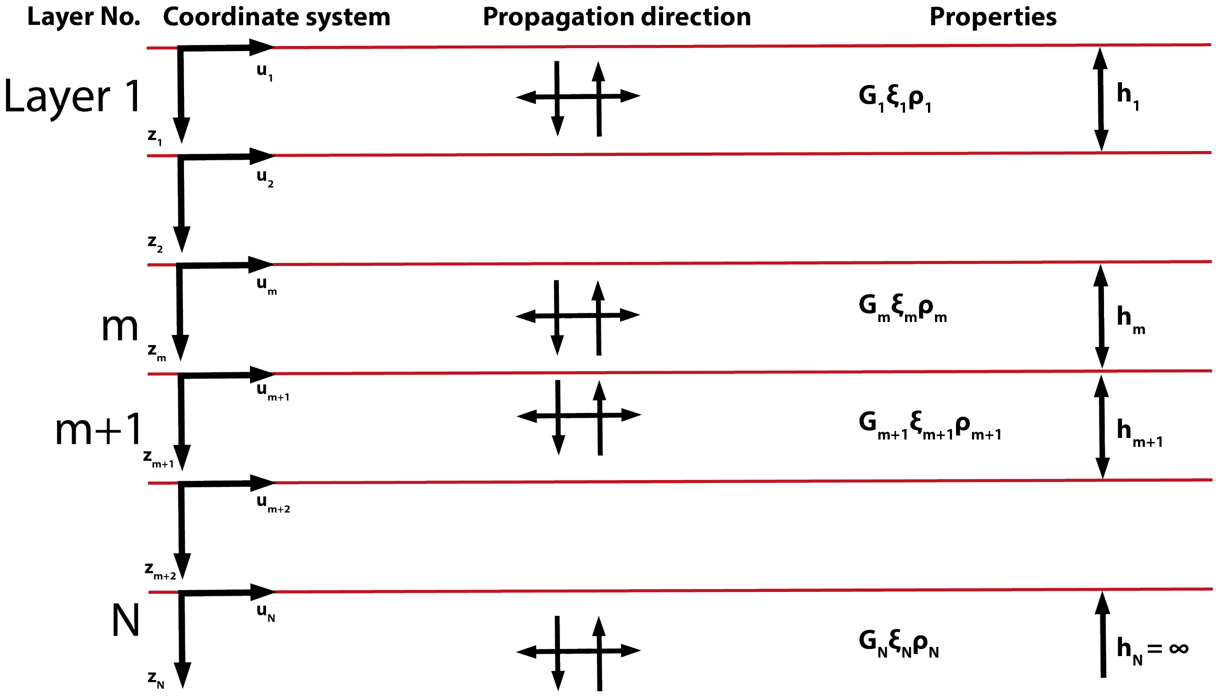

Figure 3.6: Illustration of a layered soil deposits overlying elastic bedrock. Each layer has different properties of shear modulus (G), damping factor (ξ) and mass density (ρ). The acceleration at each layer boundary can be approximated in DEEPSOIL. Modified from: Schnabel et al. (1972).

For a layered, damped soil in elastic bedrock, the transfer function is derived by considering a soil profile with N (Figure 3.6) layers that behaves like a Kelvin-Voigt solid (viscoelastic). The 1D shear wave propagating equation for a Kelvin-Voigt solid is expressed as

$$\rho\frac{\partial^2 u}{\partial t^2} = G\frac{\partial^2 u}{\partial z^2} + \eta\frac{\partial^3 u}{\partial z^2 \partial t} \tag{3.18}$$

where ρ is the mass density, G is the shear modulus, η is the viscosity of the soil and u is the horizontal displacement.

The solution of the wave equation (Equation 3.19) gives the horizontal displacement in terms of the circular frequency of ground shaking (ω), amplitudes (Ae and Be) of the waves traveling in the upward- ($-z$) and downward direction (z) and the complex wave number (k^*).

$$u(z,t) = Ae^{i(\omega t + k^* z)} + Be^{i(\omega t - k^* z)} \tag{3.19}$$

The product of the complex shear modulus and the shear strain gives the shear stress. Introducing a local coordinate system, Z, for each layer allows the displacement at the top and bottom for a particular layer, m, to be computed by Equations 3.20a and 3.20b.

$$u_m(Z_m = 0, t) = (A_m + B_m)e^{i\omega t} \tag{3.20a}$$

$$u_m(Z_m = h_m, t) = (A_m e^{ik^*_m h_m} + B_m e^{-ik^*_m h_m})e^{i\omega t} \tag{3.20b}$$

The displacement at the top of a particular layer must be equal to the displacements at the bottom of the overlying layer, and the stresses should also be continuous at layer boundaries. In addition, the shear stresses must be zero at the surface of the soil profile. Equation 3.21 relates the amplitudes in layer m to the amplitudes in layer 1:

$$A_m = a_m(\omega)A_1 \tag{3.21a}$$

$$B_m = b_m(\omega)A_1 \tag{3.21b}$$

where a_m and b_m are the amplitudes of the incident and reflected waves are equal at the free surface, i.e. $A_1 = B_1 = 1$. The transfer function relates the displacement amplitude at layer i to that at layer j can now be given by Equation 3.22.

$$F_{i,j}(\omega) = \frac{|u_i|}{|u_j|} = \frac{a_i(\omega) + b_i(\omega)}{a_j(\omega) + b_j(\omega)} \tag{3.22}$$

Implying that the motion in one layer can be determined from the motion in any other layer.

Ground motion evaluation

The previously described transfer function plays an important role in the linear evaluation of site response. The process is illustrated in Figure 3.7 and Kramer (1996) explains the site response evaluation as the following:

- The input motion (bedrock acceleration in time domain obtained from EXSIM12, Figure 3.7.b) are transformed to the frequency domain by the Fast Fourier Transform algorithm (FFT) and expressed as Fourier Amplitude Spectrum (FAS) (Figure 3.7.c).
- The properties of the soil layers are used to calculate the transfer functions (Figure 3.7.d).
- The Fourier series of the output (surface) motion is obtain by the taking the product of the FAS and the transfer functions (Figure 3.7.e).
- The surface motion is transformed back to the time domain by the inverse FFT algorithm (Figure 3.7.f).

Because this is a linear analysis, the nonlinearity of the soil must accounted for. In a linear approach, the properties G and ξ are constant for each layer, but will in reality depend on the induced strain in each layer. To make sure that the properties used in the analysis are compatible with the computed strain levels in all layers, an iterative procedure is needed to obtain equivalent linear properties values (Kramer, 1996). The iterative procedure is illustrated in Figure 3.8 and described by Kramer (1996) and Ordonez (2012) as follows:

1. Initial estimates of the shear modulus, G, and the damping, ξ, are made for each layer in the soil profile. For the initial estimate, low strain levels are often used.
2. The ground motion and the time histories of shear strain for each layer is computed based on the estimates in Step 1.
3. From the maximum shear strain in the shear strain time history, the effective shear strain is computed for layer j by the equation

$$\gamma_{eff_j}^{(i)} = R_\gamma \gamma_{max_j}^{(i)}$$

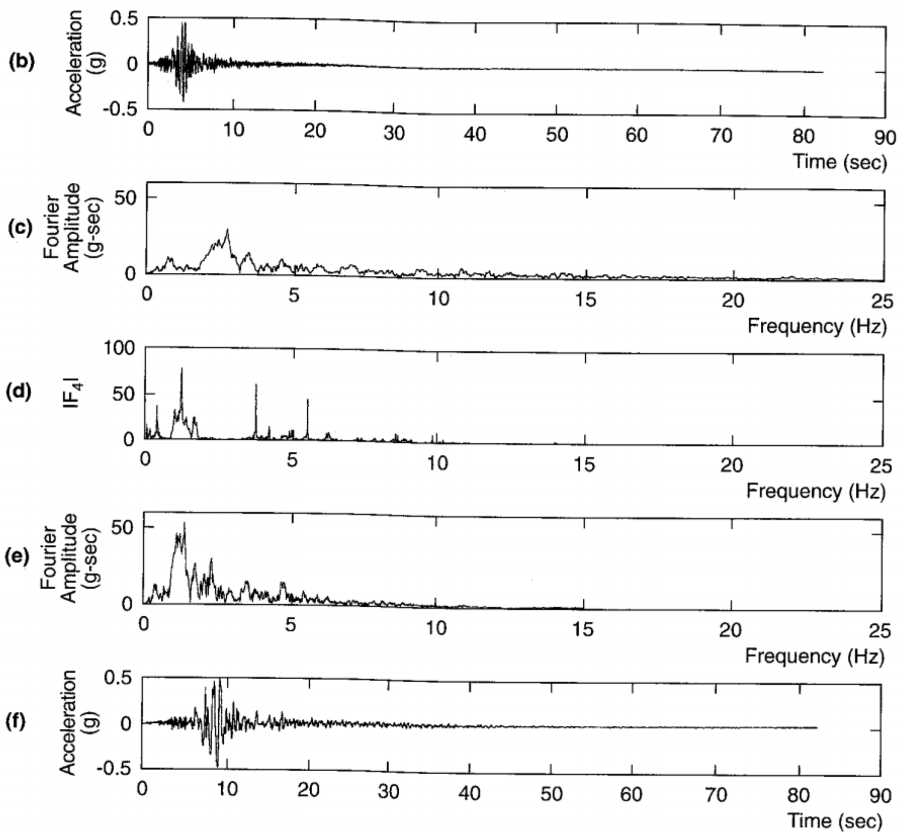

Figure 3.7: Ground motion modeling process in DEEPSOIL. b) Input acceleration to base of sediment profile. c) Fast Fourier Transform (FFT) of input motion. d) Transfer function obtained from soil properties. e) Output ground motion in Fourier series. f) Output ground motion in time domain by inverse FFT. From Kramer (1996)

where the subscript i refers to the iteration number and the ratio of the effective shear strain to maximum shear strain, R_γ depends on the earthquake magnitude and can be estimated by

$$R_\gamma = \frac{M-1}{10}$$

4. New equivalent linear values of G and C are chosen from the effective strain in Step 3 and used for the next iteration.

5. The iteration process ends when the difference between the computed shear modulus and damping values reach a predetermined value in all layers.

3.3.3 Non-Linear analysis

An alternative approach to the EQL analysis, is to analyze the actual nonlinear response of a soil profile using direct numerical integration in the time domain, the NL approach.

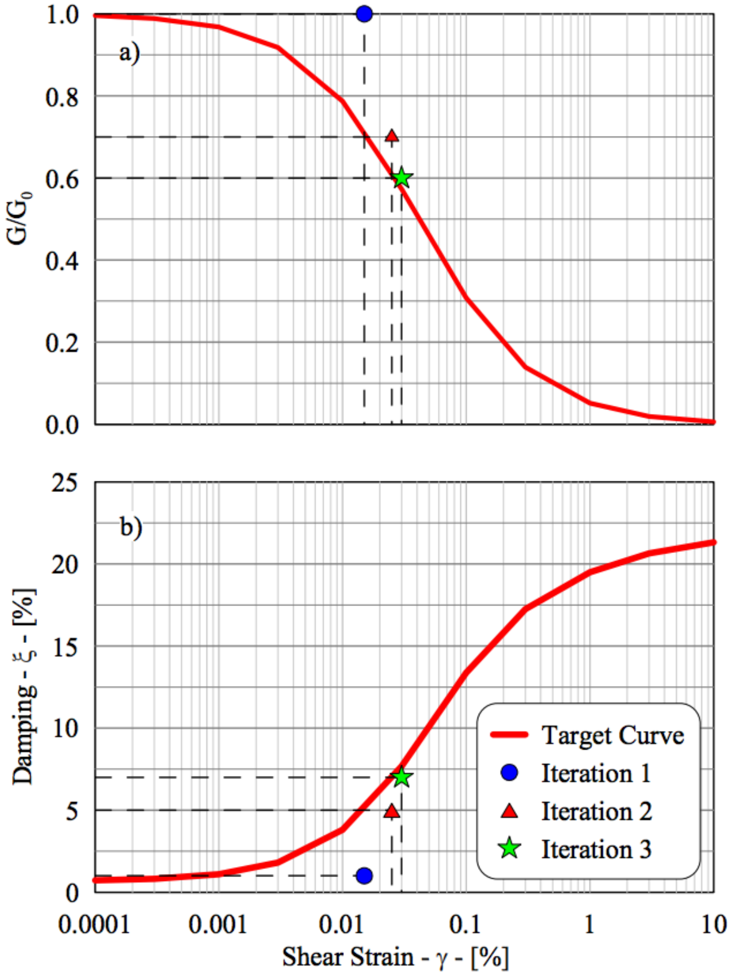

Figure 3.8: Illustration of the equivalent linear iterative procedure to account for nonlinear behavior of soils; a) Modulus reduction curve b) Damping curve. From Hashash et al. (2010)

In DEEPSOIL, the lumped mass equation of motion (Equation 3.23) is solved in a time-step procedure called the Newmark β method (Hashash et al., 2015).

$$[M]\{\ddot{u}\} + [C]\{\dot{u}\} + [K]\{u\} = -[M]\{I\}\ddot{u}_g \tag{3.23}$$

In Equation 3.23, $[M]$ is the soil mass matrix and is usually constructed as a lumped mass system (Figure 3.9). $[C]$ is the viscous damping matrix, $[K]$ is the stiffness matrix, described below. $\ddot{u}$, $\dot{u}$ and u are the acceleration, velocity and displacement, respectively. $\ddot{u}_g$ is the acceleration of the input motion at the base of the soil profile (Park and Hashash, 2004; Hashash et al., 2010).

The stiffness matrix, $[K]$, is continuously updated during earthquake loading, which is one on the key element in the non-linear approach. A constitutive model that described the cyclic behavior of soils can be used to obtain the soil response (Hashash et al., 2010).

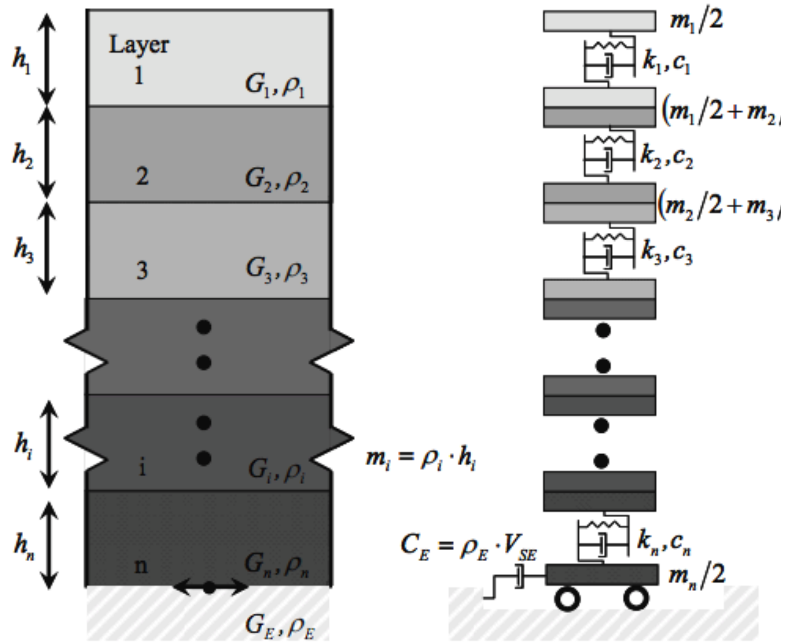

Figure 3.9: Multi-degree-of-freedom lumped parameter model. The soil mass matrix (m) is obtained from the vertical thickness (h) and the density (ρ). G, k and c represent the shear modulus, viscous damping matrix and the stiffness matrix, respectively. V_{SE} is the velocity from a horizontal propagating shear wave at the base of the sediment profile. From: Hashash et al. (2010)

One of the non-linear soil model implemented in DEEPSOIL, and the one used for this study, are the GQ/H model (Hashash et al., 2015). This model allows the shear strength of soil at failure to be defined, while still providing the ability to represent the small-strain stiffness nonlinearity. The equation to construct the backbone curve has the form:

$$\frac{\tau}{\tau_{max}} = \frac{2(\gamma/\gamma_r)}{1 + (\gamma/\gamma_r) + \sqrt{(1 + (\gamma/\gamma_r))^2 - 4\theta_\tau(\gamma/\gamma_r)}} \tag{3.24}$$

where τ is the shear stress and τ_{max} is the peak shear strength of the soil the soil at failure, θ_τ is a curve fitting parameter, γ is the shear strain, and γ_r is the reference shear strain given by $\gamma_r = \tau_{max}/G_{max}$. The GQ/H model is compared to the reference curve for modulus reduction and damping curves from Darendeli (2001) equations to represent the dynamic soil behavior (Groholski et al., 2015).

The definition of a damping matrix is necessary to prevent oscillations and to accommodate the small strain damping to the system that is not captured by the NL models. In DEEPSOIL, the construction of the viscous damping matrix $[C]$ can be performed using either Rayleigh damping or frequency independent formulation (Phillips and Hashash, 2009). The construction in this thesis applied the recommended (Hashash et al., 2015) frequency independent approach. Information of the frequency independent algorithm implemented in DEEPSOIL can be found in Phillips and Hashash (2009).

The integration process can be summarized based on Kramer (1996) and Hashash et al. (2015) as the following:

1. The particle velocity $\dot{u}_{i+1}$ and the total displacement u_{i+1} at time $i+1$ are known at each layer boundary by the equations (Newmark β method):

$$\dot{u}_{i+1} = \dot{u}_i + [(1-\gamma)\Delta t]\,\ddot{u}_i + (\gamma\Delta t)\ddot{u}_{i1+1}$$

$$u_{i+1} = u_i + (\Delta t)\dot{u}_i + \left[(0.5-\beta)(\Delta t)^2\right]\ddot{u}_i + \left[\beta(\Delta t)^2\right]\ddot{u}_i + 1$$

2. The shear strain within each layer $\gamma_{i,t}$ are determined from the particle displacement profile.
3. The stress-strain relationship, in this case the GQ/H-model, is used to determine the shear stress $\tau_{i,t}$ in each layer.
4. The motion at the base of the soil layer at time $t+\Delta t$ is determined from the input motion.
5. The motion of each layer boundary at time $t+\Delta t$ is calculated, stating with the deepest layer.
6. The response in the next time step is computed by repeating all the steps from Step 1 with updated matrices of $[K]$ and $[C]$.

3.4 Seismic slope stability

There exist several analyses for evaluating the seismic stability of a slope or even a area, on several levels of details (Brian Carlton, pers. comm.):

- Pseudo-Static analysis, which is a limit equilibrium solution that calculates the Factor of Safety
- Seismically induced permanent displacements
- 2D or 3D finite element analyses or finite difference analyses

Two seismic stability analyses have been applied in order to evaluate the slope stability of the study area. The pseudo-static analysis is the simplest and least accurate analysis. This analysis has been performed to obtain a general idea of the stability in the study area. The second analysis, is the permanent displacement analysis. This analysis predict the displacement as a result of ground motion from an earthquake, which is a better indication of seismic slope stability (Kramer, 1996).

3.4.1 Limit equilibrium analyses

The pseudo-static analysis is based on the limit equilibrium method. The limit equilibrium method provides a scalar index of the stability, commonly known as the Factor of Safety (FoS). Slope failure often occur due to processes that increases the shear stresses or decrease the shear strength of the soil (Abramson et al., 1996). When the shear stresses required to maintain equilibrium reach or exceed the available shearing resistance on a potential failure surface, the slope will become unstable.

The concept of limit equilibrium is the base for nearly all slope stability analyses, and can generally be explained by Equation 3.25, or physically by Equation 3.26 (e.g. Kramer, 1996; Abramson et al., 1996; ten Brink et al., 2009).

$$\mathrm{FoS} = \frac{\text{available shear strength}}{\text{shear stress required to maintain equilibrium}} \tag{3.25}$$

The driving forces in a static slope stability analysis are the weight of the soil mass, i.e. gravitational forces, and the resisting forces are the shear strength of the soil (Abramson et al., 1996).

$$FoS = \frac{S_u}{\tau} \tag{3.26}$$

S_u is the shear strength of the material in place (in this study; the undrained shear strength of the sediment), and τ is the shear stress on a slip surface (Kramer, 1996; Abramson et al., 1996; ten Brink et al., 2009). The shear strength of the soil is dependent on the effective stress and the pore water pressure, which is briefly described in section 1.4. The values for the soil properties parameters can be found by laboratory testing and field investigation (Abramson et al., 1996). In this thesis, all parameter values are found in previously studies and the various laboratory tests and field investigation methods will therefore not be further discussed.

Equation 3.26 with $FoS > 1.0$ indicates a stable slope, where a $FoS \leq 1.0$ indicates that the slope may fail. In practice, an FoS above 1.0 is rarely considered acceptable, due to uncertainties in the parameters used to define FoS (Kramer, 1996).

3.4.2 Pseudo-static analysis

Additional dynamic stresses needed to produce instability may be low if the shear stresses required to maintain equilibrium under static gravitational loads are high. The effects of earthquakes can cause such additional dynamic stresses in a slope. One way of analyzing these effects from an earthquake on slope stability is the pseudo-static approach. This approach is similar to the static (limit) equilibrium approach, described above (Kramer, 1996).

This section is similar to section 3.1, where the maximum distance from source to site was calculated in terms of critical acceleration (FoS = 1) and the slope angle. This Section will describe the calculation of FoS in terms of the horizontal earthquake acceleration and slope angle.

The shear strength τ in Equation 3.26 can be defined , as in section 3.1:

$$\tau = \gamma' z \sin\beta \cos\beta + k\gamma z \cos^2\beta \tag{3.27}$$

where k are the horizontal earthquake acceleration (ten Brink et al., 2009). This horizontal acceleration are of interest here, because the soil response is highly dependent on this parameter. The FoS can then be calculated with Equation 3.26 with the shear stress, τ, defined above.

3.4.3 Seismically-Induced permanent displacements

No information on deformation, or earthquake-induced displacement, are obtained with the pseudo-static analysis. Because the stability of the slope is controlled by seismically-induced deformation, displacement analyses will give a reasonable indication of seismic stability of slopes (Kramer, 1996). When acceleration exceeds the critical acceleration, the Factor of Safety will be below 1 and the potential failure mass will be unbalanced. This condition may initiate a failure of the slope, and a prediction of the displacement can be performed by displacement analyses (Kramer, 1996; Rathje and Saygili, 2009).

Seismic displacement analyses requires three main components, which also represent the most significant uncertainties. The input motion to the soil profile, or the resulting ground motion from an earthquake, is the most critical component because of the contribution to displacement calculation. The dynamic resistance of the structure and the dynamic response of the potential sliding mass (failure mass) are the two other components (Bray, 2007; Rathje and Saygili, 2009).

Typical ground motion parameters that are used in displacement analyses are peak ground acceleration (PGA), peak ground velocity (PGV), spectral acceleration (SA / PSA), critical acceleration and critical acceleration ratio, earthquake magnitude, Arias intensity and combinations of these (Bray, 2007). Ground motion with the same PGA can vary in respect to e.g. duration, and it is therefore a very simple calculation/prediction with the use of only this parameter. Ideally, the prediction should be performed with two or more of the parameters mentioned above to obtain a better estimate of the effect on slope stability (Bray, 2007). Travasarou and Bray (2003) found the spectral acceleration at a degraded period equal to 1.5 times the initial fundamental period of the slope to be the most efficient ground motion parameter for all slopes. The important ground motion characteristics of intensity and frequency component can be directly captured by the spectral acceleration and are in addition relatively easy to obtain (Bray, 2007). The magnitude of an event also have large influence on displacement calculation because the frequency content and duration of shaking is magnitude dependent (Rathje and Saygili, 2009).

The critical acceleration (or the yield coefficient), as described in sections above, can be used as an indication of the dynamic resistance of a earth structure. One of the most critical elements of a seismic displacement calculation is estimating k_y because it is highly dependent on the dynamical strength of the soil, and because it has an important effect on seismic displacement (Bray, 2007; Rathje and Saygili, 2009).

The Newmark sliding block analysis estimates the seismically-induced permanent displacement by considering the part of the acceleration time-history that exceeds the critical acceleration and integrates twice with respect to time (Jibson, 2007). This method can be used to get an overview where the dominant displacement mechanism is seismic compression of the volume of the soil. However, this method considers a rigid block sliding on a surface and does not take into account the dynamic response of a potential failure mass under an earthquake. The dynamic response characteristics of the potential sliding mass also affects the seismic displacement. When the sliding mass is near resonance the seismic displacement increases (e.g. Rathje and Bray, 2000). For methods of seismic displacement that considers the seismic response of a deformable sliding block, the fundamental period period of the sliding mass T_s can usually be estimated with the equation $T_s = 4H/V_s$ (Bray, 2007).

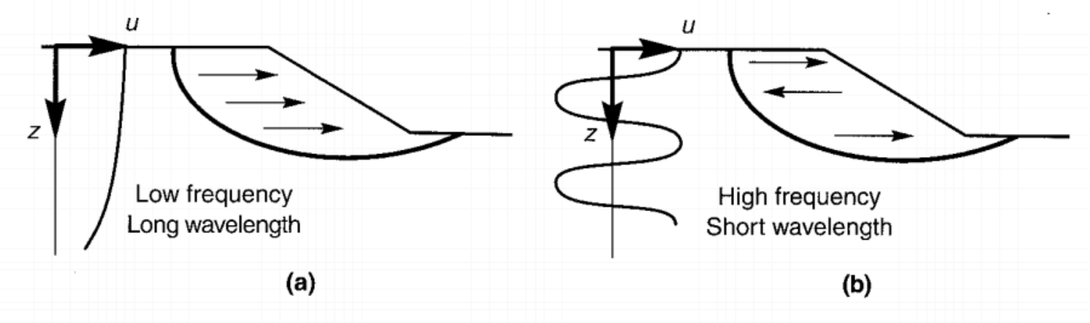

Figure 3.10: Influence of frequency on motions induced in slopes. a) low-frequency motion causes soils above failure surface to move nearly in phase. b) high-frequency motion above failure surface may be moving in opposite directions. From: Kramer (1996)

As mentioned earlier, the input motion is the most critical factor for the accuracy of a seismic displacement analysis. The dynamic response of a soil depends on stiffness, amplitude and frequency content of the input motion. For slopes that are subjected to low-frequency motion, the lateral displacement throughout the potential failure mass will nearly be in phase, see Figure 3.10. Because results (described in section 5.3.3, has shown an amplification in the soil for lower frequencies, we want to take this into account. Therefore, the model proposed by Travasarou and Bray (2003) has been used for the seismic displacement analysis. The model by Travasarou and Bray (2003) is a simplified semi-empirical predictive model for estimating seismic slope displacement is expresses as:

$$\begin{aligned}\ln(D) = & -1.10 - 2.83\ln(k_y) - 0.333(\ln(k_y))^2 \\ & + 0.566\ln(k_y)\ln(S_a(1.5T_s)) + 3.04\ln(S_a(1.5T_s)) \\ & - 0.244(\ln(S_a(1.5T_s)))^2 + 1.5T_s + 0.278(M-7) \pm \epsilon\end{aligned} \tag{3.28}$$

More on the Fundamental Period

The lowest natural frequencies of a soil deposit are known as the fundamental frequency, and tells us where the greatest amplification factor will occur. The period corresponding to the fundamental frequency are known as the fundamental period or the characteristic site period. The period that will give the most significant amplification can be estimated by calculating the fundamental period (Kramer, 1996). Continued loading can result in an increase of the fundamental period in soft soil. This is referred to as the degraded fundamental period (Biscontin and Pestana, 2003). Travasarou and Bray (2003) (Eq. 3.28) concluded that the degraded fundamental period would be a better choice in the calculation for seismic-induced permanent displacement than the initial fundamental period because of the non-linearity of the soil.

Chapter 4

Data

This chapter will describe and discuss the input data used in the different methods applied in this study. The parameters have mostly been adapted from previous publications. The Chapter will start by describing the input parameter for the calculation of maximum distance from fault to site of failure. The input parameters implemented in the ground motion modeling in EXSIM12 and site response analysis in DEEPSOIL will be described. Last, the input parameters to the slope stability analyses will be summarized.

4.1 Maximum distance from fault to site

It is expected that a higher magnitude will have a greater potential of triggering failure, and that there might exist a minimum magnitude where failure would rarely occur as a result of earthquake shaking. Equally, the source-to-site distance where failure could occur is expected to increase with increasing magnitude of the earthquake. The maximum source-to-site distance also depend on the type of landslide occurring, i.e. type of material and movement (Kramer, 1996). Keefer (1984) stated that for an earthquake to trigger a submarine failure, the magnitude of the event should be equal to or above 5. The maximum magnitude in Norway is assumed to be of magnitude 7 (Bungum et al., 2005), therefore the magnitudes between 5 and 7 have been modeled. Because the slope angle of which earthquakes can trigger submarine slide are of interest, the calculation have been performed with angles from 0 to mainly 10°, and for some calculations up to 14-15 °.

Morphometrical parameters of the Storegga Slide have been mapped by Haflidason et al. (2005), and the vertical thickness, z, of the slide have been adapted from the average height of the headwall from their mapping. The average height of headwalls is assumed to represent the initial thickness of the sediments before the failure, and was preliminary set to 200m. This vertical thickness is a very rough estimate, as the slide had a retrogressive movement and cut through several layers (Bryn et al., 2005).

The failure mass has by e.g. Haflidason et al. (2005) been identified to be of tertiary age. Lindholm et al. (2005) and Gauer et al. (2005) used a density of $2g/cm^3$ for sediments of tertiary age in their studies of seismic hazard and retrogressive slide dynamics. This value has been adopted for this study. The density for water is commonly set as $1g/cm^3$, even though it might be higher for salt water this value has been used here. The corresponding unit weight is $19.62kN/^3$ and the submerged unit weight is approximate $10kN/m^3$. The weight ratio (γ'/γ) have been computed as in ten Brink et al. (2009) by the equation $(\rho_{soil} - \rho_{water})/\rho_{soil}$.

Lindholm et al. (2005) used a shear wave velocity of $1.1.km/sec$ for tertiary sediments and have been used here as an average velocity for the failure mass.

The undrained shear strength (S_u) have partly been adapted from Kvalstad et al. (2005b) and Leynaud et al. (2004). Kvalstad et al. (2005b) studied the soil condition and slope stability in the Ormen Lange area from a cone penetration test at the top of the upper headwall. The undrained shear strength, Su, at 200m depth (average thickness of sediments) have been chosen from a cone penetration test above the slide scar described by Kvalstad et al. (2005b).

Leynaud et al. (2004) performed a slope stability assessment of the Hellan-Hansen area located at the side of the Storegga Slide scar (Figure 4.4) and give a summary of soil conditions and recommended soil parameters for this area. The Hellan-Hansen area are located to the side, and may be a better analogue to the soil conditions at the release area of the Storegga slide than the geotechnical parameters obtained at the top of the slide scar. Because the vertical thickness of the slide have been assumed to be 200m, the undrained shear strength to use have been adapted from this depth. The S_u for both studies are close, and an average of 425kPa have been used.

The c/p - ratio is a measure of dynamic soil properties at high strain levels, and is the ratio between the undrained shear strength and the effective consolidation pressure (Abramson et al., 1996). The ratio have been calculated from the undrained shear strength, the submerged unit weight and the vertical thickness of the failure mass, equation given in Table 4.1.

The fundamental period was calculated by the equation $T = 4z/V_s$, which is a reasonable estimate for a potential sliding mass where the response is mainly 1D, shown in Figure 4.1. (Rathje and Bray, 2001).

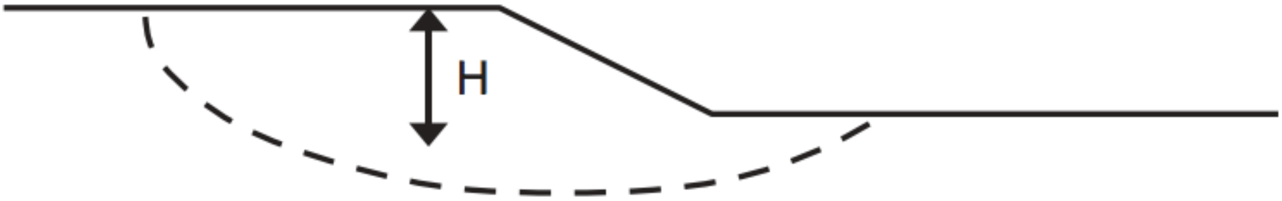

Figure 4.1: Assumed geometry of potential sliding mass for estimating the fundamental period. *H* represent the vertical thickness of the potential failure mass. Modified from: Bray (2007)

The c-values used in the GMPEs was chosen based on the fundamental period. The period was approximated to 0.75s for this calculation. The c-values for different periods can be found in Campbell (2003) and Shahjouei and Pezeshk (2015). A summary of the parameters used can be found in Table 4.1.

Table 4.1: Input parameters used in the calculation for maximum fault to site distance.

Parameter	Notation	Value
Vertical thickness of slide	z	$\approx 200m$
Density of soil mass	ρ_{soil}	$2g/cm^3$
Density of water	ρ_{water}	$1g/cm^3$
Shear wave velocity	V_s	$1.1km/sec$
Submerged unit weight	γ'	$9.62kN/m^3$
Saturated unit weight	$\gamma = \rho g$	$19.62kN/m^3$
Weight ratio	$\frac{\gamma'}{\gamma}$	≈ 0.5
Undrained shear strength	S_u	$\approx 425kPa$
c/p - ratio	$\frac{S_u}{\gamma' z}$	0.2209
Fundamental period	$T_s = \frac{4z}{V_s}$	≈ 0.75

4.2 Selection of Faults

One of the question that we want to investigate are at what distance from the release area the earthquake can be located, the chosen faults are therefore at various distances (Table 4.2). Blystad et al. (1995) mapped the structural elements in the Norwegian Sea region (Figure 2.3). Many of the structural elements from Blystad et al. (1995) have been used

Table 4.2: Some information of the faults selected for ground motion modeling. The modeling has been performed with magnitude and fault type given in this table.

Fault	Abbreviation	Distance from initiation area	Fault type	Magnitude (M_w)
Fles Fault Complex	FFC	≈ 130-170km	Reverse	5-7
Faroe Shetland Escarpment	FSE	≈ 45km	Reverse	5-7
Gnausen High - Giske High-Gossa High	GGG	≈ 190km	Reverse	6-7
Jan Mayen Fracture Zone North	JMFZN	≈ 215km	Strike-Slip	6-7
Jan Mayen Fracture Zone South	JMFZS	≈ 80km	Strike-Slip	5-7
Klakk Fault Complex	KFC	≈ 150-180km	Reverse	5-7
Modgunn Arch - Gjallar Ridge	MG	≈ 85km	Strike-Slip	5-7
Møre Marginal High	MMH	≈ 120km	Strike-Slip	5.5-7
Manet Ridge - Ona High	MO	≈ 155-165km	Reverse	5.5-7
Makrell Horst - Tampen Spur - Gnausen High	MTG	≈ 210-230km	Reverse	6-7
Ormen Lange	OL	≈ 130km	Reverse	5-7
Slettringen Ridge North	SRN	≈ 45km	Reverse	5-7
Slettringen Ridge South	SRS	≈ 66-80km	Reverse	5-7
Vigra High - Grip High	VG	≈ 80-90km	Reverse	5-7

for detailed seismic hazard studies by several, e.g. Lindholm et al. (2005); Atakan and Ojeda (2005), and have also been adopted for this study. In addition six other faults have also been selected for further modeling. The number of faults in the area is of a great number and therefore the main focus have been on the larger faults, that is assumed to be capable of generating earthquakes with magnitudes larger than 5. Some of the faults selected for the modeling are located outside the maximum distance zones, but have been included due to the focus in previous published studies, e.g. Lindholm et al. (2005) and Atakan and Ojeda (2005).

Lindholm et al. (2005) modeled seven main faults in terms of deterministic and probabilistic seismic hazard assessment. The basis for hazard analyses are the earthquake catalog, where it is assumed that future earthquakes could occur close to locations of historical earthquakes. The faults have dimensions that imply that they have a great earthquake potential, but there exist no clear evidence that these specific fault have been active through the post-glacial period. However, there are earthquakes that have been recorded close to these fault (compare Figure 4.2 and 4.3), and they are therefore identified as sources for potential earthquakes (Lindholm et al., 2005). An overview of the faults selected for modeling can be found in Table 4.2 and Figure 4.3.

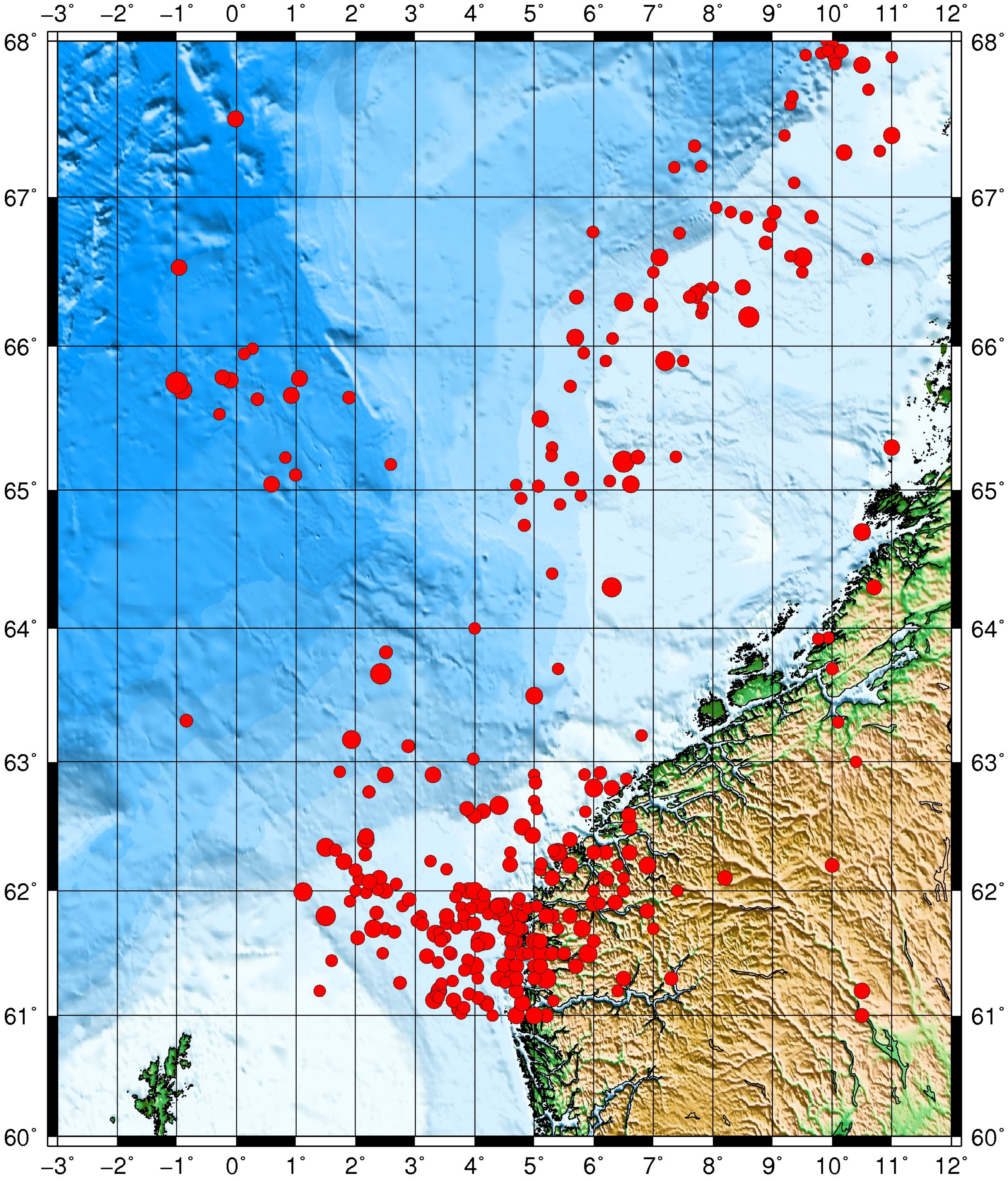

Figure 4.2: Earthquakes registered in study area from 1900 to November 2017 (NNSN earthquake catalog).

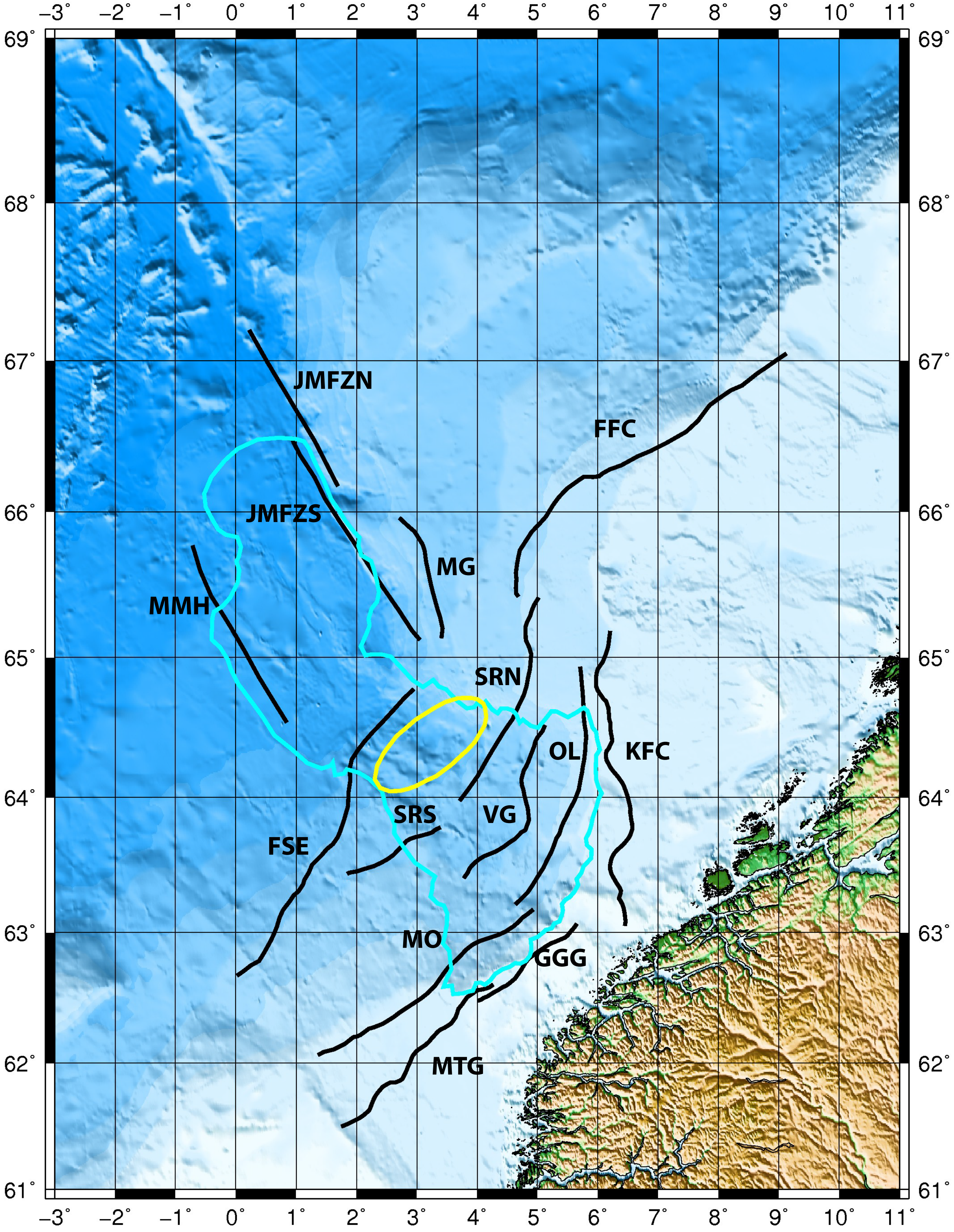

Figure 4.3: Map displaying selected fault, the abbreviation are specified in Table 4.2. Blue outline represent the Storegga slide, yellow ellipse represent the assumed initiation area of the slide. Redrawn from: Blystad et al. (1995), Lindholm et al. (2005), Bryn et al. (2005) and Haflidason et al. (2005).

4.3 Input to EXSIM12

Based on parameters describing the fault and local crust properties the ground motion can be calculated with EXSIM12. Parameters such as stress, drop, S-wave velocity, magnitude and quality factor are implemented. The selected faults are located in the same area, and the same parameters have been used for all faults, except location, magnitude and depths. Tveit (2013) performed a sensitivity study for the Øygarden fault, and because this fault and the faults in my study area are all located offshore Norway, it is assumed that the earthquakes in this study will have the same properties as the Øygarden fault and have been adopted.

Some of the important parameters in EXSIM12 are the density and S-wave velocity of the crust, geometrical spreading, attenuation function and quality factor. Boore (2009) proposed values for Eastern-North America (ENA). Because of the similar tectonic environment for ENA and Norway, Tveit (2013) suggested that these values are appropriate to adapt (Table 4.5).

Tveit (2013) concluded that the ground motion are most affected by the stress drop ($\Delta\sigma$), κ [1], moment magnitude and the depth. For κ and $\Delta\sigma$, Tveit (2013) found that a value of respectively 0.02 and 80 bar are appropriate for Norway.

It is not likely that the entire length of the fault will rupture all at once. Because of this, Wells and Coppersmith (1994) relations have been used to calculate the rupture length and area for a given magnitude. The equation for subsurface rupture length have been used, because Wells and Coppersmith (1994) states that this equation is appropriate for buried or blind faults, which are the case for the selected faults in this study. The equations can be found in Table 4.3 and calculated lengths, area and width can be found in Table 4.4. It is reasonable to expect that the part of the fault located closest to the area of release will have the greatest potential to affect the slope stability, and is therefore used in the modeling in order to observe the worst-case scenario (Kramer, 1996).

There is little information on focal depth of earthquakes in the study area (Lindholm et al., 2005), and therefore high uncertainties related to the fault depth. Interpretation of seismic profiles and depth conversions in order to find the exact depth of the faults will be too extensive for this master thesis. Another possibility would have been to study the hypocenter depths of recorded earthquakes in this area, to get an indication of the depths of the faults. The depth of the fault have a major impact on the ground motion, where deeper faults produce a lower ground motion level than a shallow faults at the surface

---

[1] κ - near surface attenuation

Table 4.3: Equations from Wells and Coppersmith (1994) used to calculate length and width of faults depending on magnitude.

Type	Equation	Slip type	a	b
Surface Rupture Length	$\log(SRL) = a + bM$	Reverse	-2.86	0.63
		Strike-slip	-3.55	0.74
Subsurface Rupture Length	$\log(RLD) = a + bM$	Reverse	-2.42	0.58
		Strike-slip	-2.57	0.62
Rupture Area	$\log(RA) = a + bM$	Reverse	-3.99	0.98
		Strike-slip	-3.42	0.90
Rupture Width	RW = RA/RLD	Reverse	–	–
		Strike-slip	–	–

Table 4.4: Calculated length and width (in km) of faults depending on magnitude.

	Slip type	M7	M6.5	M6	M5.5	M5
RLD	Reverse	43.6516	22.3872	11.4815	5.8884	3.0200
(km)	Strike-slip	58.8844	28.8403	14.1254	6.9183	3.3884
RA	Reverse	714.3102	239.8833	77.6247	25.1189	8.1283
(km^2)	Strike-slip	758.5776	269.1535	95.4993	33.8844	12.0226
RW	Reverse	16.9824	10.7152	6.7608	4.2658	2.6915
(km)	Strike-slip	12.8825	9.3325	6.7608	4.8978	3.5481

(Tveit, 2013). Modeling at different depth will therefore give an indication of the depth the fault should be located if being responsible for triggering slope failure. Due to these uncertainties, the modeling has been performed with depths of 1,5 and 10 km depth to the top of these faults.

It is not possible to determine the hypocenter location 8200 years ago, when the Storegga Slide occurred. The locations of the hypocenter was therefore set to random, with 10 iterations. This creates an average, or a smoothing of the ground motion by changing the locations of the hypocenter 10 times, and eliminate the effect of directivity. The same applies for the slip distribution, because this is a theoretical study, and the slip distribution is unknown and set to random.

Based on the strike compared to the stress field, the type of fault was chosen. The orientation of the stress field favors that many of the fault will have an oblique mechanism, but because EXSIM12 does not allow for a oblique definition the fault type was set to strike-slip and reverse. Tveit (2013) concluded that the fault type have a minor impact on the ground motion, but there are a small tendency that strike-slip have a higher ground motion level than reverse. The dip of the faults was also found by Tveit (2013) to have a minor impact on the ground motion, but was set to 90 ° for the strike-slip and

60 ° for the reverse faults (Kuvvet Atakan, pers. comm.).

The sensitivity study by Tveit (2013) found that ground motion is sensitive to subfault dimensions. The peak ground acceleration will increase near the fault if the subfault length is too small, and decrease near the fault if the subfault width is too small. The subfault dimensions have therefore been varied depending on the length ruptured in an earthquake. The pulsing percent define how many subfault are active at a time and are set to 50 % based on the sensitivity study by Tveit (2013).

Additional parameters in Table 4.5, have been adapted from the example input file from EXSIM12. EXSIM12 allow to implement crustal amplification file, empirical filter and site amplification file. The crustal amplification file from EXSIM12 have been used because it is given for hard rock site as Norway (Johnsen, 2015). In this study, there is no need to apply an instrument response function, and the empirical filter file is not needed. Additional site response will be evaluated by DEEPSOIL, where the input parameters are described in the next section.

4.3.1 Output from EXSIM12

EXSIM12 provides several files with various parameters, where three of the files are of interest for further modeling. One file contains the acceleration-time history, another contains a summary of PGA at each coordinate pair defined, and the last of provides the spectral accelerations. EXSIM12 was also run at only the coordinate pair of the approximately initiation are of the slide. These results will provide the information given for only the site of interest, which was used as input motion to DEEPSOIL.

Table 4.5: Input parameters to the modeling in EXSIM12

Parameter	Value
Moment magnitude M_w	5 - 7
Stress drop $\Delta\sigma$	80 bar
Coordinates of upper fault edge	Fault location
Fault dimensions	Table 4.4
Depth of fault	1, 5 and 10km
Fault Dip	Reverse 60° Strike-slip 90°
Subfault dimensions	$5x5km$ $2.5x2.5km$
Rupture velocity/S-wave velocity	0.8
Hypocenter location	Random
Rise time	1
Density of crust	$2.8g/m^3$
S-wave velocity	$3.7km/sec$
Geometric spreading	dR, d = 3 0.16 (10-70km) -0.03 (70-130km) 0.04 (>130km) 0.05
Quality factor	$Q = max\left[1000, 893f^{0.32}\right]$
Distance depending on duration	dR, d = 3 0.16 (10-70km) -0.03 (70-130km) 0.04 (>130km) 0.05
Type of Window	1 (Saragoni-Hart window)
Low-cut filter corner	0.05 (removes frequencies lower than 0.05 Hz)
Output ground motion frequencies	PGA, PGV, 0.5, 5.0
Pulsing percent	50
Iteration per site	10
Slip distribution	Random slip

4.4 Input to DEEPSOIL

The Hellan-Hansen area is situated north of the Storegga Slide scar, and the sediment is this area are not significantly affected by the slide. Because we want to obtain geotechnical parameters that can represent the conditions in the slope before the failure occurred, the Hellan-Hansen area are of interest. Leynaud et al. (2004) performed slope stability assessment of the Hellan-Hansen area, and borehole 6405/5 (Figure 4.4) described in Leynaud et al. (2004) has been assumed to be a candidate for the geotechnical parameters. Boreholes located at the top of the slide headwall was also evaluated to be representative. However, downslope differences in geotechnical properties may occur (Haflidi Haflidason, pers. comm.) and it was therefore decided to used the parameters from Hellan-Hansen. The location of this borehole are also approximately at the same downslope distance as the initiation area of the slide.

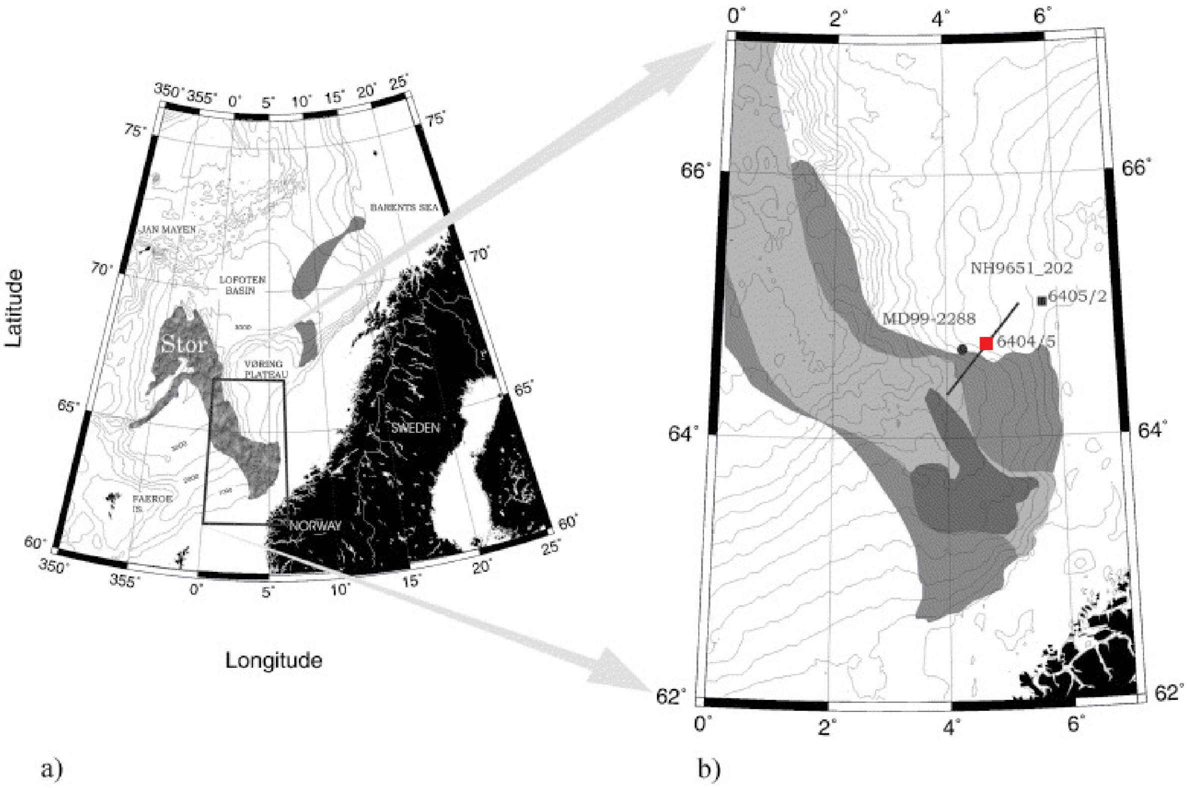

Figure 4.4: Location of borehole 6405/5 (red dot). The geotechnical parameters from this borehole have been used for the soil response evaluation. a) Regional overview of study area b) Location of borehole. From: Leynaud et al. (2004)

4.4.1 Procedure in DEEPSOIL

The soil response in DEEPSOIL involve five steps before the result can be obtained, the following are a summary from Hashash et al. (2015).

Step 1 - Define analysis

In step 1, both time domain analysis and frequency domain analyses can be chosen. This study have performed a non-linear analysis in the time domain, and a equivalent linear analysis in the frequency domain. The GQ/H model (Groholski et al., 2015), as described in section 3.3, was chosen for the nonlinear backbone formulation.

Step 2a - Soil profile definition

The parameters given in Table 4.6 have been used in step 2 to define the soil profile and properties to the sedimentary layers. Six layers have been used in the analysis, where the thickness, unit weight, shear modulus and shear strength were defined for each layer. The damping ratio was defined using the model by Darendeli (2001). The Darendeli model requires over consolidation ratio (OCR), K_0 , number of loading cycles (N), frequency and plasticity index (PI). OCR and PI are given in Table 4.6 and are adapted from Leynaud et al. (2004). K_0 was set to 0.5, N was set to 10 and the frequency to 1 (Brian Carlton, pers. comm.). Because all of the layers have over 30% clay they have been modeled as clay in the model of Darendeli (2011) (Brian Carlton, pers. comm.).

Table 4.6: Geotechincal parameters used in the soil response evaluation. The parameters have been used to define the soil properties for soil repose analysis in DEEPSOIL . Modified from Leynaud et al. (2004).

Layer	Depth (m)	Clay content (%)	γ_{tot} kN/m^3	Ip (%)	OCR	S_u^{DSS}	Shear Modulus (kPa)
1	0-30	42	16.0	35.7	1.7-1.2	3-80	4000
2	30-65	43	17.8	27.4	1.2	80-130	14833
3	65-123	41	18.3	26.4	1.2	130-260	36167
4	123-152	35	17.4	29.0	1.2	260-325	55000
5	152-270	43	18.9	28.3	1.2	325-580	96667
6	270-309	34	17.6	32.0	1.2	580-700	96667

Step 2b - Profile summary

A summary of the soil profile is given in step 2b. The shear wave velocity in each layer have been calculated based on the unit weight and shear modulus.

Step 2c - Half space and Bedrock definition

Definition of half space and bedrock are given either as rigid half space or elastic half space. The output from EXSIM12 give elastic half space properties. The shear modulus, unit weight and damping ratio are required input parameters here. The shear modulus and unit weight for the bedrock have been found in Ahrens (1995). Because the area are at a transitional zone from continental to oceanic, the values used have been adapted from crust at 15km depth.

The damping ratio are not used in the time domain analysis. The damping ratio is used in the transfer function for EQL, but have negligible effect on the result (Hashash et al., 2015). Therefore it is set to 2 %, which is the default used in the program.

Step 3 - Input motion

The ground motion modeling from EXSIM12 has been imported to DEEPSOIL and is used as the input motion at the base of the soil profile. Before importing the ground motion to DEEPSOIL, the time history was filtered with a Butterworth-filter (code provided by Brian Carlton, 2017), where only the frequencies of interest (0.1 to 50 Hz) was kept.

Step 4 - Viscous/Small-strain damping definition

For sites with long natural periods, which are the case for the soil profile in this study, the frequency-dependent Rayleigh damping formulation can reduce the response at high frequencies significantly in the NL-analysis (Rathje and Kottke, 2011). The recommended damping matrix type from Hashash et al. (2015) was therefore used for the damping definition. This damping matrix are frequency independent.

Step 5 - Analysis control

For the frequency domain analysis, the number of iteration, effective shear strain ratio and the complex shear modulus formulation, the recommended values from Hashash et al. (2015) was used. Number of iteration was set to 15 and the effective shear strain ratio to 0.65. The complex shear modulus formulation is given as $G^* = G(1 + 2i\xi)$ and is frequency independent. For the time domain analysis, the step control was set to flexible, the maximum strain increment to 0.005 and the time history interpolation method to linear interpolation.

Analysis Result

The results from DEEPSOIL is provided by time history plots, stress-strain plots, spectral plots, summary profiles, response spectra summary and are given for both the EQL and

NL analysis. The summary profile display how the PGA varies through the layers and are useful for a general overview. The response spectra summary provide the response spectra for all layers, including the bedrock.

4.5 Input to slope stability anlysis

The various outputs from EXSIM12 and DEEPSOIL was implemented in the slope stability analysis. The FoS and the seismic-induced permanent displacement was calculated for each layer (six layers) to obtain an indication of what layer the failure are most likely to occur.

4.5.1 Pseudo-static Factor of Safety

When evaluating the Factor of Safety, as described in Section 3.4.2, the peak ground acceleration (PGA) from the modeling in EXSIM12 and DEEPSOIL are used as an input to Equation 3.27 for the peak ground acceleration (k, PGA). PGA, in this case the peak horizontal acceleration, are a measure of the largest amplitude of a particular ground motion (Kramer, 1996). The depth and unit weight are the same as in 4.6 Equation 3.25 also require the shear strength of the material in place, the shear strength for each layer are also the same as in Table 4.6.

4.5.2 Seismic-Induced Permanent Displacement

As described in Section 3.4.3, the permanent displacement analysis used in this study, implement the spectral acceleration at 1.5 the fundamental period. This information can be extracted from the output of EXSIM12 and DEEPSOIL.

The calculation of permanent displacement also require the fundamental period and the critical acceleration. The calculation of critical acceleration (k_y, Eq. 3.4) and the fundamental period (Table 4.1) are the same as for the maximum distance. MATLAB-code for extracting information and calculation can be found in Appendix A.

Chapter 5

Results

This Chapter will present the result from the modeling and analysis performed. Five fault will be presented here, chosen based on their various distance to initiation area. The rest of the fault are located at distances in between the fault located the furthest away and the closest fault, and it have therefore been assumed that the five fault presented here will give an overview also representative for the other faults. The results from the remaining faults can be found in Appendix B, C and D.

5.1 Maximum distance from fault to site

The result from the maximum distance from fault to site will be presented in this section. The plots presented illustrate the maximum distance from the ruptured fault to the location of failure, if an earthquake should be the responsible trigger mechanism for the Storegga Slide. The results is based on the pseudo-static method, and the distances here are therefore be the maximum distances to produce instability in the slope. The results will not give an indication of release or not.

Figure 5.1 present the maximum distance based on Campbell (2003) ground motion prediction equation. The maximum distance increase with increasing magnitude and slope angle. This imply that the fault can be located further away from the release area if the slope are steeper. The same applies for magnitudes of the earthquake, a higher magnitude imply that the distance can be greater in order to produce instability. For a flat ground, the maximum distance for a magnitude 7 are calculated to be 26.5 km. An increase in slope angle show that the maximum distance is increasing steadily. After approximately 8° the maximum distance increase more drastically.

An interesting result for a magnitude 5 event (Figure 5.1), is that the calculation does not predict a maximum distance before the slope angle has reached 3.5°. Another observation is the increase in distance with increasing slope angle are shifted towards higher slope angles for smaller magnitude events.

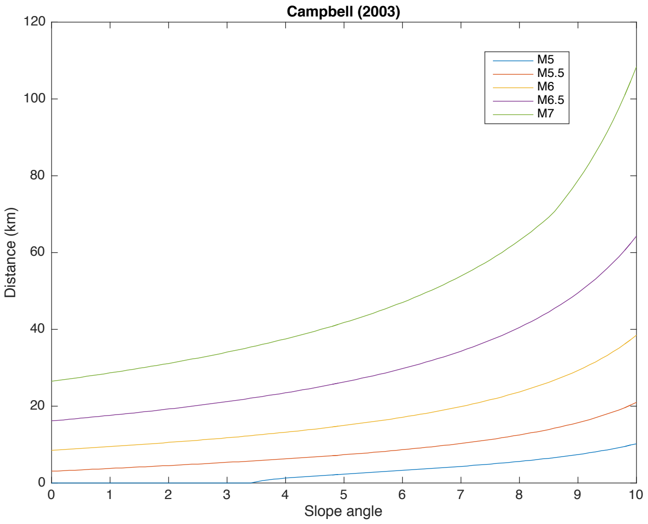

Figure 5.1: Plot displaying the calculated maximum distance from fault to site by the Campbell (2003) GMPE. The maximum distance increase with increasing magnitude and slope angle.

Figure 5.2 present the maximum distance when the NGA-WEST2 ground motion prediction equation is applied. The application of this GMPE shows a small difference in calculated distances. At a flat ground the maximum distance for a magnitude y event are 28.9 km, and the increase is more gradually than for the Campbell (2003) calculation. At 8° the predicted maximum distance for a magnitude 7 event is 51.87 km, while for Campbell (2003) the distance is 63.2 km. The main differences between the two GMPEs is that the NGA-WEST2 equation predicts a maximum distance for a magnitude 5 event also for slope angles below 3.5°.

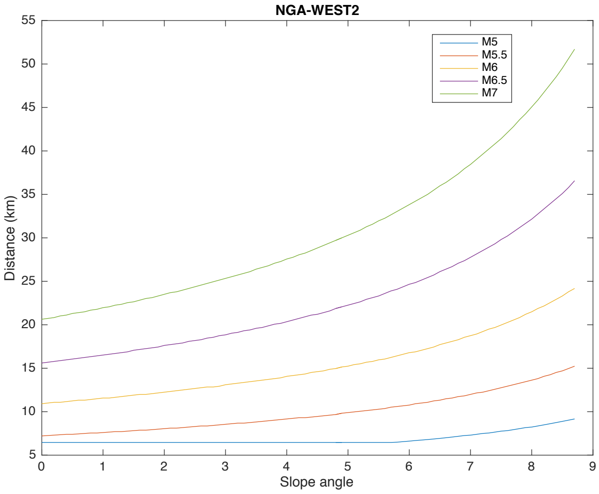

Figure 5.2: Plot displaying the calculated maximum distance from fault to site by the NGA-WEST2 GMPE. The maximum distance increase with increasing magnitude and slope angle.

5.2 Ground motion modeling - EXSIM12

The EXSIM12 algorithm was used for ground motion modeling of the 14 selected faults in bedrock. In this section, an example from SRN fault are shown, Figure 5.3 to 5.7. The figures illustrate ground motion at bedrock level. The results from the remaining faults can be found in Appendix B. Note that the EXSIM12 results is displayed in cm/sec^2. The gray line in the figures represent the faults, because the use of Wells and Coppersmith (1994) equation, the entire fault in gray will not rupture, but only a part of it. The part that has ruptured can be recognized by the high ground motion predicted close to the fault.

As seen in the figures below, the ground motion are highest close to the fault and attenuates with increasing distance. The same applies for the depth. With increasing depth of the fault, the ground motion recorded at top of the bedrock decrease.

The length and width of the fault are, as mentioned, calculated with Wells and Coppersmith (1994), it is therefore expected that the resulting ground motion will be approximately the same for the same magnitude and depth. The difference for minimum acceleration recorded are small, while the difference in maximum acceleration are higher.

5.2.1 Magnitude 7

The maximum acceleration predicted for a magnitude 7 event at 1km depth are $1016 cm/s^2$, which is close to the fault. The minimum acceleration is $4.451 cm/s^2$. As observed in Figure 5.3, the contour line of $200 cm/s^2$, $100 cm/s^2$ and $50 cm/s^2$ cross the line of assumed initiation area.

For a magnitude 7 event at 5km depth, the maximum acceleration is $490 cm/s^2$, which is lower than in the case of 1km depth. The contour lines of $100 cm/s^2$ and 50 cm/s^2 are also well within the assumed failure area. The $200 cm/s^2$ contour line are just within the area. The minimum acceleration is $4.459 cm/s^2$, and are not that different from an event at 1km.

An event at 10km depth with magnitude 7 will predict a maximum acceleration of $269 cm/s^2$, which is a significant decrease compared to the event at 1km depth. The minimum acceleration is $4.619 cm/s^2$, which is not a significantly different from the 1km depth event. The contour lines of $100 cm/s^2$ and $50 cm/s^2$ are again well within the assumed initiation area.

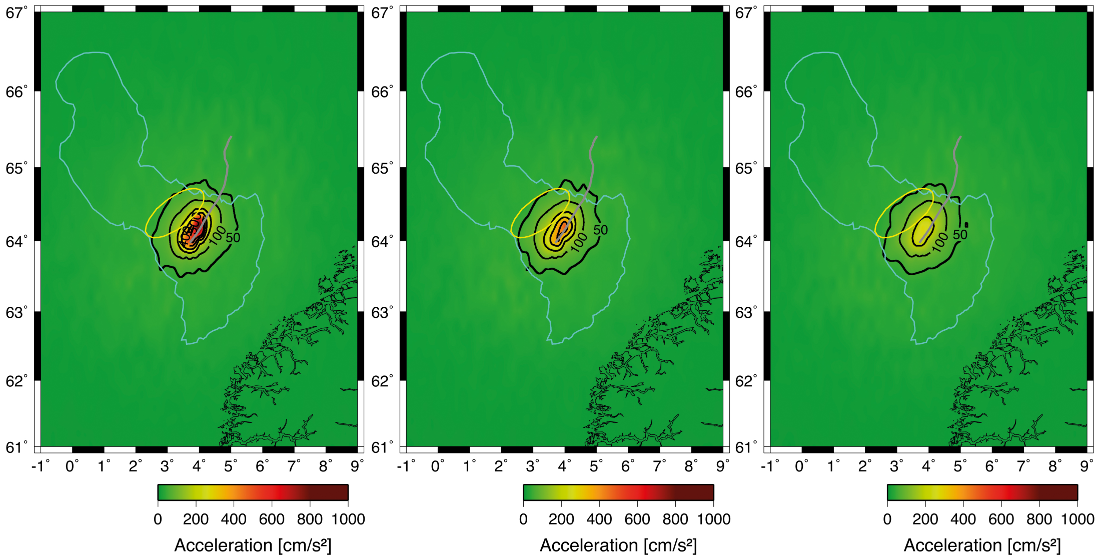

Figure 5.3: Ground motion from a magnitude 7 event at 1, 5 and 10km depth at the SRN fault. The blue are outline of the Storegga Slide, yellow ellipse are the assumed initiation area, the fault are marked with gray.

5.2.2 Magnitude 6.5

A magnitude 6.5 event at 1km depth predicts a maximum acceleration of $897.1cm/s^2$, and a minimum of $3.419cm/s^2$. The contour lines of 100 and $50cm/s^2$ are within the initiation area. At 5km depth the maximum and minimum acceleration are respectively $515cm/s^2$ and $3.519cm/s^2$. The contour lines of $100cm/s^2$ and $50cm/s^2$ are also within the initiation area. For the 10km depth event, the maximum acceleration is $327.2cm/s^2$ and minimum acceleration is $3.327cm/s^2$. The contour lines of $100cm/s^2$ and $50cm/s^2$ are for this case also within the initiation area.

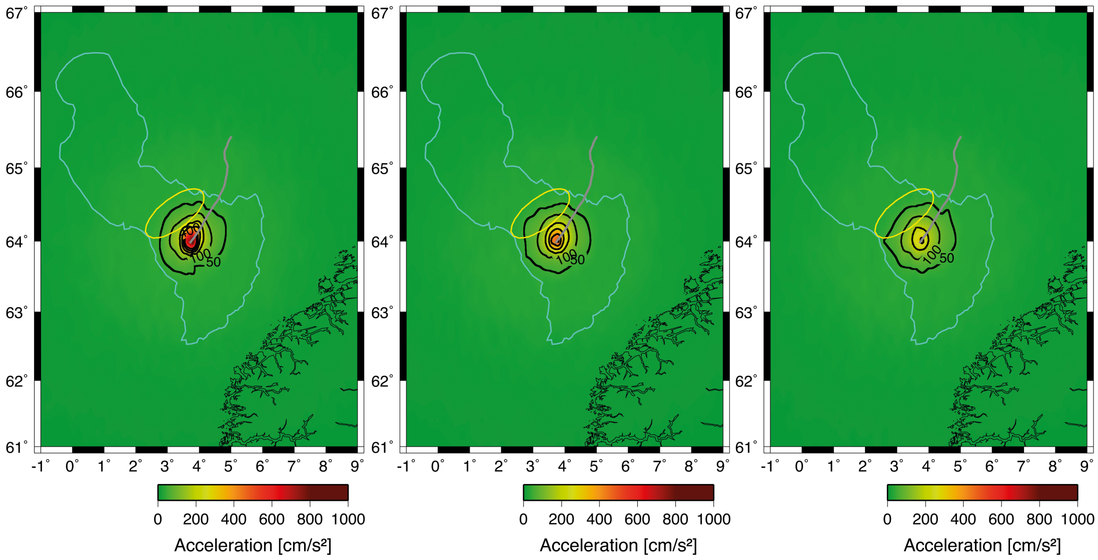

Figure 5.4: Ground motion from a magnitude 6.5 event at 1, 5 and 10km depth at the SRN fault. The blue are outline of the Storegga Slide, yellow ellipse are the assumed initiation area, the fault are marked with gray.

5.2.3 Magnitude 6

A magnitude 6 event at 1km depth predicts a maximum acceleration of $952.5 cm/s^2$ and a minimum of $1.945 cm/s^2$. The contour line of $50 cm/s^2$ are within the initiation area, while the $100 cm/s^2$ contour line barely cross the line. For a event at 5km the maximum and minimum acceleration are respectively $439.4 cm/s^2$ and $1.965 cm/s^2$. The contour line of $50 cm/s^2$ are well within the initiation are, while the $100 cm/s^2$ do not cross the line. The maximum and minimum acceleration for a 10km depth event are respectively $250 cm/s^2$ and $2.024 cm/s^2$.

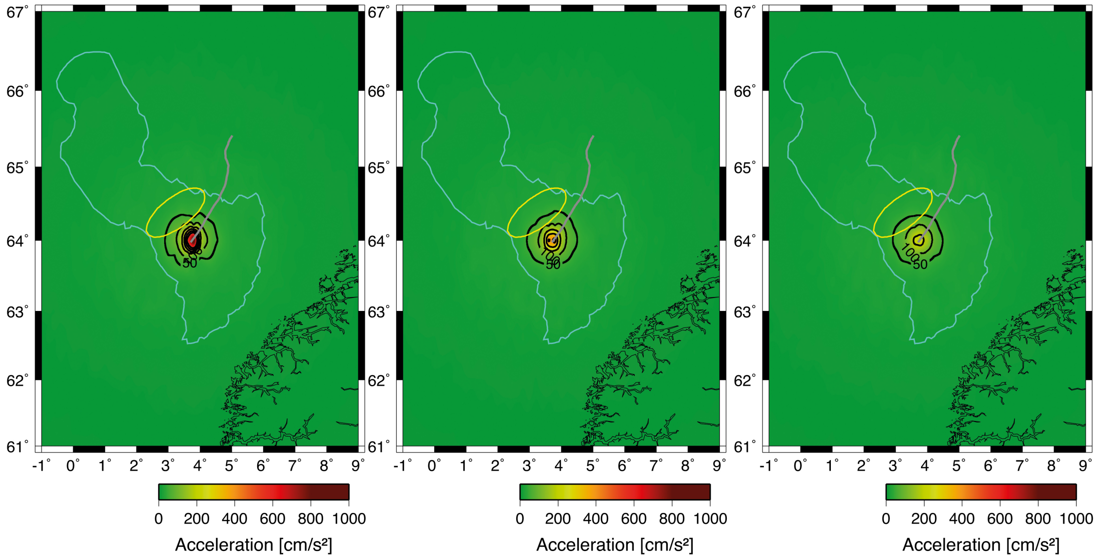

Figure 5.5: Ground motion from a magnitude 6 event at 1, 5 and 10km depth at the SRN fault. The blue are outline of the Storegga Slide, yellow ellipse are the assumed initiation area, the fault are marked with gray.

5.2.4 Magnitude 5.5

A magnitude 5.5 event at 1km depth predicts a maximum acceleration of $820.4 cm/s^2$ and a minimum of $1.104 cm/s^2$. The contour line of $50 cm/s^2$ are within the initiation area, however does not reach as far into the area as for the larger magnitude events. For a 5km event the maximum acceleration is $354.4 cm/s^2$ and minimum acceleration is 1.094. The contour line of $50 cm/s^2$ are also within the initiation area. The 10km depth appears to have be displaced somewhere in the modeling process and will not be discussed further.

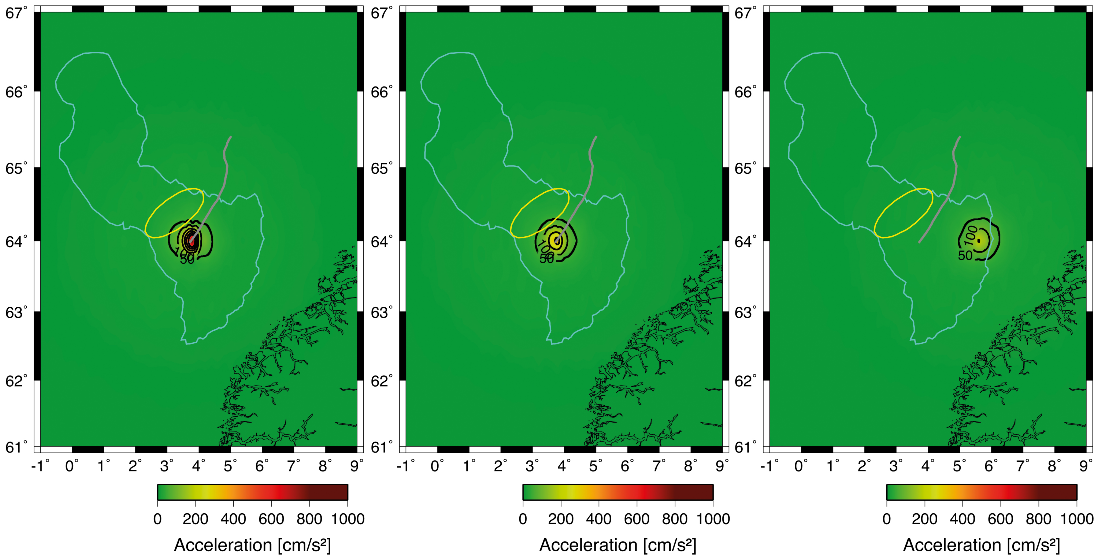

Figure 5.6: Ground motion from a magnitude 5.5 event at 1, 5 and 10km depth at the SRN fault. The blue are outline of the Storegga Slide, yellow ellipse are the assumed initiation area, the fault are marked with gray.

5.2.5 Magnitude 5

A magnitude 5 event predicts a maximum acceleration of 310.9cm/s^2 and a minimum acceleration of 0.4660cm/s^2, which is a significant difference from the magnitude 7 and 6.5 events. No contour lines are within the initiation area, indicating that the acceleration are below 50cm/s^2. The 5km depth event have a maximum and minimum acceleration of respectively 168.4cm/s^2 and 0.4652cm/s^2, with no contour lines within the initiation area. The maximum and minimum acceleration are 101.6cm/s^2 and 0.4624cm/s^2 for the 10km depth event, also for this case no contour lines are within the initiation area.

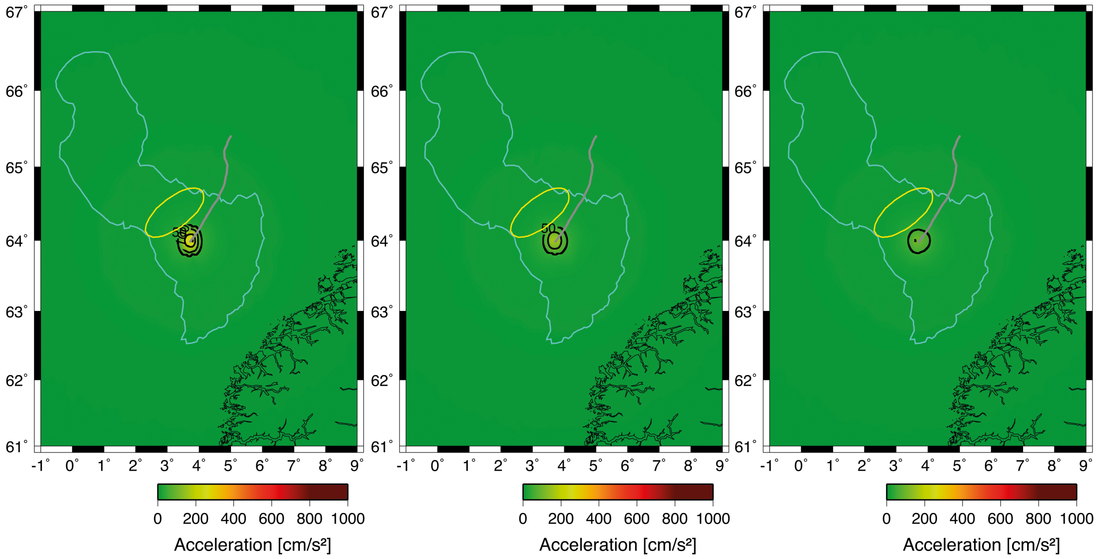

Figure 5.7: Ground motion from a magnitude 5 event at 1, 5 and 10km depth at the SRN fault. The blue are outline of the Storegga Slide, yellow ellipse are the assumed initiation area, the fault are marked with gray.

5.3 Soil Response - DEEPSOIL

DEEPSOIL was used for modeling of the sediment response. Both equivalent linear and non-linear analysis was performed. An example comparing the equivalent linear and non-linear approach are included for both the PGA and the Response spectra. Fourteen faults was modeled, but only the modeling of five faults for the case of a magnitude 7 event at 1km depth will be presented here. The remaining response spectra can be found in Appendix C.

5.3.1 Comparison between equivalent linear (EQL) and non-linear approach(NL)

Figure 5.8 display the resulting PGA for the non-linear approach and the equivalent linear approach. The PGA from top of the bedrock (layer 6) are not included in the figure because the difference is so large that the changes in the sediments would not be observed. Nevertheless, the PGA is attenuated through layer 6 up to the bottom of layer 5. The main difference between the EQL and NL in Figure 5.8 is that the PGA attenuate through layer 6, and increases from bottom of layer 5 up to the surface for the NL approach. For the EQL approach, the PGA attenuates up to layer 2, before increasing up to the surface. The general trend when comparing the EQL and the NL approach is that the EQL systematically predicts a higher PGA than the NL-approach.

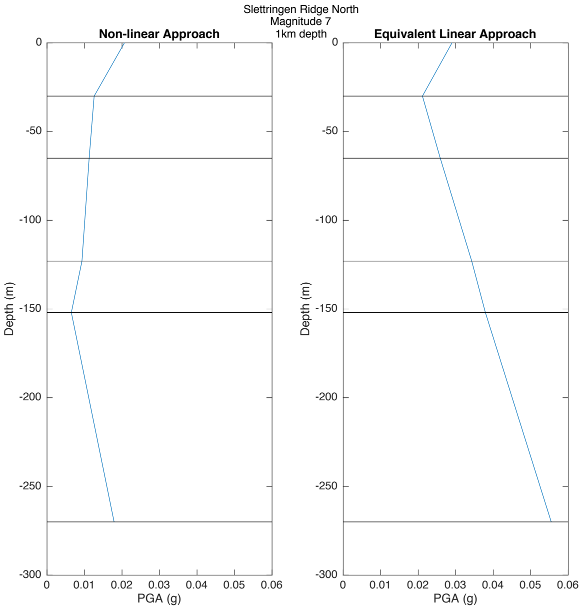

Figure 5.8: Comparison of the EQL and NL approach for a magnitude 7 event at 1km depth at the SRN fault. The black lines represent the layer boundaries.

5.3.2 Peak Ground Acceleration

The following will only include the results from the NL-approach, because this approach is believed to better capture the actual sediment response of ground motion by including the changes in stiffness. Figure 5.9 to 5.13 display how the PGA varies through the sediment deposits, note that the axis are not the same for all plots. The PGA at base of layer 6 (or top of bedrock) has been excluded, due to relative high values in order to better observe the effect in the sediment deposit. The values can be found in Table 5.1., where it is observed that the PGA decreases with increasing distance from initiation area. The only exception are the VG fault, which have a larger PGA than SRN. The PGA values calculated will be used to evaluate the FoS in the six layers of the soil profile. The PGA plot are for all faults a magnitude 7 event at 1km depth.

Table 5.1: Peak ground acceleration (PGA) at base of layer 6 for the five fault presented in this section.

Fault	PGA Layer 6
SRN	0.0671g
VG	0.0735g
OL	0.0241g
KFC	0.0231g
MTG	0.0185g

Slettringen Ridge North (SRN)

Base of layer 5 for a magnitude 7 event at 1km depth at the SRN fault has a PGA value of 0.0179g, before decreasing drastically to 0.0065g to base of layer 4. Through layer 4 and to the base of layer 1 the PGA increases to 0.0126g, before a large increase up to 0.0206g can be observed at the surface of the sediment profile.

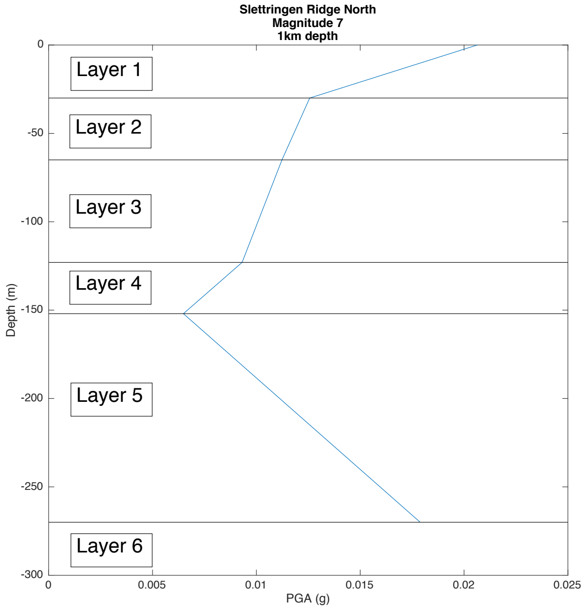

Figure 5.9: Plot illustrating how the PGA varies through the sediment deposit for a magnitude 7 event at 1 km depth at the SRN fault.

Vigra High - Grip High (VG)

A magnitude 7 event at 1km depth at the VG fault result in a PGA of 0.016g at the base of layer 5. The PGA decreases up to bottom of layer 4 to 0.0073g. Through layer 4, there is a small increase of 0.0014g, before the PGA has a small decrease of 0.0006g up to the base of layer 2. The PGA increases again through layer 2, and have a larger increase to the surface of the sediment profile where the PGA is 0.0191g.

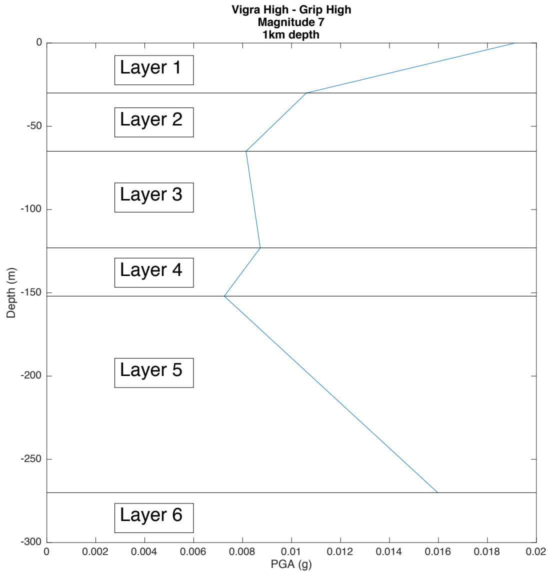

Figure 5.10: Plot illustrating how the PGA varies through the sediment deposit for a magnitude 7 event at 1 km depth at the VG fault.

Ormen Lange (OL)

The OL fault has a PGA value of 0.0115g at base of layer 6 for a magnitude 7 event at 1km depth, before decreasing by 0.0075g up to base of layer 5. The PGA then increases up to base of layer 2, where the PGA again have a decrease up to base of layer 1. Up to the surface the PGA increases to 0.0118g.

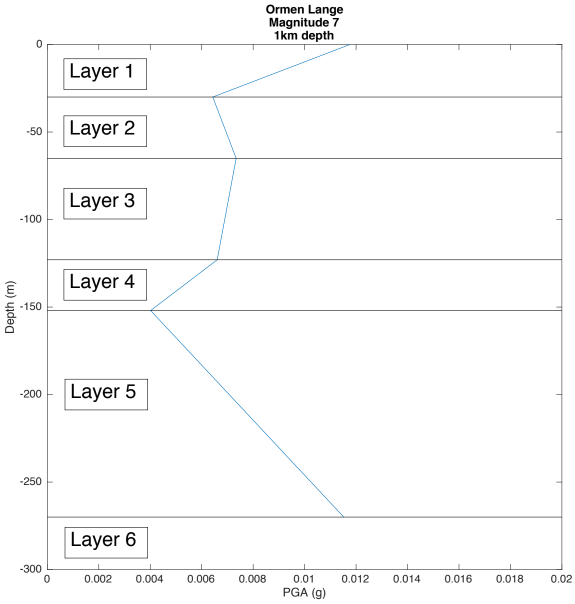

Figure 5.11: Plot illustrating how the PGA varies through the sediment deposit for a magnitude 7 event at 1 km depth at the OL fault.

Klakk Fault Complex (KFC)

For the KFC fault, the PGA at base of layer 5 are 0.0107g, before decreasing to 0.005g at base of layer 4. There is an increase up to base of layer 2, where a small decrease of 0.001g are observed up to base of layer 1. The PGA then increases to 0.0106g at the surface of the soil profile.

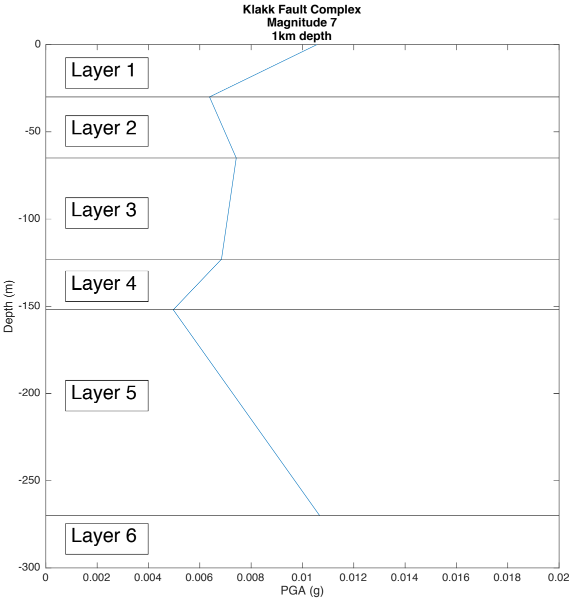

Figure 5.12: Plot illustrating how the PGA varies through the sediment deposit for a magnitude 7 event at 1 km depth at the KFC fault.

Makrell Horst - Tampen Spur - Gnausen High (MTG)

At the base of layer 5 a PGA of 0.0092g are observed from a magnitude 7 at 1km depth event. As observe for the other four fault the PGA decrease up to base of layer 4. The PGA then increases up to base of layer 1 before a large increase up to 0.0075g are observed at the surface.

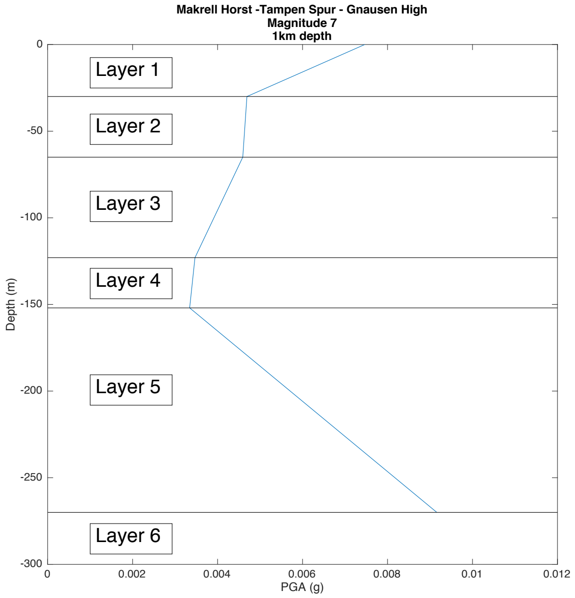

Figure 5.13: Plot illustrating how the PGA varies through the sediment deposit for a magnitude 7 event at 1 km depth at the MTG fault.

5.3.3 Peak Spectral acceleration

Figure 5.14 and 5.15 display the response spectra at the initiation area for a magnitude 7 event at 1km depth at the SRN fault and the MTG fault. A comparison between the NL-approach and the EQL-approach has been done for the various faults, magnitudes and depths has been done. The SRN and the MTG has been included in this chapter, while the remaining response spectra can be found in Appendix C.

Figure 5.16 to 5.20 display the response spectra from a magnitude 7 event at 1km depth. The black lines represent the input ground motion at the base of the sediment profile, while the colored lines represent the sedimentary layers. At high frequencies (or low period) it is observed that the input ground motion is significantly attenuated in the sediments compared to the bedrock. At lower frequencies or longer periods, we can observe that the input ground motion is significantly amplified in the sediment layers.

When evaluating the response spectra, it becomes clear that slope stability analysis should not be performed only with PGA, because amplification could occur at lower frequencies, which is not captured by evaluating only the PGA.

Comparison between the EQL- and NL-approach

In Figure 5.14 and 5.15, response spectra from the EQL-approach and the NL- approach are compared. In the response spectra for NL, it is observed attenuation of the ground motion at high frequencies, and amplification in the sedimentary layers at lower frequencies.

For the EQL-approach, the ground motion in the sediment layers at moderate periods are significantly amplified. At a period of 0.18s, the ground motion in layer 5 exceeds the bedrock motion. At lower frequencies, there is observed amplification in the sedimentary layers for both approaches, but the amplification are higher for the EQL-approach.

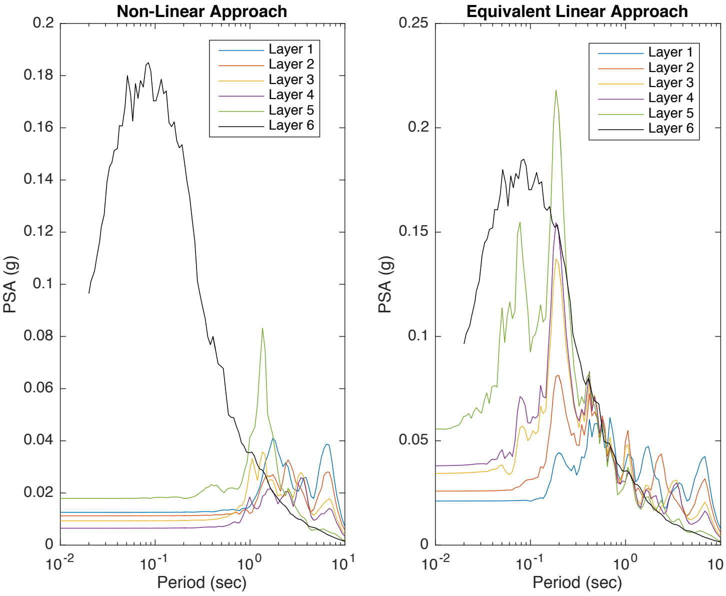

Figure 5.14: Response spectra for the NL-approach and the EQL-approach. Magnitude 7 event at 1km depth at the SRN fault. The accelerations are at the bottom at each layer, i.e. the black line are the acceleration at top of bedrock and at bottom of soil profile. This fault is located close to the initiation area.

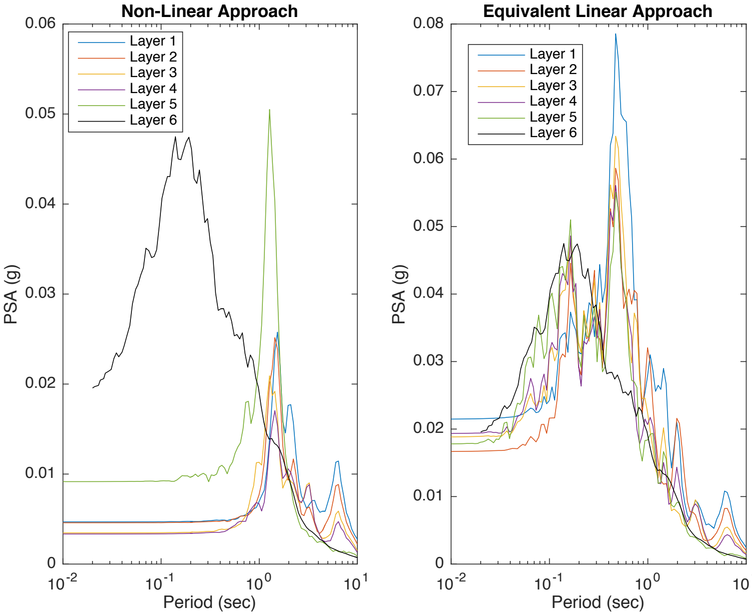

Figure 5.15: Response spectra for the NL-approach and the EQL-approach. Magnitude 7 event at 1km depth at the MTG fault. The accelerations are at the bottom at each layer, i.e. the black line are the acceleration at top of bedrock and at bottom of soil profile. The fault is located at a greater distance from the initiation are than the SRN fault.

Slettringen Ridge North

On Figure 5.16 we can observe that at high frequencies the ground motion in the sediments are significantly attenuated compared to the bedrock. At a period around 1.4s the ground motion in the sediments experience a significant amplification in layer 5. Layer 1 and 3 experience a small amplification at the same period, while the remaining layers does not show an amplification that correspond to a higher acceleration than in the bedrock. At the lowest frequencies, all layers experience an amplification causing a higher acceleration than the bedrock, The highest amplification is in layer 1, and decreases with increasing depth. The PSA of the different layers are shown in Table 5.2.

Table 5.2: Peak spectral acceleration (PSA) for a magnitude 7 event at 1km depth at Slettringen Ridge North.

Layer	PSA (g)	Period (sec)
1	0.041	1.7384
2	0.0327	2.5240
3	0.0357	1.3558
4	0.0259	3.4438
5	0.0831	1.3668
6	0.1850	0.0850

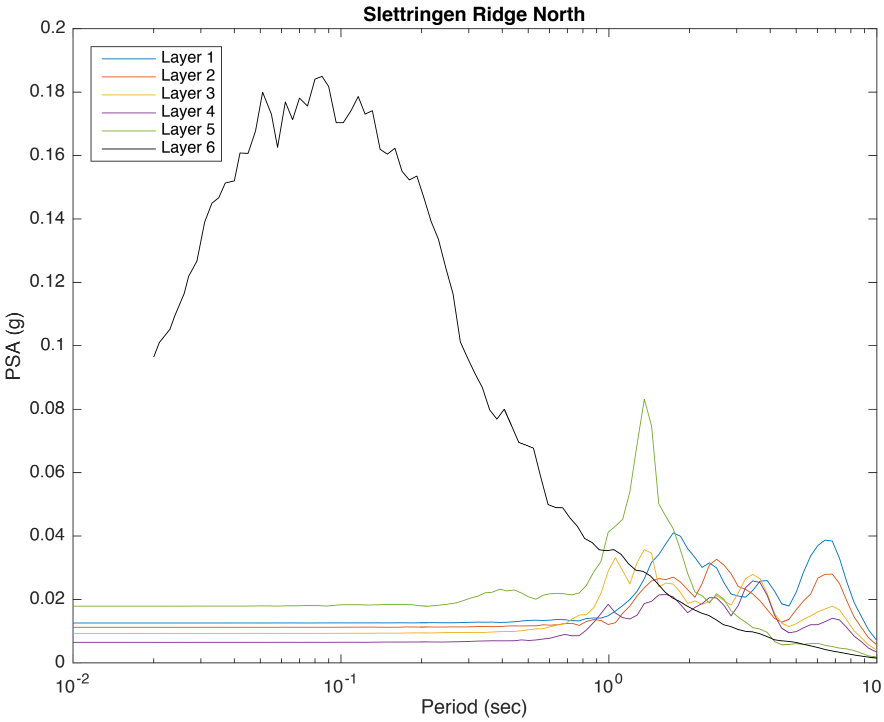

Figure 5.16: Peak spectral acceleration, magnitude 7 1km depth event for the SRN fault. The accelerations are at the bottom at each layer, i.e. the black line are the acceleration at top of bedrock and at bottom of soil profile.

Vigra High - Grip High

The bedrock for the VG fault displays a higher PSA compared to the SRN fault, but also for this case the ground motion in the sediment layers are strongly attenuated. The amplification in layer 5 at 1.4s are not as large, and also layer 3 shows a smaller amplification than for SRN. The remaining layers does not show any amplification compared to bedrock at the same period. Layer 4 does not have any significantly amplification around 3.6s. The PSA in layer 1 are observed at lower frequencies than the other layers. At the lowest frequencies, layer 1 show the greatest amplification. The PSA of the different layers are shown in Table 5.3.

Table 5.3: Peak spectral accelerations in the different layers for a magnitude 7 event at the VG fault.

Layer	PSA (g)	Period (sec)
1	0.0289	6.4110
2	0.021	1.5352
3	0.0348	1.3558
4	0.020	3.6646
5	0.0724	1.3558
6	0.2824	0.0550

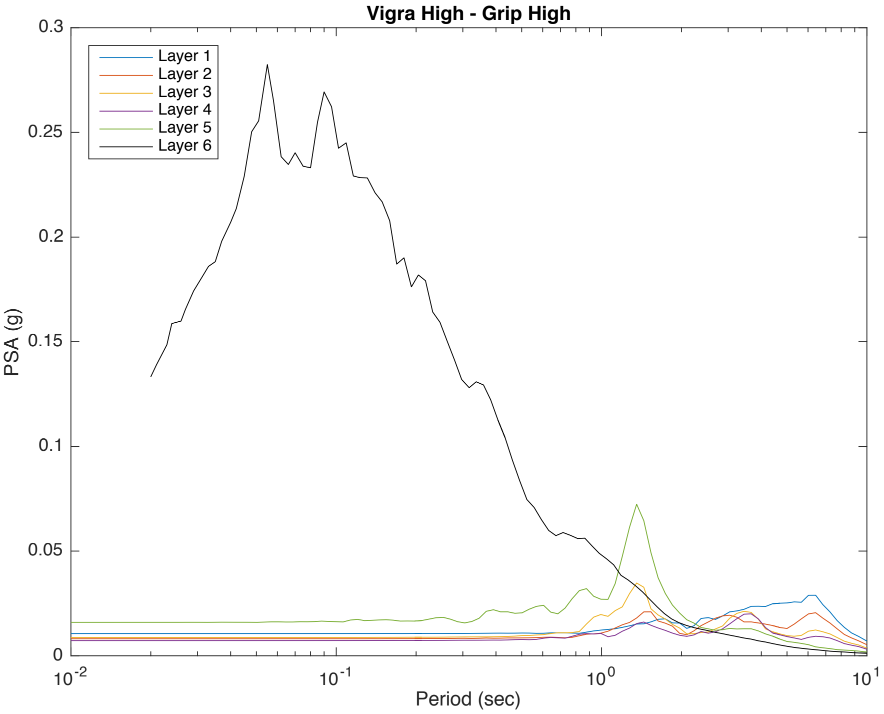

Figure 5.17: Peak spectral acceleration, magnitude 7 1km depth event for the VG fault. The accelerations are at the bottom at each layer, i.e. the black line are the acceleration at top of bedrock and at bottom of soil profile.

Ormen Lange

The acceleration at higher frequencies are most significant in layer 6, as for the two previously examples, but the PSA are lower. The ground motion in the sediment layers are significantly attenuated at high frequencies. All sediment layers show and amplification at a period of 1.4s, layer 2 and layer 5 also have an higher PSA than for the VG fault. At the lowest frequencies, the same as for the SRN and VG are observed; highest acceleration in layer 1. For layer 1, the PSA are also observed at slightly lower frequencies than the other layers. The PSA of the different layers are shown in Table 5.4.

Table 5.4: Peak spectral accelerations in the different layers for a magnitude 7 event at the OL fault.

Layer	PSA (g)	Period (sec)
1	0.0238	2.2290
2	0.0246	1.3558
3	0.0311	1.3558
4	0.0191	1.3558
5	0.0772	1.2741
6	0.0836	0.1230

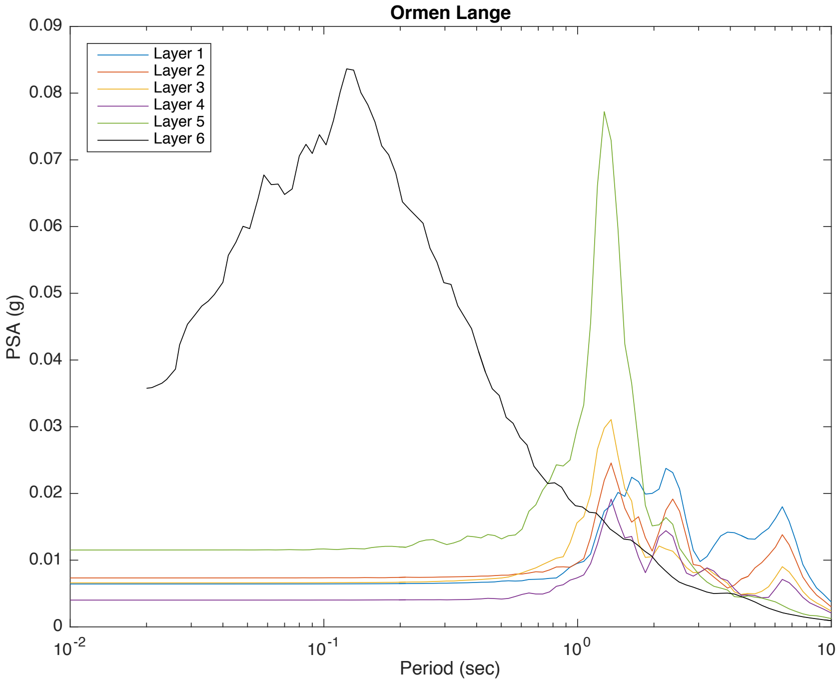

Figure 5.18: Peak spectral acceleration, magnitude 7 1km depth event for the OL fault. The accelerations are at the bottom at each layer, i.e. the black line are the acceleration at top of bedrock and at bottom of soil profile.

Klakk Fault Complex

The highest acceleration in layer 6 is again observed at the higher frequencies, where the ground motion observed in the sediment layers are significantly attenuated. The PSA for this case is also lower than the three previous examples. An interesting observation in layer 5 are that the PSA exceeds the PSA for layer 6 (or bedrock) at a period of 1.4s, and are also higher than the PSA compared to the VG fault. The PSA in layer 1 is again shifted to lower frequencies compared to the rest of the layers, as observed for the other faults. At the lowest frequencies the amplification is largest in layer 1, and decreases with increasing depth. The PSA of the different layers are shown in Table 5.5.

Table 5.5: Peak spectral accelerations in the different layers for a magnitude 7 event at the KFC fault.

Layer	PSA (g)	Period (sec)
1	0.0277	2.2290
2	0.0299	1.3558
3	0.0322	1.3558
4	0.0195	1.3558
5	0.0771	1.3558
6	0.0649	0.090

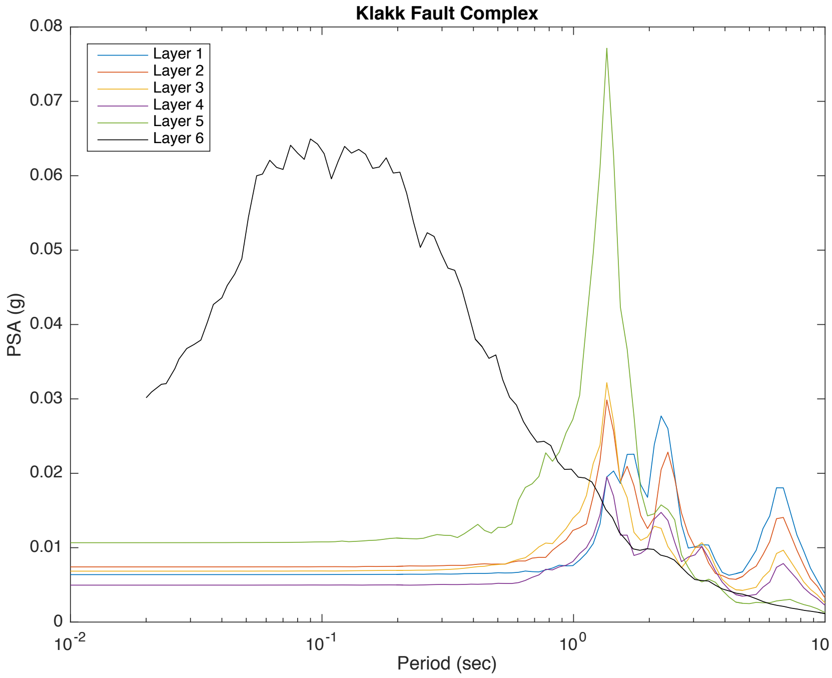

Figure 5.19: Peak spectral acceleration, magnitude 7 1km depth event for the KFC fault. The accelerations are at the bottom at each layer, i.e. the black line are the acceleration at top of bedrock and at bottom of soil profile.

Makrell Horst - Tampen Spur - Gnausen High

At the highest frequencies the PSA for layer 6 can be observed, and attenuation of ground motion in the sediment layers. The PSA in layer 6 are the smallest of the presented cases. The PSA for all sediment layers observed at a period of approximately 1.4s. Also for this case the PSA for layer 5 exceeds the PSA of bedrock. At the lowest frequencies, layer 1 again have the greatest amplification which decrease for increasing layer depth. The PSA of the different layers are shown in Table 5.6.

Table 5.6: Peak spectral accelerations in the different layers for a magnitude 7 event at the MTG fault.

Layer	PSA (g)	Period (sec)
1	0.0258	1.5352
2	0.0252	1.4427
3	0.0209	1.2741
4	0.01709	1.4427
5	0.0505	1.2741
6	0.0415	0.1020

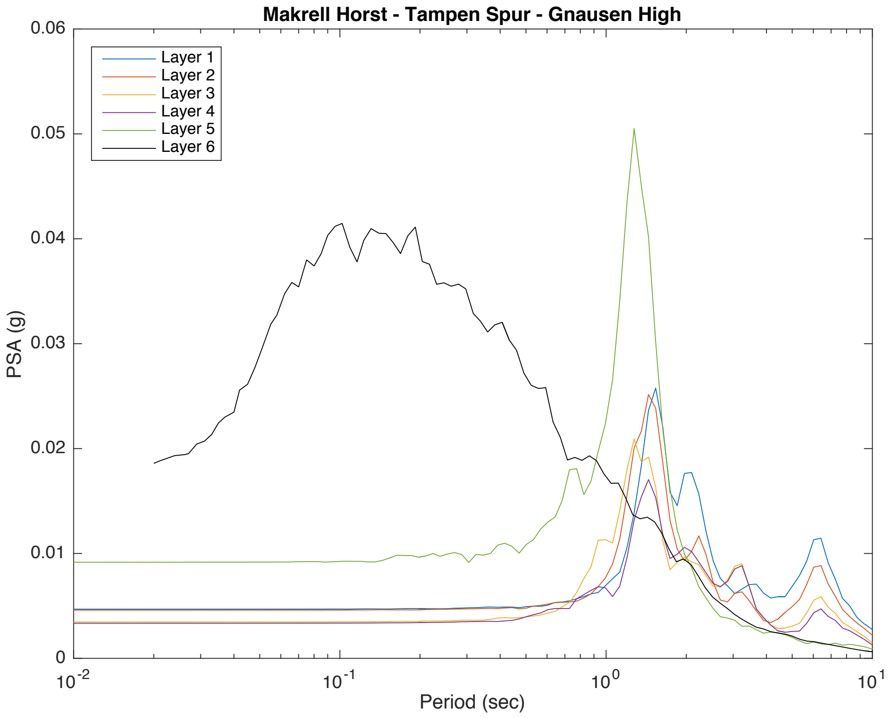

Figure 5.20: Peak spectral acceleration, magnitude 7 1km depth event for the MTG fault. The accelerations are at the bottom at each layer. i.e. the black line are the acceleration at top of bedrock and at bottom of soil profile.

5.4 Factor of Safety

To test how the parameters affect the slope stability, the FoS was calculated by vary the shear strength, unit weight and the acceleration.

Shear strength

The shear strength was tested for four values, with the other parameters kept constant, see Table 5.7 for input parameters. The shear strength are a resisting force, therefore it is expected that the FoS will decrease with decreasing shear strength. The result from shear strength's effect on slope stability can be seen on Figure 5.21. As expected, a higher shear strength result in a higher FoS, and require a higher slope angle in order to have an effect on the slope stability. Table 5.8 gives the FoS equal to or smaller than 1. The FoS for a slope angle equal to 0° are very high, and because a high FoS yields a very stable slope they are not shown on the plot in Figure 5.21.

Table 5.7: Input parameters for effect of shear strength on the Factor of Safety.

Parameters	Value
Shear strength	700, 500, 300, 100 kPa
Acceleration	0.1g
Unit weight	$19kN/m^3$
Thickness	300m

Table 5.8: Factor of Safety equal or less than 1 for various shear strength. FoS ≤ 1 indicate that the slope is unstable

Shear Strength	FoS ≤ 1	FoS at 0°
700 kPa	15°	368.4
500 kPa	10.7°	263.2
300 kPa	6.4°	157.9
100 kPa	2.1°	52.63

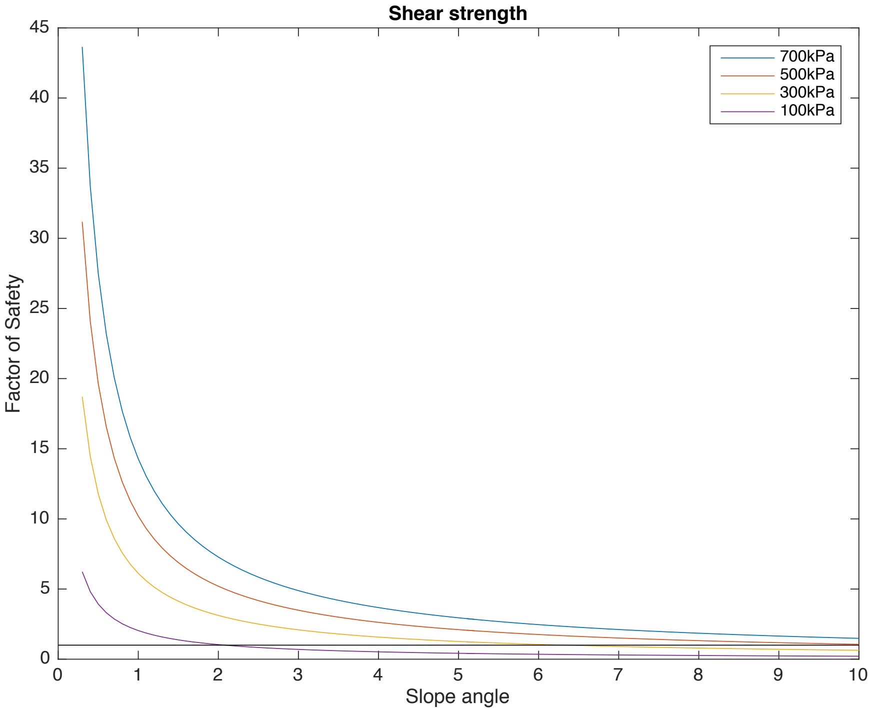

Figure 5.21: Plot of the FoS with slope angle for various shear strength. Higher shear strength yields higher FoS. The black line represent FoS = 1. The slope angles in this plot ranges from 0.3 to 10° in order to observe the difference clearer.

Unit Weight

Four different values of unit weight was tested for the FoS calculation, with all other parameters kept constant (Table 5.9). The unit weight can be identified as a driving force, because the gravity effect will increase as the weight of the soil mass increase. It was expected that increasing unit weight will result in a decrease in FoS. The slope angle when FoS equals to or are smaller than 1 can be seen in Table 5.10.

Table 5.9: Input parameters for effect of unit weight on the Factor of Safety.

Parameters	**Value**
Shear strength	$500kPa$
Acceleration	0.1g
Unit weight	19, 17, 15, $13kN/m^3$
Thickness	300m

Figure 5.22 display the results from the FoS calculation with varying unit weight. As expected a high unit weight results in a decrease in FoS, indicating that with a high unit weight the slope angle required for instability decreases.

Table 5.10: Factor of Safety equal or less than 1 with various unit weights. FoS ≤ 1 indicate that the slope is unstable.

Unit Weight	FoS ≤ 1	FoS at 0°
19 kN/m^3	10.7°	263.2
17 kN/m^3	13.8°	294.1
15 kN/m^3	19.5°	333.3
13 kN/m^3	33.7°	384.

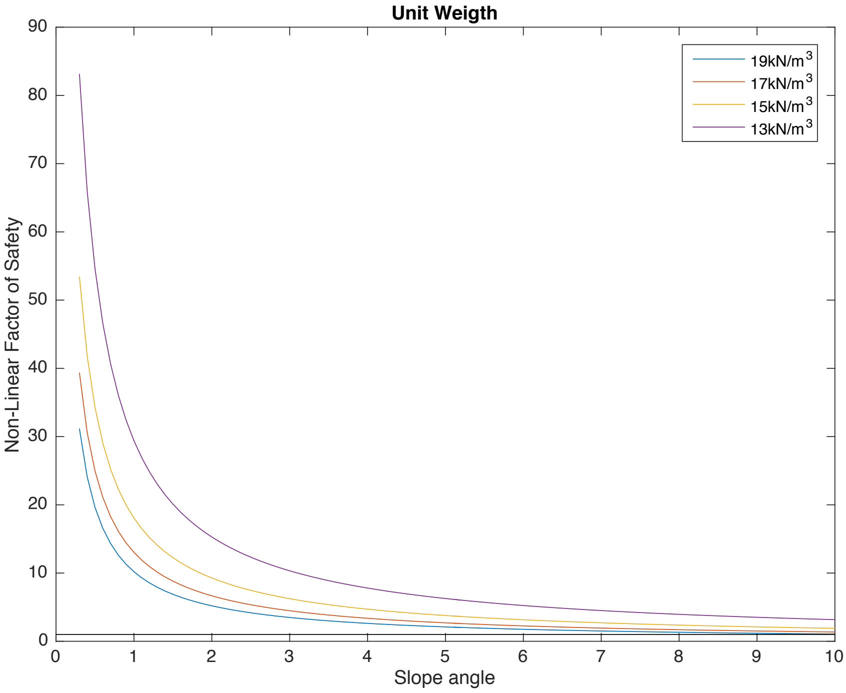

Figure 5.22: Plot of the FoS with slope angle for various unit weight. Higher unit weight yields smaller FoS. The black line represent FoS = 1. The slope angles in this plot ranges from 0.3 to 10° in order to observe the difference clearer.

Acceleration

Six acceleration values effect on FoS was tested with all other parameters kept constant (Table 5.11). Earthquake acceleration can be seen as a driving force, together with the unit weight. The extra stresses induced by the cyclic loading by earthquakes are expected to increase the driving force, thus reducing the FoS. Table 5.12 show the FoS ≤ 1 for the various acceleration values.

Table 5.11: Input parameters for effect of acceleration on the Factor of Safety.

Parameters	**Value**
Shear strength	$500kPa$
Acceleration	0.5, 0.2, 0.1, 0.05, 0.02, 0.01g
Unit weight	$19kN/m^3$
Thickness	300m

Figure 5.23 display the calculated FoS for the various accelerations depending on the slope angle. Rather unexpected, there is little difference between the accelerations values. The only exception is the higher acceleration, where the FoS at lower angle are lower than for the low acceleration. Around 5° the calculated FoS are approximately the same. The difference for when FoS ≤ 1 are only at 0.1 to 0.2°.

Table 5.12: Factor of Safety equal or less than 1 for various input acceleration. FoS ≤ 1 indicate that the slope is unstable

Acceleration	FoS ≤ 1	FoS at 0°
0.5	10.5°	52.63
0.2	10.6°	131.6
0.1	10.7°	263.2
0.05	10.7°	526.3
0.02	10.7°	1316
0.01	10.7°	2632

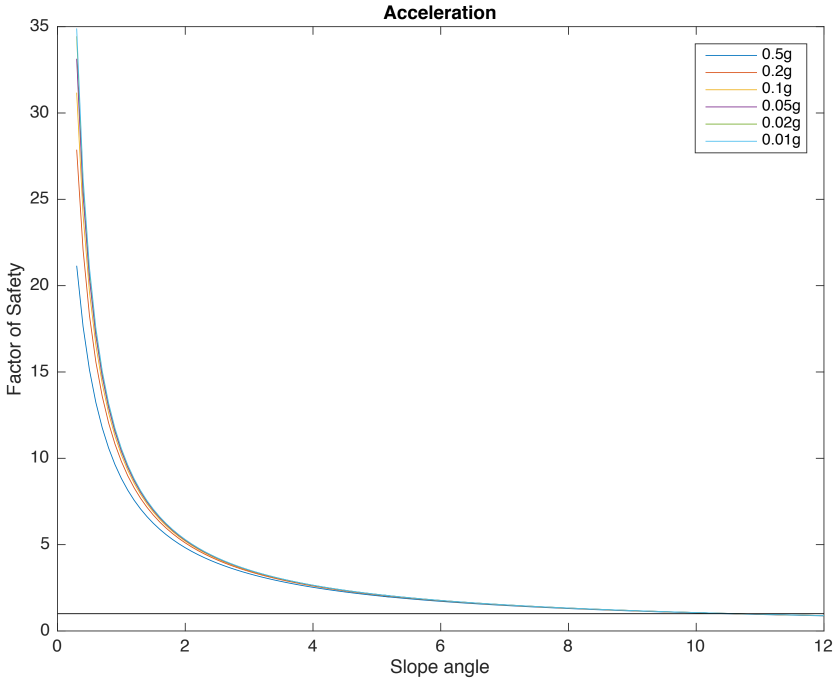

Figure 5.23: Plot of the FoS with slope angle for various acceleration. Higher acceleration yields smaller FoS at low inclination. The black line represent FoS = 1. The slope angles in this plot ranges from 0.3 to 12° in order to observe the difference clearer.

Variation of Factor of Safety through the layers

The different layers in the soil profile have different properties and the slip layer varies through the Storegga Slide, from deep failure to shallower upslope (Bryn et al., 2005). Therefore, I wanted to test how the FoS changes from layers to layers. It is reasonable to believe that a FoS ≤ 1 in any layer will cause instability in the overlying layer as well. The ground motion modeling from EXSIM12 and DEEPSOIL have been used as input acceleration, respectively in layer 6 and in layer 1 to 5.

The soil column, described in section 4.4.1, are assumed to be unconsolidated sediment deposits on top of bedrock, i.e. hard/solid rock. In case of a failure, the upper layer, a layer in between, or the entire soil column may fail.

The main interest of this analysis are to evaluate if the slope are stable or instable. Instability, according to the limit equilibrium analyses, occur when FoS ≤ 1. Therefore, the results are displayed as at the slope angle where FoS are ≤ 1 in Table 5.13. The table show the FoS for magnitude 7 events for all faults at 1km depth. Figure 5.24 display how the FoS decreases with increasing slope angle. The calculations in this plot is performed between 0.5° and 15° to better observe any changes at low angles. The FoS at 0° are extremely high values, and the FoS above a slope angle of 15° are almost identically for all layers.

From Table 5.13, it is observed that the upper layers requires a higher slope angle than layer 2 and 3. Layer 4 require a higher slope angle than layer 2, 3 and 5, and Layer 6 require a higher slope angle than layer 5.This indicates that Layer 5, 3 and 2 are the weakest layers, or that the ground motion/acceleration are greatest amplified here.

An unexpected result, is that all the faults display the same FoS results for all layer, for all depth and magnitudes. Because the faults are at different distances from the initiation area, it would have been expected that the closer fault would affect the slope stability more than the fault at larger distances. Because the results are exactly the same, only one plot of a magnitude 7 event at 1km depth at the Slettringen Ridge North fault are included.

Table 5.13: Slope angles where FoS ≤ 1 for magnitude 7 events at 1 km depth.

Fault	Layer 1	Layer 2	Layer 3	Layer 4	Layer 5	Layer 6
SRN	26.4°	14.9°	14.8°	16.8°	14°	17.4°
VG	26.4°	14.9°	14.8°	16.8°	14°	17.4°
OL	26.4°	14.9°	14.8°	16.8°	14°	17.4°
KFC	26.4°	14.9°	14.8°	16.8°	14°	17.4°
MTG	26.4°	14.9°	14.8°	16.8°	14°	17.4°

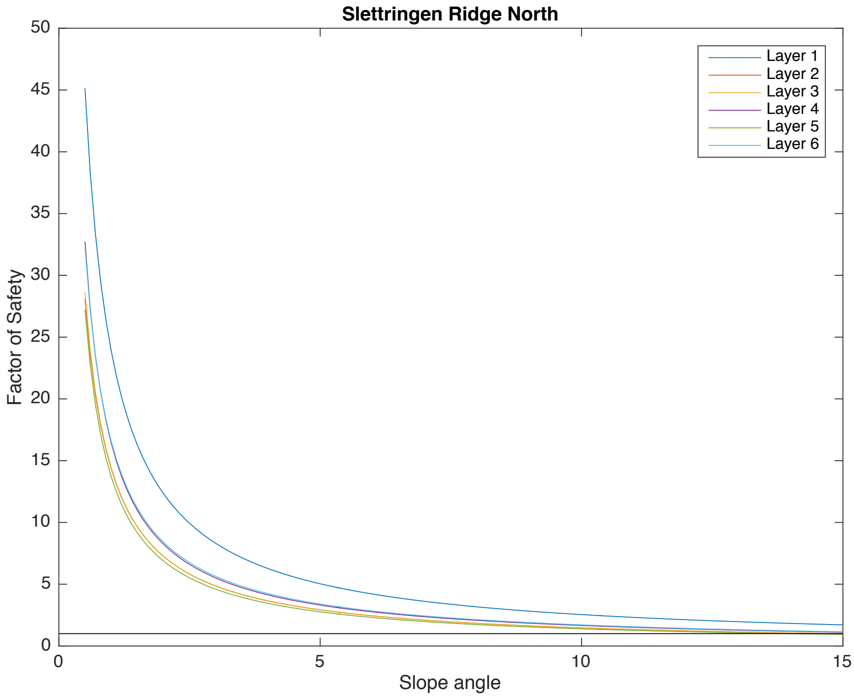

Figure 5.24: Plot of the Factor of Safety for layer 1 to layer 6. The black line represent FoS = 1. The angles are from 0.5 to 10° to better observe any difference.

5.5 Seismic-Induced Permanent Displacement

The equation developed by Travasarou and Bray (2003) has been applied to calculate the seismic-induced permanent displacement. Because this equation includes the spectral acceleration we can better observe the effect of amplification at low frequencies. The equation is dependent on critical acceleration, the spectral acceleration at $1.5S_a$ and magnitude. The critical acceleration are the same as calculated for the maximum distance. The spectral acceleration is obtained from the results of DEEPSOIL in the different layers. The results from EXSIM12 defined the spectral acceleration of bottom of layer 6. The critical acceleration will at one particular angle be negative, which will predict a permanent displacement equals to zero at high slope angles, which are reasonable to believe is not the case. The permanent calculation have therefore only been calculated for positive values of k_y, and the line for some of the layers ends, while some continues to increase. This is further discussed in Chapter 6.

The results presented in this section are from the same faults as in previously sections. Table 5.14 is a summary of the slopes angle at which critical displacement are observed for the different faults for a magnitude 7 event at 1km depth. For layer that does not present any value of slope angle, the critical displacement are located outside the range of 0° to 15°. The literature are vague on the finite distance/displacement required to initiate slide. Because no information of critical displacement are known, and the evaluation of this is beyond the scope of this thesis, it has been assumed that 100cm permanent displacement as used in ten Brink et al. (2009) and defined by e.g. Newmark (1965), could be used as a required displacement for slope failure. Even though the finite distance could be debated, this value have been adopted here as required displacement for failure because the slopes of interest are gentle and it is reasonable to assume that the displacement required to cause failure should be greater on gentle slopes than on steep slopes. As for the FoS, the displacement have been evaluated for the different layers, and it is reasonable to believe that a critical displacement in one layer, will also cause instability in the overlying layer.

The results from FoS showed no difference in magnitude, depth or distance for source to site. For the permanent displacement, analysis there are observed difference in the calculated displacement depending on distance from fault to size, magnitude and depth of fault. Figure 5.25 illustrates the the calculated permanent displacement for different magnitudes at the SRN fault at 1km depth. The highest predicted displacement at low slope angles are for a magnitude 7 event, and decrease with decreasing magnitude. At approximately 13° the permanent displacement appear to tend to infinity for all magnitudes.

Figure 5.26 and 5.27 illustrates the permanent displacement in layer 5 for different depths

Table 5.14: Critical angle for magnitude 7 events at 1 km depth. Some of the critical angles are outside the range of 0° to 15°, and are therefore not presented here.

Fault	Layer 1	Layer 2	Layer 3	Layer 4	Layer 5	Layer 6
SRN	-	12.9°	11.6°	13.9°	11.4°	14.9°
VG	-	12.7°	12.5°	14.5°	12°	-
OL	-	13.6°	13.3°	-	12.5°	-
KFC	-	13.8°	13.5°	-	12.2°	-
MTG	-	14°	13.7°	-	12.9°	-

for magnitude 7 events at the SRN and the MTG fault. For the SRN fault, the displacement reach critical displacement at 11.4° for 1km depth, and at 11.8° and 12.5° for 5km and 10km depth. For the MTG fault, both 1km and 10km depth reach critical displacement at 12.9°, while 13.2° for 5km depth.

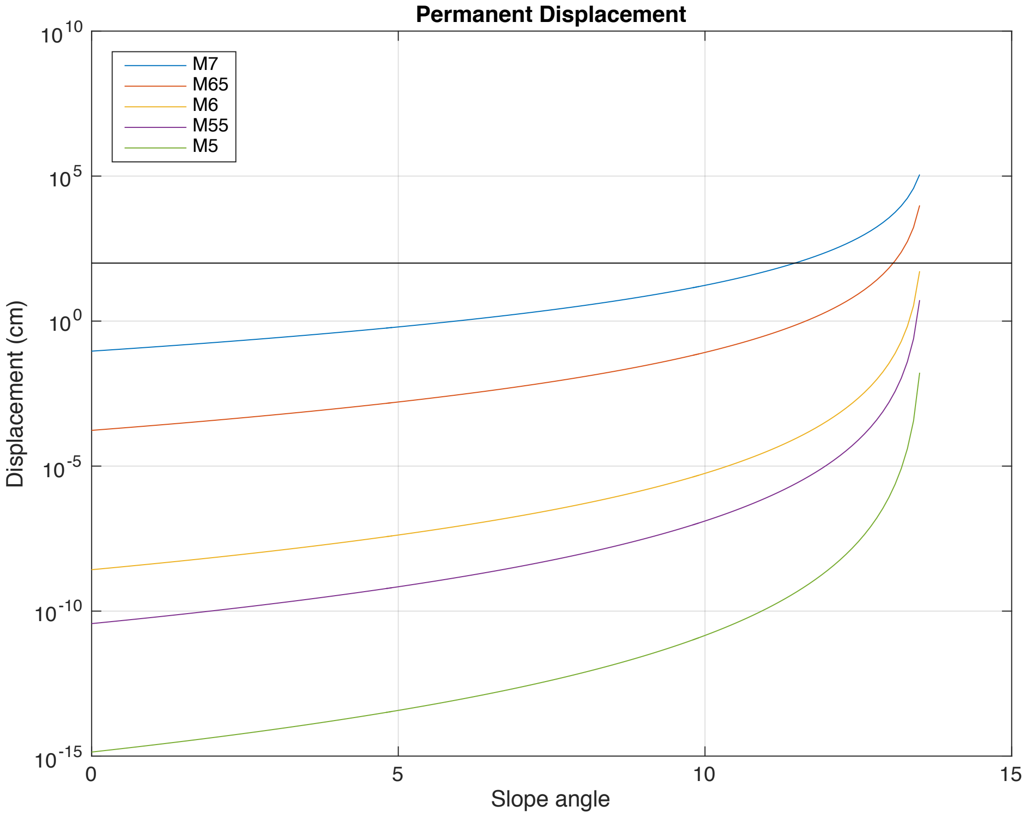

Figure 5.25: Plot displaying the calculated permanent displacement in layer 5 for different magnitudes at the SRN fault at 1km depth. The predicted permanent displacement increase with increasing magnitude, and increase with increasing slope angle. The black line represent critical displacement, defined as 100cm.

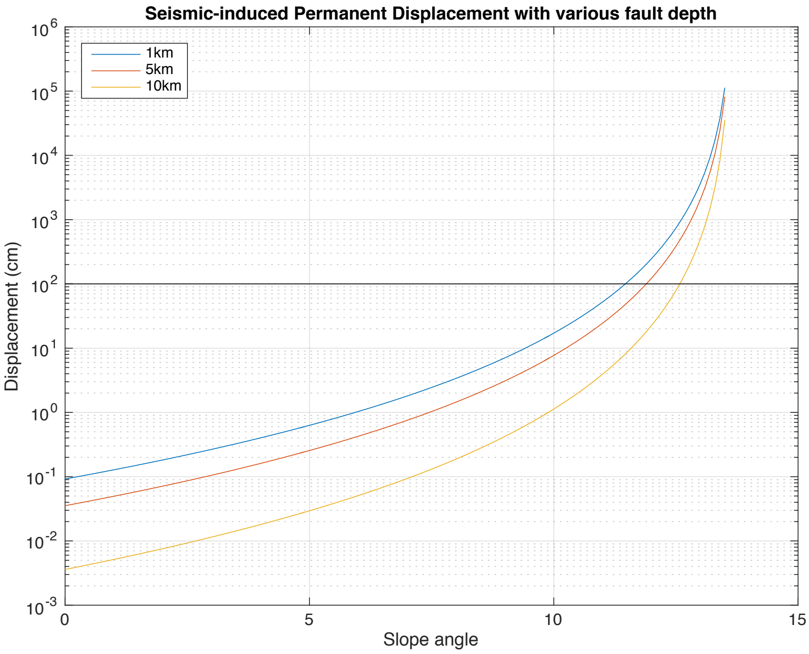

Figure 5.26: Plot displaying the calculated permanent displacement in layer 5 for different depths at the SRN fault. The permanent displacement increase with decreasing depth of fault. The black line represent critical displacement, defined as 100cm.

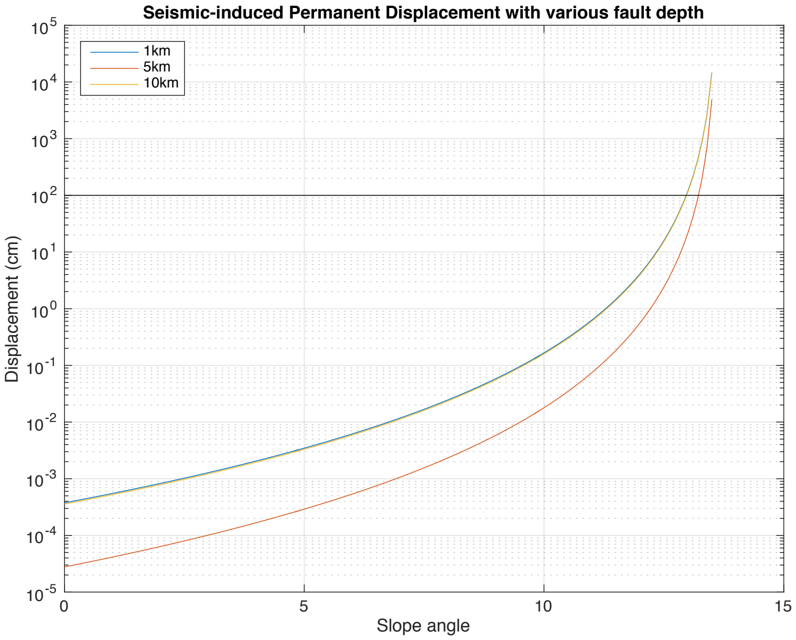

Figure 5.27: Plot displaying the calculated permanent displacement in layer 5 for different depths at the MTG fault. The permanent displacement varies less when comparing depths for the MTG fault, which is located at a greater distance from the initiation area than the SRN fault. The black line represent critical displacement, defined as 100cm.

5.5.1 Slettringen Ridge North

The SRN fault is located closest to the initiation area and are therefore assumed to be capable of having the largest effect on slope stability. The approximate distance from the SRN fault to the assumed initiation area is 45km. If we follow the definition of 100cm required displacement, we can observe that layer 5 reach the critical displacement first at 11.4°. Layer 3 reach the required displacement at 11.6°, and it is reasonable to believe that the difference between layer 5 and 3 are insignificantly, i.e. have the same potential. At low angles, the displacement are largest in layer 3 followed by layer 4. However, the displacement here are considered to be to small to affect the stability.

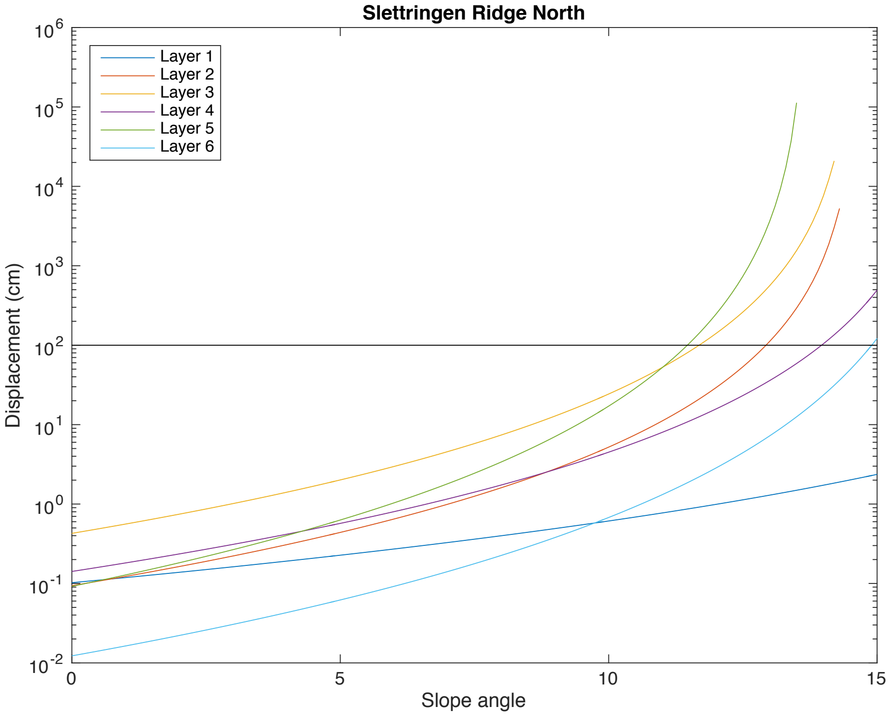

Figure 5.28: Plot of permanent displacement for SRN M7 1km depth. The black line represent critical displacement, defined as 100cm. Layer 5 reach the critical displacement at 11.4°. Layer 1 does not reach the critical displacement for the range of slope angles defined.

5.5.2 Vigra High - Grip High

The VG fault is located 80-90km from the assumed initiation area. In Figure 5.29 we can observe that layer 5 reaches the critical displacement at about 12°. Layer 3 and 2 are critical displaced at about 12.5° and 12.7°, which is considered as an insignificant difference. At 14.4° layer 4 reaches the critical displacement. Layer 1 and 6 does not exceed the critical displacement limit for the slope angles defined here. At lower angles, the largest predicted displacement is in layer 2 followed by layer 3 and 1. However, the low displacement predicted at lower angles are assumed not to be sufficient to cause failure.

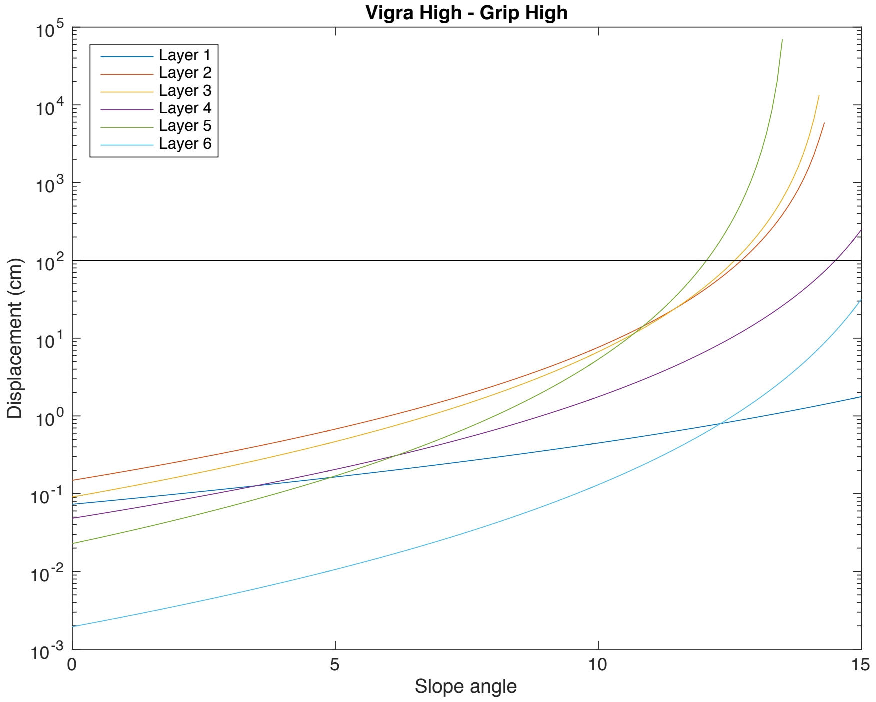

Figure 5.29: Plot of permanent displacement for VG M7 1km depth. The black line represent critical displacement, defined as 100cm. Layer 5 reach the critical displacement at 12°. Layer 1 and 6 does not reach the critical displacement for the range of slope angles defined.

5.5.3 Ormen Lange

The OL fault is located approximately 130km from failure area, and are well above the calculated maximum distance even for a magnitude 7 earthquake. Layer 5 reaches critical displacement at approximately 12.5°. Layer 3 and 2 are critical displaced at 13.2° and 13.6°. The remaining layers does not reach critical displacement for the slope angles defined. At low angles, the largest displacement are observed in layer 1, 2 and 3. The displacement at low angles are, however, considered insufficient to cause failure.

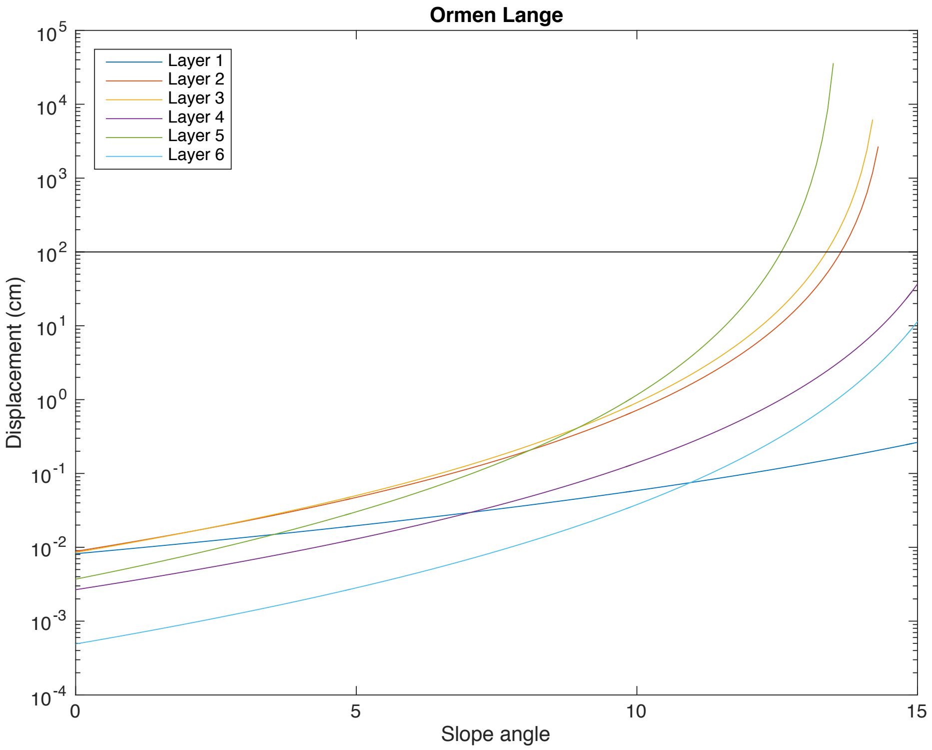

Figure 5.30: Plot of permanent displacement for OL M7 1km depth. The black line represent critical displacement, defined as 100cm. Layer 5 reach the critical displacement at 12.5°. Layer 1, 4 and 6 does not reach the critical displacement for the range of slope angles defined.

5.5.4 Klakk Fault Complex

The KFC fault is located 150-180km from failure area. At 12.2°, layer 5 are critical displaced. Layer 3 and 2 reaches the critical displacement limit at respectively 13.5° and 13.8°. Layer 1,4 and 6 are not critical displaced for the defined slope angles. An interesting observation, differs from the previous cases, are that layer 5 have the largest predicted displacement at all slope angles, followed by layer 3 and 2. Layer 5 and 6 predict approximately the same displacement for all defined slope angles.

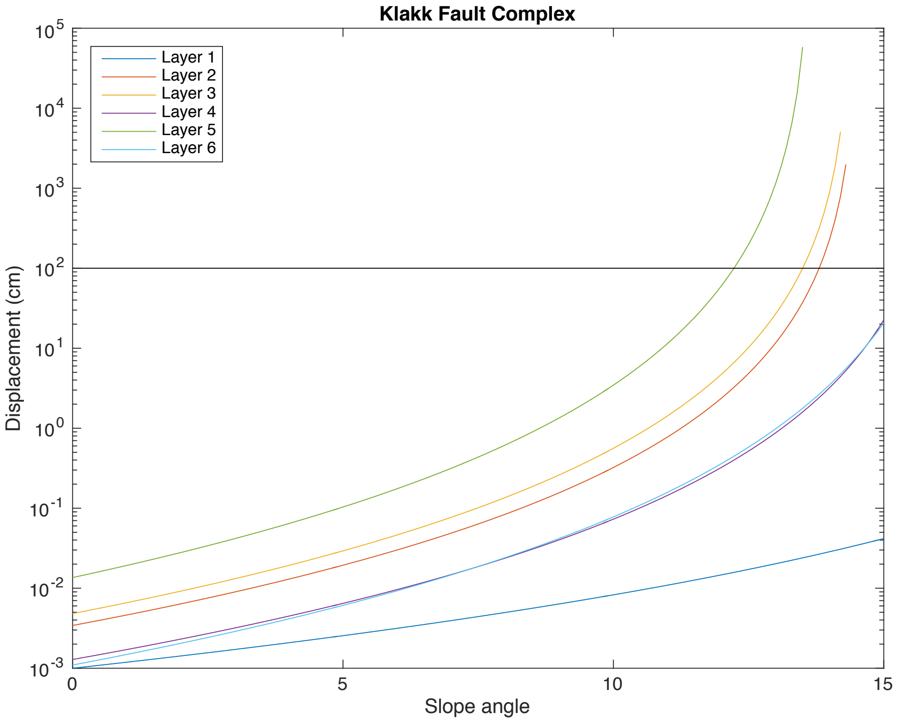

Figure 5.31: Plot of permanent displacement for KFC M7 1km depth. The black line represent critical displacement, defined as 100cm. Layer 5 reach the critical displacement at 12.2°. Layer 1, 4 and 6 does not reach the critical displacement for the range of slope angles defined.

5.5.5 Makrell Horst - Tampen Spur - Gnausen High

The MTG fault is located 210-230km from initiation area, and are the fault presented that is located furthest away from the initiation area. Because of the large distance, it is expected that an earthquake at this fault will have the least potential of triggering slope failure. Layer 5 predicts the critical displacement at 12.9°. Layer 3 and 2 are critical displaced at 13.7° and 14°, while layer 1, 4 and 6 does not predict any critical displacement within the defined slope angles. At low angles, layer 3 predicts highest displacement, but as for the other cases, this displacement is considered to be too small to cause failure.

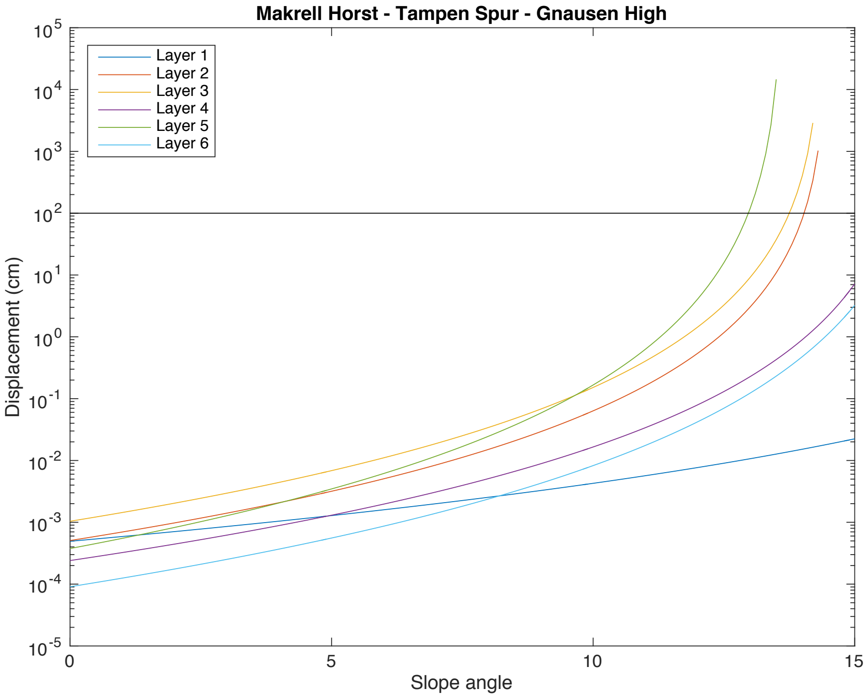

Figure 5.32: Plot of permanent displacement for MTG M7 1km depth. The black line represent critical displacement, defined as 100cm. Layer 5 reach the critical displacement at 12.9°. Layer 1, 4 and 6 does not reach the critical displacement for the range of slope angles defined.

Chapter 6

Discussion

This Chapter will start by a brief discussion of the maximum distance from fault to site. Followed by a discussion of the soil response analysis by equivalent linear and nonlinear approach. The results from the pseudo-static Factor of Safety and permanent displacement analysis will be discussed. An evaluation of earthquake as a triggering mechanism will be made based on the result presented in this thesis. Last, the uncertainties with the analysis will be discussed. The results concerning EXSIM12 will not be discussed here, and the reader are referred to Section 4.3 and to the master thesis' of Tveit (2013) and Johnsen (2015) for discussion of the input parameters and results.

The main objective of this study was to evaluate earthquakes as the responsible triggering mechanism for submarine mass failures. The results have been presented for a range of slope angles, but the most interesting part are low angles (0.5 to 2.3°). The preslide inclination of the slope is estimated to 0.6-0.7° in the middle slope and to 1-2° in the upper slope by Bryn et al. (2005). The main focus in this discussion will be on these low angles, but some comments on results at greater inclinations will also be given.

6.1 Maximum distance from fault to site

The maximum distance calculations indicate that the distance increase with higher magnitude and steeper slope. This was an expected result because with steeper slope angles the static shear stresses in the slope will increase (Biscontin and Pestana, 2006), and a higher magnitude yields a higher energy release. Because the energy from earthquakes attenuated with distance, it is reasonable to believe that a lower magnitude earthquake will not have potential to overcome the critical acceleration at a close enough distance. A larger magnitude earthquake will have larger amount of energy, that also could overcome the critical acceleration at a greater distance.

For slope angles over approximately 9-10° some strong variations was observed (Fig. 6.1

). This variations is due to the critical acceleration after a certain value of β will calculate negative value of K_y. For the calculation using Campbell (2003), the maximum distance drop to zero at 12° for a magnitude 7 event, some higher for the lower magnitudes. For the NGA-WEST2 (Shahjouei and Pezeshk, 2015), the maximum distance increase evenly, before a strong increase is observed around 9°, around 9.5° the distance drops to zero. No obvious reason for this "phenomena" was found in the literature. Because these variations is observed at higher angles, they have been interpreted to be due to the slope being so steep that no external trigger is required, and the slope may fail only due to gravitational effects.

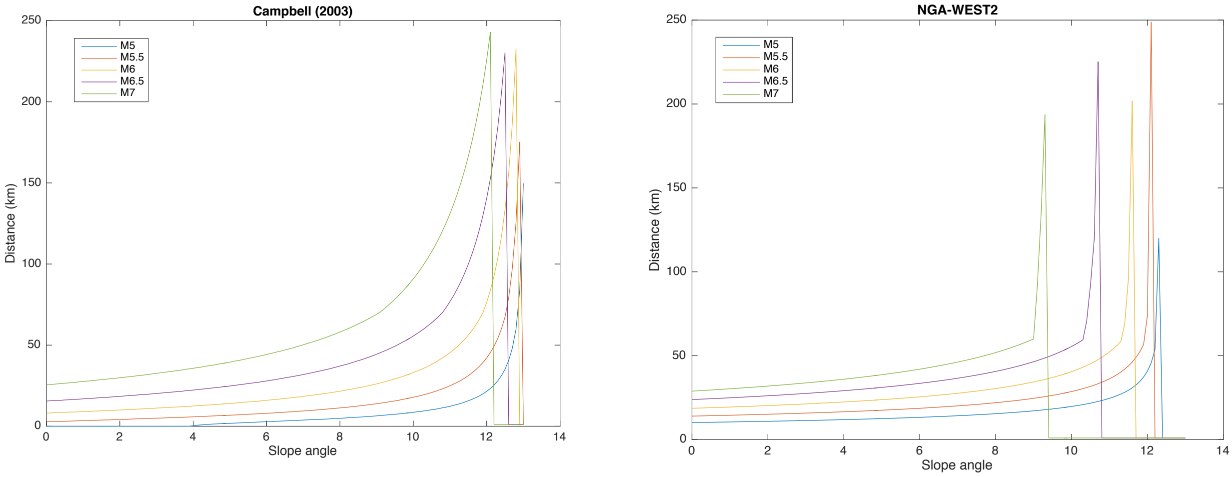

(a) Campbell (2003)

(b) NGA-WEST2

Figure 6.1: Plot displaying the variations in maximum distance observed at higher slope angles.

6.2 Comparison of the non-linear approach and the equivalent linear approach

The non-linear and equivalent linear approach has shown to predict different results at different periods. At short periods, the NL analysis predicts less amplification in the sediment compared to the input motion. This is in agreement with Rathje and Kottke (2011) which have explained this difference as a response to the incoherency (waves not in phase) in ground motion. The nonlinear stress-strain response cause this incoherency to occur in ground motion (Rathje and Kottke, 2011).

Kramer (1996) states that the incoherency response can be caused by e.g. traveling wave effect, extended source effect and ray-path effects. The traveling wave occur when the wavefront reach the surface at different times due to the waves not traveling vertical. The extended source effect occurs when there is produced a time shift due to differences in geometry of the source, e.g subfault N reach "receiver 2" before subfault N+1 reach "receiver 2". Scattering (reflection and refraction) of waves are caused by inhomogeneities along the travel paths of seismic waves, this is named the ray-path effect and can cause incoherency. Because assumptions such as vertically propagation SH-waves and horizontal layer boundaries are made for the 1D analysis (Kramer, 1996). The ray-path effect is probably the effect that causes incoherency in the NL-analysis because reflection and refractions will also occur at each layer boundary due to different properties.

At moderate periods the NL-approach predicts more amplification than the EQL-approach, this is also in agreement with Rathje and Kottke (2011). Rathje and Kottke (2011) explains this amplification in the NL-analysis to be caused by stress reversal caused by instantaneous change in soil stiffness. In the EQL-analysis, high frequencies can also be over-damped, which results in higher amplification prediction by the NL-analysis (Rathje and Kottke, 2011).

Close to the fundamental periods, the NL-analysis predicts more amplification than the EQL. Again, in agreement with Rathje and Kottke (2011), which explains this to be caused by the soil stiffness being changed continuously in the NL-analysis.

Because the PGA plots from DEEPSOIL uses the ground acceleration at high frequencies, the EQL approach will reveal higher acceleration values than the NL approach due to smaller incoherency of the seismic waves.

6.2.1 Equivalent Linear or Non-Linear analysis?

As described in the section above, NL and EQL predicts different amplification at different frequencies (or periods). The differences depend on the soil responses degree of nonlinearity. When larger strains are involved the non-linear approach should be used because it allows to incorporate the nonlinearity of the soil. At low strains, both of the analysis should predict acceptable results and can be applied (Kramer, 1996). Kaklamanos et al. (2013) found that the best indicators for when the different approaches should be used are the maximum shear strain, predominant S_a and the PGA. Their results are summarized in Figure 6.2.

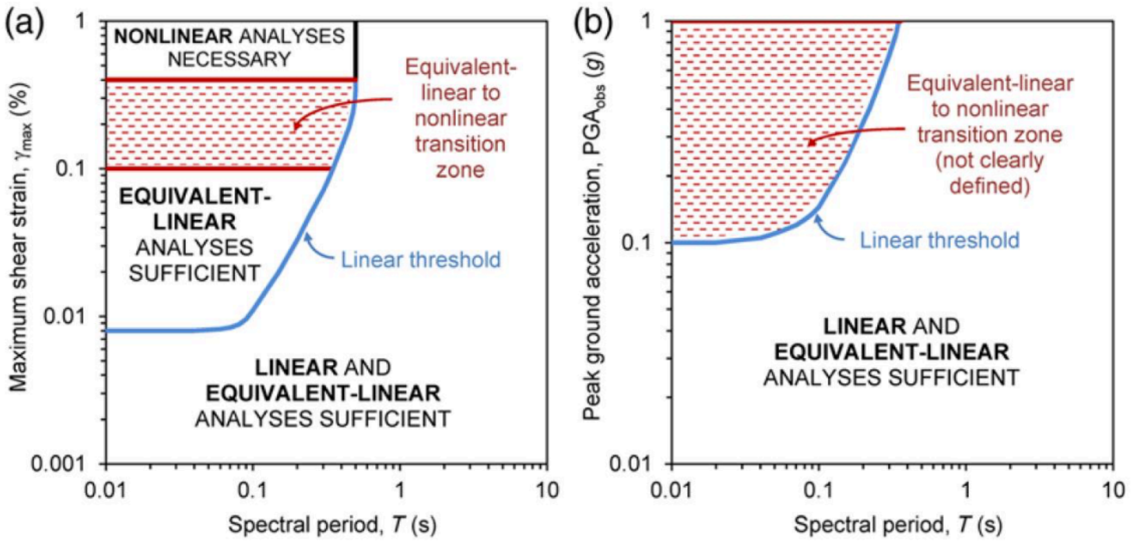

Figure 6.2: Figure presenting acceptable ranges for when EQL analysis are sufficient and for when the NL analysis should be used. From Kaklamanos et al. (2013).

A test to compare EQL and NL was performed by a permanent displacement analysis for a magnitude 7 event (1km depth) at the SRN fault (Fig. 6.3). The result from this test reveal almost the same results, and therefore indicate that small strains are involved and thus both the NL and EQL should predict reasonable results. This is also confirmed by Figure 6.8, where it is observed that the maximum shear strain does not exceed 0.5%.

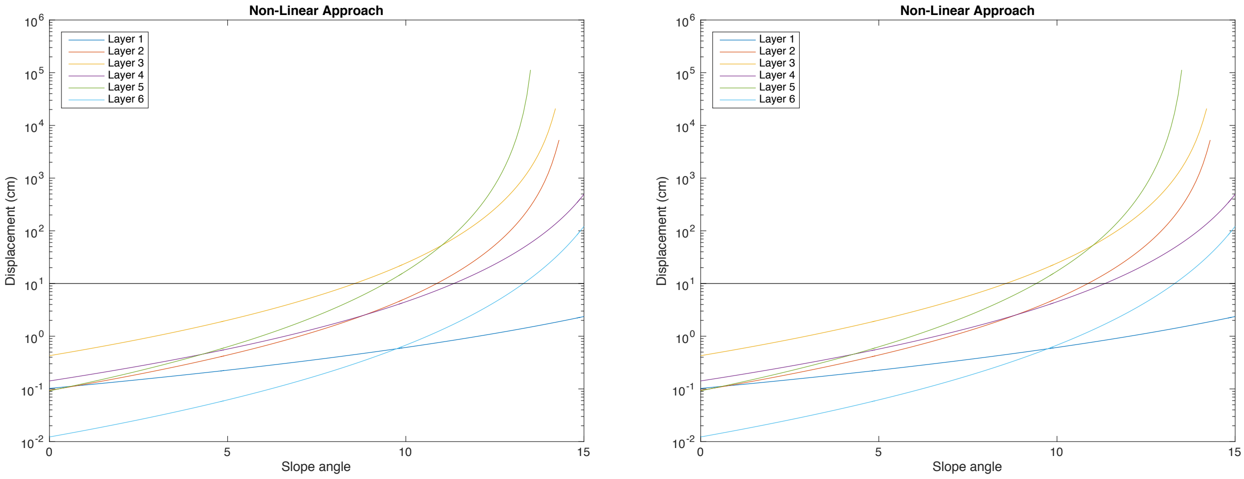

(a) Non-linear approach

(b) Equivalent linear approach

Figure 6.3: Figure displaying permanent displacement in the case of a magnitude 7 event at 1km depth at the SRN fault by the use of the NL- and the EQL approach.

The difference between the NL and the EQL approach is illustrated in Figure 6.4. The EQL approach predicts a slightly higher displacement than the NL. With increasing slope angle the difference increase. For low slope angles the difference is about 2%, while at higher slope angle the difference is as much as 40%. However, the actual difference (cm) in predicted displacement is so small that it is considered to be insignificant.

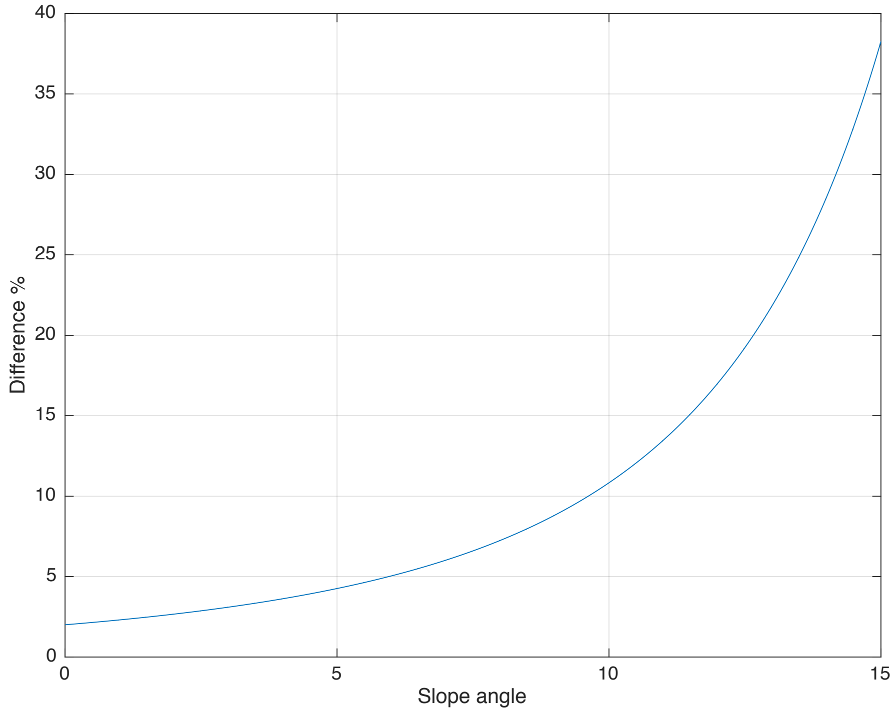

Figure 6.4: Difference between NL and EQL approach in percent with slope angle.

6.3 Pseudo-static Factor of Safety

In Section 5.4, different parameters effect on the Factor of Safety was tested. For these result it was observed that the shear strength of the soil has the greatest effect on the FoS, where a very low shear strength may cause slope instability at low slope angles. The acceleration and the unit weight was the parameters tested that had the smallest impact on FoS. FoS ≤ 1 for all acceleration values occurred at 10.5 -10.7°. The combination of a very high unit weight and low shear strength would probably be necessary in order to produce instability. However, this is not realistic as a high unit weight usually yields a small void ratio, and a small void ratio will usually result in a high shear strength (Oh et al., 2017; L'Heureux and Long, 2016).

After testing the effect of various parameters, the FoS for ground motion acceleration at base of each layer was computed. The result from this calculation was unexpected. The FoS are equal to or drops below 1 at one particular slope angle for each layer, independent of depth, magnitude and distance from initiation area. The parameter sensitivity test showed that the FoS probably are least sensitive to the acceleration. Because the faults are located in relatively close distances to each other, the variations in acceleration for the different faults are small. The PGA at base of the sediment profile only have a difference of 0.0486g from the fault located closest to the initiation area and the fault at greatest distance. The small differences in acceleration are thus probably the reason for the exactly same results. For all scenarios, layer 5 appears to be the layer most affected by earthquake acceleration. However, not before 14° the FoS are equal to or below 1, indicating that the slope are stable at low angles.

6.4 Seismic-Induced permanent displacement

This section will discuss the results from the permanent displacement analysis. Starting with discussion on tolerable displacement, followed by a discussion on the effects from the earthquakes at various distances.

6.4.1 Tolerable displacement

In order to evaluate how the seismic-induced permanent displacement affects the slope stability, one must consider the tolerable displacement for a slope. The tolerable (critical displacement) can be defined as a finite distance a slope can sustain without failing or become unstable. Jibson (1993) suggested that the tolerable displacement should be determined by evaluating the displacement together with the parameters of the slope material. Softer soils may be able to sustain displacements that are much larger than for brittle material (Abramson et al., 1996).

Ideally, there should be done research to find a tolerable finite permanent displacement that a slope can sustain. Because this is beyond the scope of this thesis, a displacement value of 100cm, first defined by Newmark (1965), have been adopted as the critical failure criteria.

There are suggested several levels of critical permanent displacement, these are listed by Abramson et al. (1996) as:

- Hynes-Griffin and Franklin (1984): 100cm permanent displacement for well-constructed dams
- Wieczorek et al. (1985): 5 cm permanent displacement in landslide hazard map of San Mateo County, California
- Keefer and Wilson (1989): 10 cm for coherent slides in southern California
- Jibson and Keefer (1993): 5 to 10cm for landslides in the Mississippi Valley

Carlton et al. (2016) studied the effect of sensitivity [1] on permanent displacement. If the sensitivity is high, the required shear stress for static stability may be higher than the mobilized shear strength during the earthquake. The calculation of permanent displacements will then tend to infinity, indicating that the slope has failed (Carlton et al., 2016). It has been shown that for most layers, the predicted displacement tends to infinity after 100cm of displacement, which are in agreement with Carlton et al. (2016), and may indicate failure.

6.4.2 Permanent displacement as a function of distance from fault

The permanent displacement has been calculated as a function of the slope angle, and has been shown to increase with increasing slope angle. This is in agreement with Carlton et al. (2016), which studied permanent displacement as a function of slope angle for various parameters.

Initially it was believed that the SRN fault had the greatest potential of triggering a slide because the fault is located closest to the initiation area. This is also shown to be the case for the permanent displacement. This is probably due to the energy from earthquakes not being attenuated as much as for the fault located at a larger distance. Figure 6.5 display the calculated permanent displacement for the five faults presented in section 5.5. At low angle the permanent displacement are largest for the SRN fault and smallest for the MTG fault, which would be expected because of the greater distance MTG is located. At approximately 13.5° the predicted displacement does not differ significantly. This is believed to be caused by the higher slope angle. At higher slope angle the effect of earthquake acceleration on slope stability is probably not the main triggering factor. Steeper slopes are believed not to require an external trigger, and the effect from gravitation is believed to be sufficient for failure to occur.

---

[1] Sensitivity is defined by Carlton et al. (2016) as "the ratio of peak shear strength to the residual strength."

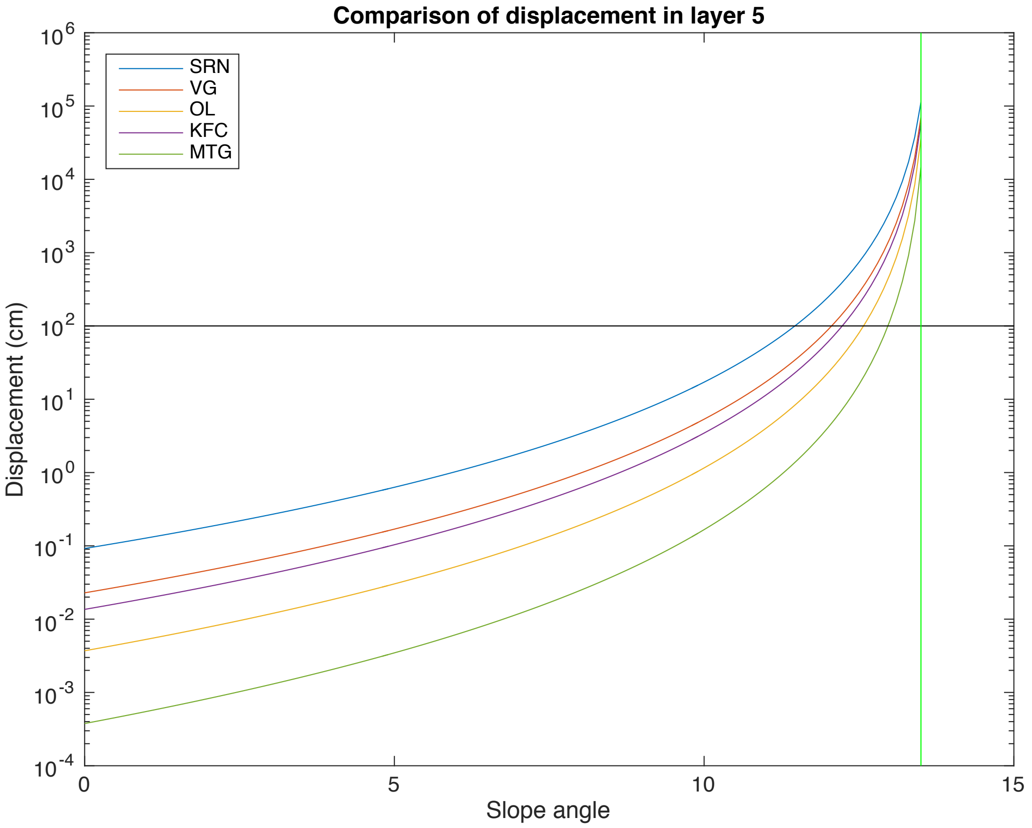

Figure 6.5: Permanent displacement for a magnitude 7 event at 1km depth for the five fault presented in Section 5.5. The horizontal black line represent the critical displacement (100cm) and the green vertical line represent the slope angle at where the displacement are approximately equal.

If the permanent displacement is considered together with the slope angle, it is found that small displacement occurred on gentle slopes, while large displacements occurred on steeper slopes. A small displacement on a gentle slope will probably not result in critical failure. While a large displacement at a great angle will most likely result in critical failure.

6.5 Earthquakes as a trigger for submarine mass failures

The result from the FoS calculations does not indicate that earthquakes in the study area could be responsible for triggering the Storegga slide. Only if the shear strength is very low, it would be indication of instability at low slope angles. The test indicated failure on low angle for constant parameters if the shear strength is as low as $100kPa$ and the acceleration $0.1g$ for a particular layer.

The permanent displacement analyses indicate failure ($>$ 100cm displacement) first at 14°. At low slope angles the permanent displacement are so low, that it is unlikely that a slide would be initiated. However, several factors, such are pore pressure build up, that can lead to failure is not considered in the analyses described in this study.

6.5.1 Critical acceleration

The critical acceleration, is the required acceleration in order to cause failure or affect the stability of slopes. This coefficient depends on the shear strength and the unit weight, and is a main key for the maximum distance calculation and also the seismic-induced permanent displacement calculation. The importance of this coefficient also causes it to be one of the greatest uncertainty in slope stabilities analyses because it represent the dynamic strength of the slope material.

6.5.2 Input motion

The accuracy of a seismic slope stability evaluation are highly dependent on the input motion. Because the seismic performance of a slope are dependent on several factors such as the magnitude, frequency content and duration, the choice of an accurate input motion are crucial (Kramer, 1996). In the following section, important aspects of the input ground motion are discussed.

Magnitude, distance and frequency content

From the results described in section 5.5, it is easily observed that higher magnitude predicts larger permanent displacement than lower magnitudes (Fig. 5.25). This was an expected result, and are probably because the higher magnitudes have a higher energy release than lower events. Because all faults are located at a distance of minimum 44km from the release area, it is reasonable to believe that this distance cause attenuation. E.g. Reiter (1991) describes attenuation as loss of seismic wave amplitude with distance. This attenuation is usually described to be a function of magnitude and distance, and consists of two main elements, geometrical spreading and absorption. Geometrical spreading are related to energy conservation due to increasing area as the waves propagates from the source. Absorption, also called damping, can be described as energy loss as the seismic waves propagates. Absorption are more complicated than geometrical spreading and are related to factors such as friction (across cracks and internal friction) and scattering of waves due to inhomogeneities of the material waves are traveling through (Reiter, 1991).

One interesting results, is that at larger distances, the critical displacement is reached or close to also for magnitude 6 events (however only slightly above or below), compared to above only for magnitude 6.5 and 7 events for events at a closer distance. For this to be explained, we have to consider the effect frequency content can have on seismic performance of a slope.

Smaller earthquakes often have a larger content of high frequency motion, while larger event have a higher content of low frequency motion and also a longer duration (Kramer, 1996; Reiter, 1991). Because high frequencies are filtered out, or attenuated and scattered, more rapid than low frequencies, and that low frequency motion can cause the lateral displacement to move nearly in phase, this may have a stronger effect on stability (Fig, 3.10) (e.g. Kramer, 1996; Reiter, 1991).

Duration

Earthquake damage are not only controlled by the magnitude, distance and frequency content, the duration of the event plays an important role as well. The number of loads or stress reversals during an earthquake affect many physical processes, e.g. degradation of stiffness and strength, and pore pressure build up. A motion with high amplitude that only last for a small period may produce less damage than a motion with low amplitude and long duration. The duration are dependent on the dimensions of the fault, because a larger fault takes longer time to rupture. This also cause the rupture to be magnitude dependent (Kramer, 1996).

This means that the time the acceleration of an earthquake exceeds the critical acceleration defined for a site, can greatly affect the slope stability. This has not been evaluated, but is however somewhat captured by the use of the degraded spectral acceleration in the permanent displacement calculations because it is magnitude dependent. Which also reveal that a larger magnitude produce a larger permanent displacement.

When discussing duration, the effect of directivity should also be mentioned. Because the hypocenter location is unknown, it was set to random with 10 iterations the modeling performed in EXSIM12. However, directivity can cause the duration to last longer or shorter. The directivity occurs because the rupture of the fault begin at one location and are moving in the direction of the fault. Figure 6.6, illustrates the effect of directivity. If the fault is rupturing towards receiver A the wave front are ”compressed” in that direction, and have a high frequency. This can cause constructive interference at receiver A which can cause a higher amplitude, but a shorter duration. At receiver B, the wave front are more spread with no constructive interference, this can result in a lower amplitude, but also a longer duration. However, a more random distribution of high frequencies may cause destructive interference and thus eliminate the effect of directivity (Reiter, 1991).

Because duration also can be affected by directivity, it would be of interest to investigate this effect. The directivity also affects the frequencies, thus if the rupture is propagating away from the initiation area, it could be expected a higher content of low frequency motion in the direction of initiation area. Since it has been shown that amplification are more prominent for low frequency motion, this should also be considered.

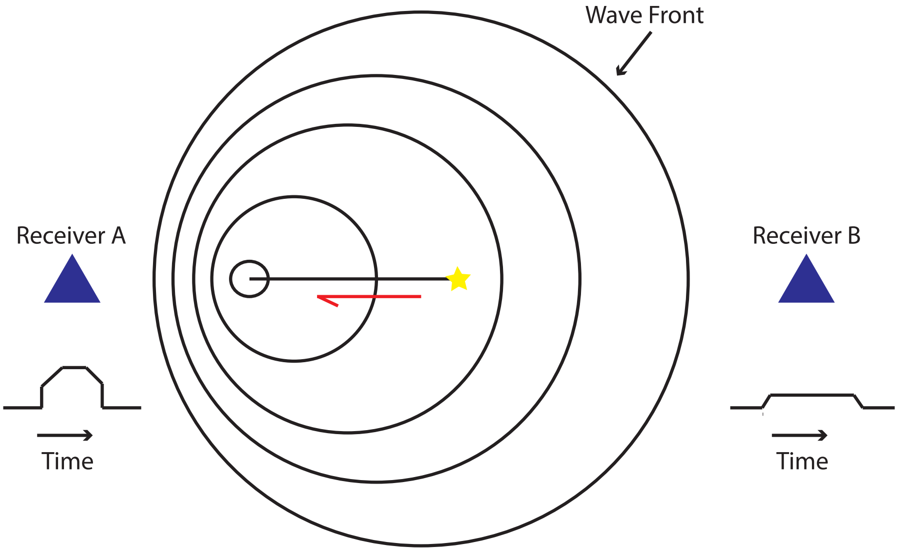

Figure 6.6: Effect of directivity on duration. Red arrow indicate rupture direction and yellow star represent the epicenter. At receiver A the duration is shorter, but the consists of higher frequencies. At receiver B the duration is longer, but consist of lower frequencies. Modified from Reiter (1991).

Depth of fault

The various depths of the fault does not appear to have a significant effect on slope stability. It would be expected that for the closer faults the depth of the fault would have a larger impact. The difference in slope angle for when the displacement reach critical displacement for 1, 5 and 10km at the SRN fault are only 1.1°. The small difference is probably because the calculations are more sensitive to the critical acceleration, which depends on the properties of the soil (e.g. shear strength), than on the actual acceleration.

The difference for the MTG fault even less than for the SRN fault. Both 1km and 10km depth reach critical displacement at 12.9°. The difference between 1km and 5km depth is only 0.3°. At larger distances, the distance waves are traveling becomes smaller compared to the depth (illustrated in Fig. 6.7), and the seismic waves are probably attenuated the same amount because the attenuation are dependent on e.g. distance.

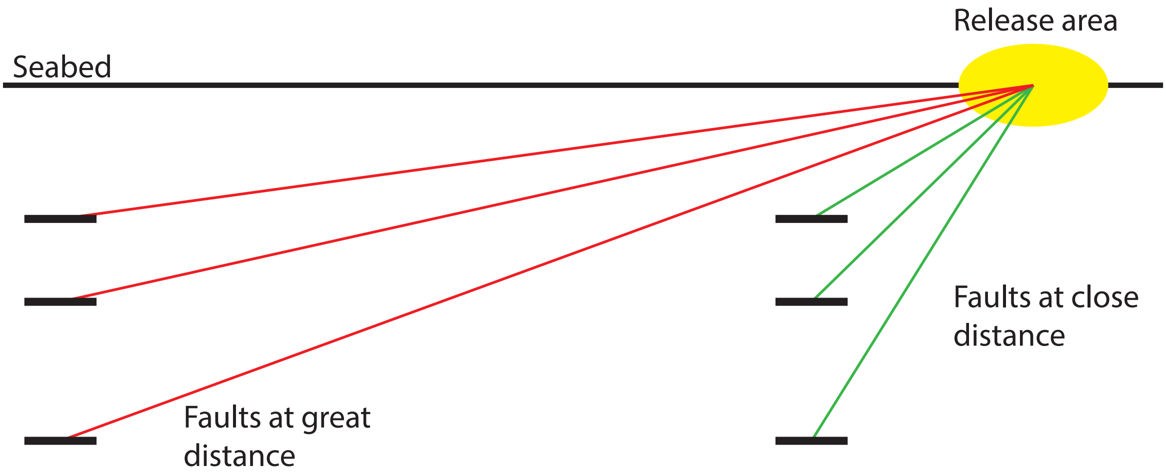

Figure 6.7: Illustration of the distance waves are traveling at fault located close and at greater distance to the release area. The difference in distance are more prominent for the fault located close.

6.5.3 Sediment properties and geometry

Fundamental frequency and thickness of soil mass

Another important factor are the fundamental period (or frequency) of the soil mass. As described earlier, is the ground motion from the earthquake resonate with the natural frequency of the soil, this may amplify the ground motion. The layers of the soil profile evaluated in this study have a relative long fundamental period, this also causes the greatest amplification of the seismic waves to occur at this period. Because high magnitude events often have a larger low frequency content, these may also cause the largest permanent displacement of the soil (Kramer, 1996).

The fundamental period can be estimated by the equation $T_s = 4z/V_s$ (e.g. Kramer, 1996; Bray, 2007), thus dependent on thickness of a layer. Layer 5 displayed the greatest displacement for all scenarios, and are also the thickest of the layers. The fundamental period of layer 5 will thus be long, making the layer more susceptible to permanent displacement for low frequency motion.

Shear strength of the sediments

As described in section 3.1, the critical acceleration is highly dependent on the shear strength (or dynamic shear strength) of the soil. Therefore the critical acceleration, combined with the input motion, are the greatest sources of uncertainty.

One of the arguments for using a 1D analysis, is that the stratigraphy of a continental slope often involves parallel layers with normal to lightly over consolidated layers (Talling et al., 2014), which also are distributed with relatively small changes in properties over great areas. For the Storegga area, it is assumed that the reason for the sliding process to end, was a strong over consolidated layer at the upper slope and that the graben structures formed by the sliding blocks acted as a stabilizer for further sliding (Gauer et al., 2005).

Because I have adapted a soil profile located to the side/north (Fig. 4.4) of the assumed initiation area, this may have been affected by various processes after the sliding event and may also have layers with local different properties than at the initiation area. There is a probability that the sliding event caused redistribution of excess pore pressure so that the shear strength today are different than it were at the time of the Storegga. Testing of the different parameters in section 5.4 revealed that slope stability was most affected by the shear strength of the soil, which then could possibly have a large impact on the slope stability analyses.

The shear strength of a soil can be defined after what "processes" that have affected the soil. As described above, a flat slope will not have any shear stresses developed, but when the ground is sloping, shear stresses are developed in the downslope direction. This can be referred to as the static shear strength, and depends on consolidation and void ratio etc. Cyclic shear strength, i.e. the strength of a soil under earthquake loading (or storm-waves), are thus a result of the static stress and the stress induced under cyclic loading (Kramer, 1996).

However, after an earthquake we can define strength as post-earthquake shear strength. The post-earthquake strength may be lower than the shear strength before cyclic loading. When a soil is subjected to cyclic loading, the structure of the soil may change causing a reduction in shear strength (Kramer, 1996).

In this study, the shear strength implemented in the analyses has not been tested under cyclic loading or after an earthquake (Leynaud et al., 2004). Because the cyclic strength and the post-earthquake may change, this will also be a source of uncertainties and should ideally be included in stability analyses. The pseudo-static equilibrium method, are however an "approximation" of the dynamic response of the soil. The critical acceleration (k_y) are derived from the pseudo-static method, and because k_y are included in the equation of seismic-induced permanent displacement, it is indirectly captured by this equation (Bray, 2007). Anyway, there should also be performed analyses to evaluate the post-earthquake strength to obtain a better knowledge of e.g. creep due to strength reduction that may occur after earthquake shaking (Nadim et al., 2007).

Pore pressure should also be included when evaluating the shear strength of a material (or soil) because generation of excess pore pressure can reduce the shear strength of the soil by decreasing the effective stress (Strout and Tjelta, 2005). Pore pressure generation has not been included in the soil response due to lack of information required, thus no comments on earthquake generated excess pore pressure can be given based on the result presented in this study. However, sources for generation of excess pore pressure in the Storegga area has been evaluated by e.g. Kvalstad et al. (2005a). Their study described earthquakes, rapid deposition and melting of gas hydrates as potential sources for excess pore pressure generation. Analysis of earthquake induced pore pressure generation did however not reveal large accumulation of strains and pore pressure, and they believed that the existence of excess pore pressure probably was preexisting due to e.g. rapid sediment loading or pore pressure transferred from the North Sea fan (Kvalstad et al., 2005a; Bryn et al., 2005).

Shear strain

For a submarine slope consisting of clay under an strong earthquake, the main deformation mechanism is the accumulation of shear strains in the down-slope direction. Simulation of seismic response on submarine slopes performed by Nadim et al. (2007) showed that the earthquake-induced cyclic shear strain of a clay slope rarely exceeds 0.5%, if the soil profile is near uniform. A strain-level below 0.5% are not likely to degrade the shear strength of a slope significantly. However, the simulations showed that permanent strain accumulation causes a rapid increase in earthquake-induced displacement at the seabed as slope angle increased (Nadim et al., 2007). As seen on Figure 6.8, non of the layers experience shear strain levels over 0.5%, making this scenario less likely. However, DEEPSOIL does not allow for modeling of earthquake-induced shear strain as a function of slope angle, thus the effects of slope inclination on shear strain has not been considered in this study.

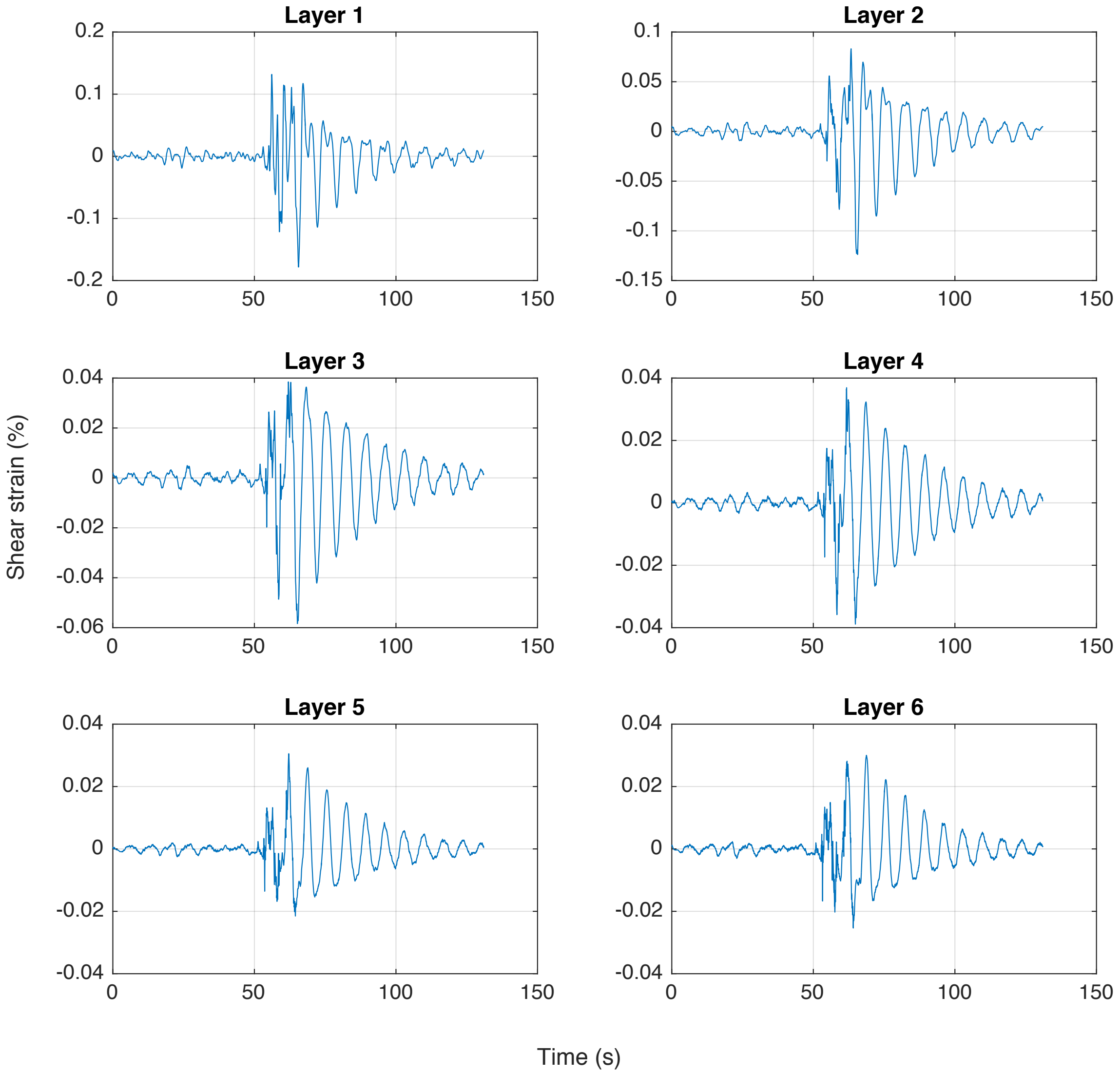

Figure 6.8: Time history of strain, resulting from a magnitude 7 event at 1km depth at the SRN fault. None of the layers have a strain rate above 0.5%, and is therefore considered as "small strain". Note that axis are not the same. Result are obtained from the soil response analysis in DEEPSOIL.

Slope angle

On the permanent displacement calculations, only small displacements are calculated for low angles. Thus indicate that earthquakes have a small to insignificant effect on the slope stability of gentle slopes.

It was observed that the permanent displacement increases as the slope angle increases. On a flat slope there are not generated shear stresses due to gravitational effects. As the slope angle increases, static shear stresses develops in the soil mass due to gravitation effect. When the soil mass is then subjected to an earthquake, this shear stress causes the displacement to accumulate downslope (Carlton et al., 2016).

6.6 Comparison with Biscontin et al. (2004), Biscontin and Pestana (2006) and Nadim et al. (2007)

Three scenarios for earthquake-induced submarine slides have been proposed by Biscontin et al. (2004); (1) failure during earthquake, (2) post-failure due to increase in pore pressure, and (3) post-failure due to creep. The three scenarios are closely linked.

For the first scenario, failure during earthquake, strong strain-softening [2] behavior of the soil and high sensitivity is required. The cyclic stresses generate strains and pore pressures that may degrade the shear strength of slope materials. The shear strength can degrade so much that the static shear stresses are not sufficient to prevent failure. However, large displacements downslope may occur without causing a complete failure (Nadim et al., 2007).

Loose sand and silts are most susceptible to liquefaction during earthquake shaking(Seed et al., 1983). The study area consist of clay or clayey sediments ($>30\%$ clay) and have a sensitivity in the order of 2.4 to 4.6 (considered low) (Leynaud et al., 2004), which usually does not liquefy during earthquake shaking (Seed et al., 1983). Earthquake shaking will then have a smaller potential to initiate slides in slopes containing clay, but can still cause permanent deformation and slumping downslope. The exception is clays with high sensitivity, usually having the characteristics of less than 15% clay, low plasticity and high water content (Nadim et al., 2007).

The second scenario is post-earthquake failure caused by excess pore pressure generated during and after the earthquake. Increase in excess pore pressure are caused by pore water migrating upwards as a result of earthquake shaking. The migration may not occur right after the earthquake, and a time delay of decades or centuries is possible. For this scenario to occur, a low permeable and low consolidated layer near the sea floor (5-10m) is required (Nadim et al., 2007).

Post-earthquake failure caused by reduction of static shear strength and/or creep is the last scenario. Large cyclic shear strain during the earthquake shaking is required for this scenario (Nadim et al., 2007). This scenario is similar to scenario 1. The main difference is that failure does not occur during the earthquake, but some time after due to degradation of shear strength caused by cyclic loading.

For the situation considered in this thesis, these scenarios are possible. However, ad-

---

[2] Strain-softening defined by Carlton et al. (2016) as ”the reduction of shear strength as the shear strain increases past the shear strain value where the peak shear strength occurs.”

ditional work considering strain-softening behavior and pore pressure generation would be required to obtain an indication of failure on low slope angles. Data available at the time of this study does not give enough information to perform additional analyses, thus no conclusion on the above scenarios can be given.

Chapter 7

Conclusion

7.1 Main conclusions

- Because of the small strain involved in the scenarios modeled, both the equivalent linear approach and the non-linear approach are appropriate applications in the analysis.

- The parameter sensitivity test revealed that the Factor of Safety (FoS) analysis is most sensitive to shear strength in addition to the unit weight, and least sensitive to earthquake acceleration.

- At low slope inclination, the FoS analysis revealed that slopes with the same material as given in Table 4.6, are very stable.

- Layer 5 (Table 4.6) appears to be the layer most affected by seismic loading.

- The seismic-induced permanent displacement analysis predicted small displacements at low slope inclination, indicating that seismic loading has little effect on slope stability at low slope angles.

- We do not know a finite distance the slope material should be displaced before catastrophic failure is initiated. If the displacement is lower than the critical displacement defined in this study, failure could be initiated on lower slope angles. However, a small displacement on a gentle slope will probably not result in catastrophic failure. In contrast, a large displacement at a great angle will most likely result in catastrophic failure.

- At low slope angles ($< 2^\circ$) earthquakes are probably not the main triggering mechanism for slope failure. Earthquakes may trigger a slide if the slope angle is steeper at one location. As a result failure may propagate upslope from where the earthquake has initiated failure.

- Earthquakes are not excluded as a triggering mechanism for slope failure on low slope angles, but there is a need to combine effects from earthquakes together with other possible preconditioned factors, such as excess pore pressure in the sediments.

7.2 Future work

- The ground motion prediction equations (GMPE) applied are derived for Eastern North America (ENA). Ideally, a GMPE derived for Norway should be applied.

- The shear strain predicted in this study does not consider slope angle. Because waves propagating in the slope plane could add additional shear stresses in the downslope direction (Carlton et al., 2016), the effect of slope angle should be considered.

- Information on the focal depth are sparse and was therefore set to 1, 5 and 10km. Seismic interpretation of faults in the area could give additional information on depths that could be incorporated in the modeling of ground motion. Another possibility is to evaluate hypocenter depths by recorded seismograms from the area to obtain an indication of focal depths.

- The sensitivity tests revealed that slope performance under seismic loading are most affected by the shear strength. Excess pore pressure in the sediments has been shown to decrease the shear strength and should therefore be taken into account. DEEPSOIL allows for pore pressure generation evaluation, but has not been performed due to lack of information on required parameters. PLAXIS is another program that can be applied for this problem, and allows both 2D and 3D modeling.

- The potential strain softening behavior (i.e. loss of strength due to cyclic loading)of the slope material has not been evaluated. However, this should included in seismic slope stability assessments because e.g. the Storegga slide deposits indicate a strain softening behavior (Kvalstad et al., 2005a). E.g. QUIVER, developed by Amir M. Kaynia at the Norwegian Geotechnical Institute, could be applied.

Bibliography

Abramson, L., Lee, T., Sharma, S., and Boyce, G. (1996). Slope stability and stabilization methods.

Ahrens, T. J. (1995). *Global earth physics: a handbook of physical constants*, volume 1. American Geophysical Union.

Amiranlou, H., Pourkermani, M., Dabiri, R., Qoreshi, M., Bouzari, S., et al. (2016). The stochastic finite-fault modeling based on a dynamic corner frequency simulating of strong ground motion for earthquake scenario of North Tabriz Fault. *Open Journal of Earthquake Research*, 5(02):114.

Atakan, K. and Ojeda, A. (2005). Stress transfer in the Storegga area, offshore mid-Norway. *Marine and petroleum geology*, 22(1):161–170.

Atkinson, G. M. and Assatourians, K. (2015). Implementation and validation of EXSIM (a stochastic finite-fault ground-motion simulation algorithm) on the SCEC broadband platform. *Seismological Research Letters*, 86(1):48–60.

Atkinson, G. M., Assatourians, K., Boore, D. M., Campbell, K., and Motazedian, D. (2009). A guide to differences between stochastic point-source and stochastic finite-fault simulations. *Bulletin of the Seismological Society of America*, 99(6):3192–3201.

Bellwald, Benjamin, and University of Bergen (2016). Slides in glacigenic settings - from fjords to deep sea.

Beresnev, I. A. and Atkinson, G. M. (1998). FINSIM- a FORTRAN program for simulating stochastic acceleration time histories from finite faults. *Seismological Research Letters*, 69(1):27–32.

Berg, K., Solheim, A., and Bryn, P. (2005). The Pleistocene to recent geological development of the Ormen Lange area. *Marine and Petroleum Geology*, 22(1):45–56.

Biscontin, G. and Pestana, J. (2006). Factors affecting seismic response of submarine slopes. *Natural Hazards and Earth System Science*, 6(1):97–107.

Biscontin, G., Pestana, J., and Nadim, F. (2004). Seismic triggering of submarine slides in soft cohesive soil deposits. *Marine Geology*, 203(3):341–354.

Biscontin, G. and Pestana, J. M. (2003). Seismic response of submarine slopes. In *ASME 2003 22nd International Conference on Offshore Mechanics and Arctic Engineering*, pages 867–874. American Society of Mechanical Engineers.

Blystad, P., Brekke, H., Færseth, R., Larsen, B., Skogseid, J., and Tørudbakken, B. (1995). Structural elements of the Norwegian continental shelf Part II: The Norwegian sea region: Plate i: NPD-Bulletin, 8.

Bondevik, S., Mangerud, J., Dawson, S., Dawson, A., and Lohne, Ø. (2003). Record-breaking height for 8000-year-old tsunami in the North Atlantic. *EOS, Transactions American Geophysical Union*, 84(31):289–293.

Boore, D. M. (2003). Simulation of ground motion using the stochastic method. In *Seismic Motion, Lithospheric Structures, Earthquake and Volcanic Sources: The Keiiti Aki Volume*, pages 635–676. Springer.

Boore, D. M. (2009). Comparing stochastic point-source and finite-source ground-motion simulations: SMSIM and EXSIM. *Bulletin of the Seismological Society of America*, 99(6):3202–3216.

Boore, D. M. and Joyner, W. B. (1997). Site amplifications for generic rock sites. *Bulletin of the seismological society of America*, 87(2):327–341.

Bray, J. D. (2007). Simplified seismic slope displacement procedures. In *Earthquake geotechnical engineering*, pages 327–353. Springer.

Brekke, H. et al. (2000). The tectonic evolution of the Norwegian Sea continental margin, with emphasis on the Vøring and Møre basins. *Special Publication-Geological Society of London*, 167:327–378.

Bryn, P., Berg, K., Forsberg, C. F., Solheim, A., and Kvalstad, T. J. (2005). Explaining the Storegga slide. *Marine and Petroleum Geology*, 22(1):11–19.

Bryn, P., Solheim, A., Berg, K., Lien, R., Forsberg, C., Haflidason, H., Ottesen, D., and Rise, L. (2003). The Storegga Slide complex; repeated large scale sliding in response to climatic cyclicity. *Submarine mass movements and their consequences: 1th international symposium*, pages 215–222.

Bungum, H. and Lindholm, C. (1997). Seismo-and neotectonics in Finnmark, Kola and the southern Barents Sea, part 2: Seismological analysis and seismotectonics. *Tectonophysics*, 270(1):15–28.

Bungum, H., Lindholm, C., and Faleide, J. (2005). Postglacial seismicity offshore mid-Norway with emphasis on spatio-temporal–magnitudal variations. *Marine and Petroleum Geology*, 22(1):137–148.

Byrkjeland, U., Bungum, H., and Eldholm, O. (2000). Seismotectonics of the Norwegian continental margin. *Journal of Geophysical Research: Solid Earth*, 105(B3):6221–6236.

Campbell, K. W. (2003). Prediction of strong ground motion using the hybrid empirical method and its use in the development of ground-motion (attenuation) relations in eastern North America. *Bulletin of the Seismological Society of America*, 93(3):1012–1033.

Carlton, B., Kaynia, A. M., and Nadim, F. (2016). Some important considerations in analysis of earthquake-induced landslides. *Geoenvironmental Disasters*, 3(1):11.

Chakraborty, A. and Goswami, D. (2016). State of the art: Three Dimensional (3D) Slope-Stability Analysis. *International Journal of Geotechnical Engineering*, 10(5):493–498.

Darendeli, M. B. (2001). Development of a new family of normalized modulus reduction and material damping curves.

Douglas, J. (2003). Earthquake ground motion estimation using strong-motion records: a review of equations for the estimation of peak ground acceleration and response spectral ordinates. *Earth-Science Reviews*, 61(1):43–104.

Engelder, T. and Price, N. (1993). Stress Regimes in the Lithosphere. *Engineering Geology*, 36(3):311–311.

Evans, D., King, E., Kenyon, N., Brett, C., and Wallis, D. (1996). Evidence for long-term instability in the Storegga Slide region off western Norway. *Marine Geology*, 130(3-4):281–292.

Faleide, J. I., Bjørlykke, K., and Gabrielsen, R. H. (2010). Geology of the Norwegian Continental Shelf. In Børlykke, K., editor, *Petroleum Geoscience: From Sedimentary Environments to Rock Physics*, pages 467–499. Springer.

Fejerskov, M. and Lindholm, C. (2000). Crustal stress in and around Norway: an evaluation of stress-generating mechanisms. *Geological Society, London, Special Publications*, 167(1):451–467.

Fjeldskaar, W., Lindholm, C., Dehls, J. F., and Fjeldskaar, I. (2000). Postglacial uplift, neotectonics and seismicity in Fennoscandia. *Quaternary Science Reviews*, 19(14):1413–1422.

Fossen, H., Dallmann, W., Andersen, and B., T. (2007a). Fjellkjeden går til grunne: Kaledonidene brytes ned; 405-359Ma. In Ramberg, I. B., Bryhni, I., and Nøttvedt, A., editors, *Landet blir til*, pages 178–258. Norsk geologisk forening.

Fossen, H., Pedersen, R.-B., Bergh, S., and Andresen, A. (2007b). En fjellkjede blir til: Oppbygningen av kaldonidene; ca. 500-405Ma. In Ramberg, I. B., Bryhni, I., and Nøttvedt, A., editors, *Landet blir til*, pages 178–258. Norsk geologisk forening.

Gauer, P., Kvalstad, T. J., Forsberg, C. F., Bryn, P., and Berg, K. (2005). The last phase of the Storegga slide: simulation of retrogressive slide dynamics and comparison with slide-scar morphology. *Marine and Petroleum Geology*, 22(1):171–178.

Groholski, D., Hashash, Y., Musgrove, M., Harmon, J., and Kim, B. (2015). Evaluation of 1-D non-linear site response analysis using a general quadratic/hyperbolic strength-controlled constitutive model. In *6ICEGE: 6th International Conf. on Earthquake Geotechnical Engineering.*

Haflidason, H., Lien, R., Sejrup, H. P., Forsberg, C. F., and Bryn, P. (2005). The dating and morphometry of the Storegga slide. *Marine and Petroleum Geology*, 22(1):123–136.

Haflidason, H., Sejrup, H. P., Nygård, A., Mienert, J., Bryn, P., Lien, R., Forsberg, C. F., Berg, K., and Masson, D. (2004). The Storegga Slide: architecture, geometry and slide development. *Marine geology*, 213(1):201–234.

Hashash, Y., Musgrove, M., Harmon, J., Groholski, D., Phillips, C., and Park, D. (2015). Deepsoil 6.1, user manual. *Board of Trustees of University of Illinois at Urbana-Champaign, Urbana.*

Hashash, Y., Phillips, C., and Groholski, D. R. (2010). Recent advances in non-linear site response analysis. *International Conferences on Recent Advances in Geotechnical Earthquake Engineering and Soil Dynamics*, 8.

Heezen, B. C. and Ewing, M. (1952). Turbidity currents and submarine slumps, and the 1929 Grand Banks earthquake. *American journal of Science*, 250(12):849–873.

Hjelstuen, B. O., Sejrup, H. P., Haflidason, H., Nygård, A., Ceramicola, S., and Bryn, P. (2005). Late Cenozoic glacial history and evolution of the Storegga Slide area and adjacent slide flank regions, Norwegian continental margin. *Marine and Petroleum Geology*, 22(1):57–69.

Huvenne, V. A., Georgiopoulou, A., Chaumillon, L., Iacono, C. L., and Wynn, R. B. (2016). Novel method to map the morphology of submarine landslide headwall scarps using Remotely Operated Vehicles. In *Submarine Mass Movements and Their Consequences: 7th international symposium*, pages 135–144. Springer.

Hynes-Griffin, M. E. and Franklin, A. G. (1984). Rationalizing the seismic coefficient method. Technical report, Army engineer waterways experiment station Vicksburg MS geotechnical lab.

Jibson, R. W. (1993). Predicting earthquake-induced landslide displacements using Newmark's sliding block analysis. *Transportation research record*, (1411).

Jibson, R. W. (2007). Regression models for estimating coseismic landslide displacement. *Engineering geology*, 91(2):209–218.

Jibson, R. W. and Keefer, D. K. (1993). Analysis of the seismic origin of landslides: examples from the New Madrid seismic zone. *Geological Society of America Bulletin*, 105(4):521–536.

Johnsen, M. (2015). Seismic hazard in Norway due to large earthquakes. *Department of Earth Science. UiB. Master thesis.*

Kaklamanos, J., Baise, L. G., and Boore, D. M. (2011). Estimating unknown input parameters when implementing the NGA ground-motion prediction equations in engineering practice. *Earthquake Spectra*, 27(4):1219–1235.

Kaklamanos, J., Bradley, B. A., Thompson, E. M., and Baise, L. G. (2013). Critical parameters affecting bias and variability in site-response analyses using KiK-net downhole array data. *Bulletin of the Seismological Society of America*, 103(3):1733–1749.

Keefer, D. K. (1984). Landslides caused by earthquakes. *Geological Society of America Bulletin*, 95(4):406–421.

Keefer, D. K. and Wilson, R. (1989). Predicting earthquake-induced landslides, with emphasis on arid and semi-arid environments. *Landslides in a semi-arid environment*, 2(Part 1):118–149.

Kramer, S. L. (1996). Geotechnical Earthquake Engineering Prentice Hall. *New York.*

Kvalstad, T. (2014). Undersjøiske skred. In Hoeg, Kaare, K. K. and Lied, K., editors, *Skred - skredfare og sikringstiltak, praktiske erfaringer og teoretiske prinsipper*, chapter 6, pages 123–137. Universitetsforlaget.

Kvalstad, T. J., Andresen, L., Forsberg, C. F., Berg, K., Bryn, P., and Wangen, M. (2005a). The Storegga slide: evaluation of triggering sources and slide mechanics. *Marine and Petroleum Geology*, 22(1):245–256.

Kvalstad, T. J., Nadim, F., Kaynia, A. M., Mokkelbost, K. H., and Bryn, P. (2005b). Soil conditions and slope stability in the Ormen Lange area. *Marine and Petroleum Geology*, 22(1):299–310.

Lamarche, G., Mountjoy, J., Bull, S., Hubble, T., Krastel, S., Lane, E., Micallef, A., Moscardelli, L., Mueller, C., Pecher, I., et al. (2016). Submarine Mass Movements and Their Consequences: Progress and Challenges. In *Submarine Mass Movements and their Consequences: 7th international symposium*, pages 1–12. Springer.

Leynaud, D., Mienert, J., and Nadim, F. (2004). Slope stability assessment of the Helland Hansen area offshore the mid-Norwegian margin. *Marine Geology*, 213(1):457–480.

L'Heureux, J.-S. and Long, M. (2016). Correlations between shear wave velocity and geotechnical parameters in Norwegian clays. In *Proceedings of the 17th Nordic Geotechnical Meeting.*

Lindholm, C., Roth, M., Bungum, H., and Faleide, J. (2005). Probabilistic and deterministic seismic hazard results and influence of the sedimentary Møre basin, NE atlantic. *Marine and petroleum geology*, 22(1):149–160.

Lindholm, C. D., Bungum, H., Hicks, E., and Villagran, M. (2000). Crustal stress and tectonics in Norwegian regions determined from earthquake focal mechanisms. *Geological Society, London, Special Publications*, 167(1):429–439.

Locat, J., Leroueil, S., Locat, A., and Lee, H. (2014). Weak layers: their definition and classification from a geotechnical perspective. In *Submarine mass movements and their consequences: 6th international symposium*, pages 3–12. Springer.

Lundin, E. and Doré, A. (1997). A tectonic model for the Norwegian passive margin with implications for the NE Atlantic: Early Cretaceous to break-up. *Journal of the Geological Society*, 154(3):545–550.

Lutro, Torunn (2011). Local site effects in Izmir, Turkey: Combining empirical and analytical approaches. *Department of Earth Science. UiB. Master thesis.*

Makdisi, F. and Seed, H. (1978). Simplified procedure for estimating dam and embarkment earthquake-induced deformation. *Journal of Geotechnical Engineering*, 104(7):849–867.

Martinsen, O. and Nøttvedt, A. (2007). Av hav stiger landet: Paleogen og neogen (kenozoikum), kontinentene av i dag formes; 66-2.7Ma. In Ramberg, I. B., Bryhni, I., and Nøttvedt, A., editors, *Landet blir til*, pages 440–477. Norsk geologisk forening.

Motazedian, D. and Atkinson, G. M. (2005). Stochastic finite-fault modeling based on a dynamic corner frequency. *Bulletin of the Seismological Society of America*, 95(3):995–1010.

Nadim, F., Biscontin, G., Kaynia, A. M., et al. (2007). Seismic triggering of submarine slides. In *Offshore technology conference*. Offshore Technology Conference.

Nadim, F., Kvalstad, T. J., and Guttormsen, T. (2005). Quantification of risks associated with seabed instability at Ormen Lange. *Marine and Petroleum Geology*, 22(1):311–318.

Newmark, N. M. (1965). Effects of earthquakes on dams and embankments. *Geotechnique*, 15(2):139–160.

Nøttvedt, A. and Johannessen, E. P. (2007). Grunnlaget for Norges oljerikdom: Sein jura, et øyhav vokser fram; 161-146Ma. In Ramberg, I. B., Bryhni, I., and Nøttvedt, A., editors, *Landet blir til*, pages 382–413. Norsk geologisk forening.

Nøttvedt, A. and Worsley, D. (2007). Vidstrakte sletter, kull og salt: Karbon og Perm i nord; 559-251Ma. In Ramberg, I. B., Bryhni, I., and Nøttvedt, A., editors, *Landet blir til*, pages 258–283. Norsk geologisk forening.

Nygård, A., Sejrup, H. P., Haflidason, H., and Bryn, P. (2005). The glacial North Sea Fan, southern Norwegian Margin: architecture and evolution from the upper continental slope to the deep-sea basin. *Marine and Petroleum Geology*, 22(1):71–84.

Oh, T.-M., Bang, E.-S., Cho, G.-C., and Park, E.-S. (2017). Estimation of undrained shear strength for saturated clay using shear wave velocity. *Marine Georesources & Geotechnology*, 35(2):236–244.

Olesen, O., Bungum, H., Dehls, J., Lindholm, C., Pascal, C., and Roberts, D. (2013). Neotectonics, seismicity and contemporary stress field in Norway–mechanisms and implications. *Quaternary Geology of Norway, Geological Survey of Norway Special Publication*, 13:145–174.

Ordonez, G. A. (2012). SHAKE2000- A computer program for the 1D analysis of geotechnical earthquake engineering problems.

Ottesen, D., Rise, L., Andersen, E. S., Bugge, T., and Eidvin, T. (2009). Geological evolution of the Norwegian continental shelf between 61°N and 68°N during the last 3 million years. *Norwegian Journal of Geology*, 89:251–265.

Park, D. and Hashash, Y. M. (2004). Soil damping formulation in nonlinear time domain site response analysis. *Journal of Earthquake Engineering*, 8(02):249–274.

Phillips, C. and Hashash, Y. M. (2009). Damping formulation for nonlinear 1d site response analyses. *Soil Dynamics and Earthquake Engineering*, 29(7):1143–1158.

Rathje, E. and Kottke, A. (2011). Relative differences between equivalent linear and nonlinear site response methods. In *5th International conference on earthquake geotechnical engineering, Santiago, Chile.*

Rathje, E. M. and Bray, J. D. (2000). Nonlinear coupled seismic sliding analysis of earth structures. *Journal of Geotechnical and Geoenvironmental Engineering*, 126(11):1002–1014.

Rathje, E. M. and Bray, J. D. (2001). One-and two-dimensional seismic analysis of solid-waste landfills. *Canadian Geotechnical Journal*, 38(4):850–862.

Rathje, E. M. and Saygili, G. (2009). Probabilistic assessment of earthquake-induced sliding displacements of natural slopes. *Bulletin of the New Zealand Society for Earthquake Engineering*, 42(1):18.

Reiter, L. (1991). *Earthquake hazard analysis: issues and insights*. Columbia University Press.

Rise, L., Ottesen, D., Berg, K., and Lundin, E. (2005). Large-scale development of the mid-Norwegian margin during the last 3 million years. *Marine and Petroleum Geology*, 22(1):33–44.

Roberts, D. (2003). The Scandinavian Caledonides: event chronology, palaeogeographic settings and likely modern analogues. *Tectonophysics*, 365(1):283–299.

Schnabel, P., Lysmer, J., and Seed, H. B. (1972). Shake. *A Computer Program for Earthquake Response Analysis of Horizontally Layered Sites, College of Engineering, University of Berkeley, CA. Rep., No. EERC*, pages 72–12.

Seed, H. B., Idriss, I., and Arango, I. (1983). Evaluation of liquefaction potential using field performance data. *Journal of Geotechnical Engineering*, 109(3):458–482.

Shahjouei, A. and Pezeshk, S. (2015). Hybrid empirical ground-motion model for central and eastern North America using hybrid broadband simulations and NGA-West2 GMPES. *NGA-East: Median Ground-Motion Models for the Central and Eastern North America Region, PEER Report Number 2015*, 4.

Solheim, A., Berg, K., Forsberg, C., and Bryn, P. (2005). The Storegga Slide complex: repetitive large scale sliding with similar cause and development. *Marine and Petroleum Geology*, 22(1):97–107.

Solheim, A., Forsberg, C., Yang, S., Kvalstad, T., Longva, O., Rise, L., et al. (2007). The role of geological setting and depositional history in offshore slope instability. In *Offshore Technology Conference*. Offshore Technology Conference.

Stein, S., Cloetingh, S., Sleep, N. H., and Wortel, R. (1989). Passive margin earthquakes, stresses and rheology. In *Earthquakes at North-Atlantic Passive Margins: Neotectonics and Postglacial Rebound*, pages 231–259. Springer.

Stephansson, O. (1988). Ridge push and glacial rebound as rock stress generators in Fennoscandia. *Bulletin of the Geological Institutions of the University of Uppsala*, 14:39–48.

Strout, J. M. and Tjelta, T. I. (2005). In situ pore pressures: What is their significance and how can they be reliably measured? *Marine and Petroleum Geology*, 22(1):275–285.

Talling, P., Clare, M., Urlaub, M., Pope, E., Hunt, J., and Watt, S. (2014). Large submarine landslides on continental slopes: Geohazards, methane release, and climate change. *Oceanography*, 27(2):32–45.

ten Brink, U. S., Lee, H. J., Geist, E. L., and Twichell, D. (2009). Assessment of tsunami hazard to the US East Coast using relationships between submarine landslides and earthquakes. *Marine geology*, 264(1):65–73.

Terzaghi, K. (1950). Mechanism of Landslides: In Engineering Geology (Berkey) Volume. *Geological Society of America, New York.*

Travasarou, T. and Bray, J. (2003). Optimal ground motion intensity measures for assessment of seismic slope displacements. In *2003 Pacific Conference on Earthquake Engineering, Christchurch, New Zealand, Feb.*

Tveit, R. K. (2013). Implications of a m=6.0 earthquake along the øygarden fault zone for the city Bergen: Ground motion simulations and estimation of local site effects. *Department of Earth Science. UiB. Master thesis.*

Wells, D. L. and Coppersmith, K. J. (1994). New empirical relationships among magnitude, rupture length, rupture width, rupture area, and surface displacement. *Bulletin of the Seismological Society of America*, 84(4):974–1002.

Wieczorek, G. F., Wilson, R. C., and Harp, E. L. (1985). Map showing slope stability during earthquakes in San Mateo County, California. Technical report.

Yu, H.-T., Yuan, Y., and Bobet, A. (2013). Multiscale method for long tunnels subjected to seismic loading. *International Journal for Numerical and Analytical Methods in Geomechanics*, 37(4):374–398.